THE FLORIDA STATE UNIVERSITY

COLLEGE OF ARTS AND SCIENCES

PRECOMPUTED GLOBAL ILLUMINATION OF ISOSURFACES

By

KEVIN M. BEASON

A thesis submitted to the
Department of Computer Science
in partial fulfillment of the
requirements for the degree of
Master of Science

Degree Awarded:
Summer Semester, 2005

The members of the Committee approve the thesis of Kevin M. Beason defended on July 26th, 2005.

David C. Banks
Professor Directing thesis

Mark Sussman
Outside Committee Member

Xiuwen Liu
Committee Member

To Mom and Dad. . .

ACKNOWLEDGEMENTS

Thank you very much to my advisor, David Banks, who on countless occasions went above and beyond the call of duty to assist me in a great number of ways, including everything from teaching, advising, pushing for my readmittance, years of funding and conference sending, to publishing, all in the effort to provide me with a quality education. Thank you to my committee, Mark Sussman and Xiuwen Liu, and to the many other people at FSU who assisted me along the way, including everyone at the Vis Lab, including Josh Grant, Brad Futch, Hui Song, Wilfredo Blanco, Chris Baker, Yoshihito Yagi, Chuck Mason, Neil Druckmann, Michael Connor, Theresa Chen, and Kevin Kurtz. A special thanks to Mickey Boyd for his encouragement, support, and advice. Thank you to Kayne Smith and Chris Baker for their excellent proof reading. I would also like to thank David Gaitros, Joseph Travis, Dana Lutton, the SCS administrative staff, and the SCS systems staff. Thank you to the scientists who provided datasets and feedback: M. Y. Hussaini, Kayne Smith, Jorge Piekarewicz, Debra Fadool, and Wilfredo Blanco. Also, thanks to Mike Cammarano, Steven Parker, and Henrik Jensen for heir helpful correspondences. Thank you to FSU's Master Craftsman Program for the bump box sculpture and light guide. Thank you to all my friends for their support and understanding, including Matt Scragg, Mike Scragg, Melissa Kryder, Silvana Perolini, and many other people that helped me along the way. Most importantly, thank you to my Mom and Dad, for their infinite support and love, without which none of this would have been possible. Also thank you to my loving sister, Laura, whom I wish the best of luck in her upcoming schooling.

This research was supported by the SCS Visualization Laboratory and by NSF Grant #0083898.

TABLE OF CONTENTS

LIST OF TABLES

LIST OF FIGURES

ABSTRACT

Three dimensional scalar heightfields, also known as volumetric datasets, abound in science and medicine. Viewing the isosurfaces, or level sets, is one of the two main ways to display these datasets, the other being volume visualization. Typically the isosurfaces are rendered on a personal computer (PC) allowing the scientist or doctor analyzing the dataset to interactively change the isovalue, and rotate or zoom the isosurface. Unfortunately, out of necessity due to the PC's video card, current techniques render the isosurfaces with a basic hardware-accelerated lighting model. This lighting model lacks important features such as shadows, and as a result the isosurfaces are more difficult to interpret than if they had been rendered with a physically based lighting model.

My thesis is that isosurfaces can be displayed with realistic illumination at interactive rates on a typical PC. I present a method for applying global illumination to interactively created isosurfaces, using a physically based lighting model, with a negligible increase in the time required to render the isosurfaces. The result is convincing shading that is easy to interpret by the human visual system, including features such as soft shadows, inter-reflection, caustics, and color bleeding. This is achieved by solving the rendering equation for all isosurfaces within the volume, storing the solutions in a 3D texture, and then texture mapping the result onto a polygonal approximation of the isosurface. This process is called "heightfield rendering".

CHAPTER 1

INTRODUCTION

1.1 Problem description

“Scientific visualization” is a practice whose origins trace to the massive datasets generated from computational simulations (chiefly using supercomputers at national research laboratories) of physical phenomena. The archetypical dataset is a scalar function $h : \mathbb{R}^3 \rightarrow \mathbb{R}$ representing, for example, density, pressure, or temperature. As Hamming noted, “[the] purpose of computation is insight, not numbers” [11]. The premiere technique for displaying such a dataset is to generate its level sets (isosurfaces) $\mathscr{L}_{const} = \{\vec{p} : h(\vec{p}) = const\}$. These surfaces convey qualitative aspects of the function to the scientific user analyzing the data. Examples are presented in Figure 1.1.

In the field of computer graphics, considerable success has been achieved in creating photo-realistic renderings of surfaces by solving the integral equation for light transport. Such realistic images offer important shape-from-shading cues to the human visual system. Current research in rendering concerns producing these high quality images at interactive rates (1 Hz or faster).

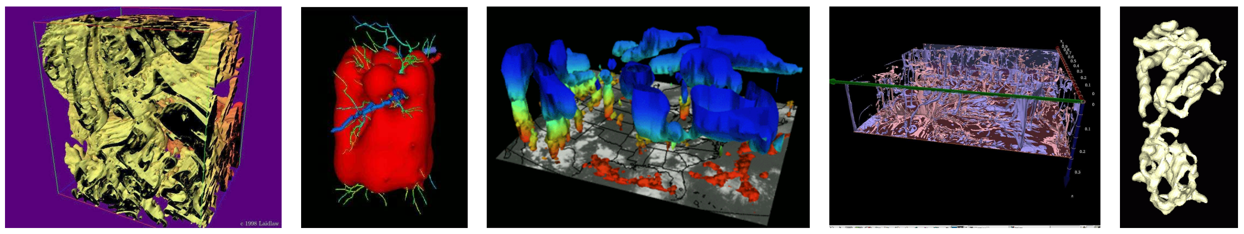

Figure 1.1: Example isosurfaces. (a) Temporal evolution of turbulent jet concentration isosurface [1] (b) iso-temperature surface calculated in a tissue volume with a number of thermal significant blood vessels [2] (c) temperature isosurface built from satellite data [3] (d) thermal plumes [4] (e) isosurface of density map for Bluetongue virus capsid protein [5]

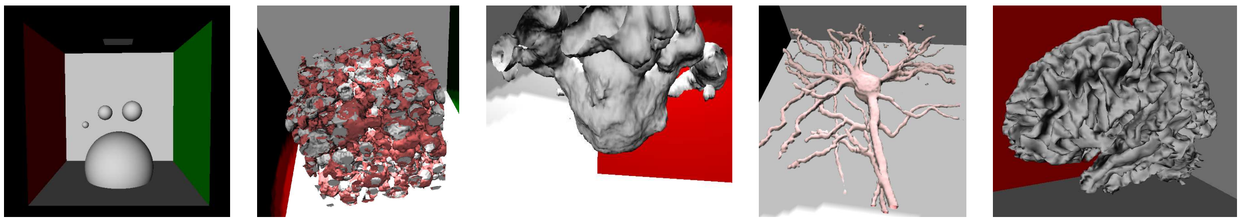

(a) bump box (b) Nucleons (c) LAPR (d) Neuron (e) Brain

Figure 1.2: Example datasets, shown as isosurfaces from functions of the form $h : \mathbb{R}^3 \to \mathbb{R}$. (a) A superposition of five Gaussian-like density functions (b) An MRI scan of a human brain from McGill University (c) Water density in a simulation of Laser Assisted Particle Removal (LAPR) (d) Confocal microscope scan of a living mouse neuron (e) Nucleonic densities from a simulation of the crust of a neutron star

However, there has been no effort to date in the visualization community either to solve the equation for light transport on isosurfaces or to make the process fast enough for the scientist to view the illuminated isosurfaces on an ordinary desktop computer. **My thesis is that both goals can be achieved. That is, globally illuminated isosurfaces of a scalar function $h : \mathbb{R}^3 \to \mathbb{R}$ can be generated and displayed at interactive rates on an ordinary desktop computer equipped with a graphics card.** I demonstrate this thesis by (1) solving a modified version of the light transport equation on the graph of h, (2) storing the solution in a three dimensional (3D) texture, and then (3) texture mapping the result onto a polygonal approximation of the isosurface. I call this 3-step pipeline "heightfield rendering".

I demonstrate heightfield rendering on actual datasets produced by scientists at Florida State University (FSU) and McGill University [12], plus one (analytically defined) reference dataset that I call the "bump box." Figure 1.2(a) shows the bump box dataset consisting of the superposition of five 3D Gaussian-like functions with varying parameters. The second dataset, whose isosurface is shown in Figure 1.2(b), is a density convolution of the exotic nuclear structures in the crust of a neutron star. This dataset is from Dr. Jorge Piekarewicz in the Department of Physics at FSU and Brad Futch in the School of Computational Science (SCS) at FSU. Next, Figure 1.2(c) shows density data from a molecular dynamics simulation of Laser Assisted Particle Removal (LAPR), conducted by Dr. M.Y. Hussaini and Dr. Kayne Smith in SCS at FSU. Figure 1.2(d) shows the fourth dataset, from a confocal microscope scan of a living mouse neuron. This dataset is from Debra Fadool in the Department of Neuroscience at FSU, and Wilfredo Blanco in SCS at FSU.

Lastly, Figure 1.2(e) is a Magnetic Resonance Imaging (MRI) scan of a human brain, scanned at the McConnell Brain Imaging Center at McGill University.

1.2 Novelty

The novel contributions contained herein are as follows:

1. The thesis (from Page 2) is proved by example. (Page 86)
2. I introduce the "bump box" as an analytically defined reference function. (Page 22)
3. I expand on the idea of storing global illumination in a texture (similar to vicinity shading [13]). (Page 67)
4. I introduce the idea of foliating the domain $\mathscr{D}$ of a heightfield $h : \mathbb{R}^n \to \mathbb{R}$ into level sets and illuminating each level set of $\mathscr{D}$. (Page 42)
5. I introduce the idea of foliating the graph of a heightfield and illuminating each raised level set in $\mathscr{D} \times \mathscr{R}$, where $\mathscr{R}$ is the range of the heightfield function. (Page 41)
6. I introduce the idea of flattened illumination of a heightfield function within $\mathscr{D} \times \mathscr{R}$. (Page 28)
7. I provide a definition of, equations for, and an implementation of flattened emittance. (Page 32)
8. I define, provide equations for, and implement flattened reflectance. (Page 36)
9. I provide a brightness correction term for flattened 3D rendering. (Page 46)
10. I devise a 3D photon-map-based flattened radiance estimate. (Page 38)
11. I decouple sampling the radiance of a heightfield surface from level set generation. (Page 43)
12. I compare the error of different graph sampling techniques. (Page 71)
13. I demonstrate heightfield rendering on actual datasets from medicine, astrophysics, neuroscience, and nanochemistry. (Page 76)

14. I demonstrate incorporating heightfield rendering into a commercial visualization software (amira from Template Graphics Systems). (Page 85)

15. I provide a corrected version of the algorithm by Parker *et al.* [9] to find a ray-isosurface intersection for trilinear boxes. (Page 88)

1.3 Solving Light Transport

1.3.1 Introduction to global illumination

In the real world, light reflects off surfaces onto other surfaces. If the material is transparent, such as glass, light may transmit through the surface. The transmission and reflection of light is called *light transport*. Regions that receive less light because objects are obstructing the light source are in *shadow*. If light has bounced off at least one surface before arriving at a region, the light is called *indirect* light, or indirect illumination. This bouncing of light from one surface to another is *inter-reflection*.

Photo-realistic means a picture looks similar to, or is indistinguishable from, an actual photograph. Making photo-realistic images is called realistic image synthesis. Typically a scene description is created, containing a 3-dimensional model along with the position of lights and a camera, and given as input to a program which generates an image. The quality of the generated image, in particular the degree of photo-realism achieved, depends on the shading algorithm the program implements [14].

Early shading algorithms such as Phong's [15] and Blinn's [16] simulate local shading effects. Local shading effects occur if the scene is composed of only the region in question and the light source. These algorithms do not consider how the scene as a whole may reflect or occlude the light, because it was considered too computationally expensive to account for these large-scale complex interactions. As a result, this simple type of illumination is known as *local illumination*. OpenGL is probably the most prominent example of local illumination. OpenGL is a standard interactive graphics library and employs a local illumination model by default.

For example, Figure 1.3(a) shows a simple scene rendered using OpenGL's local illumination shading. The scene appears fake because a simple local illumination computation is performed at the corners of the scene and the colors are linearly interpolated across the surfaces. Even if the shading is performed per-pixel, important features such as shadows will be absent because only

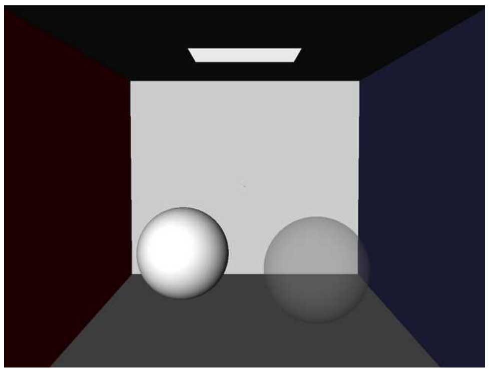
(a) “Local” illumination

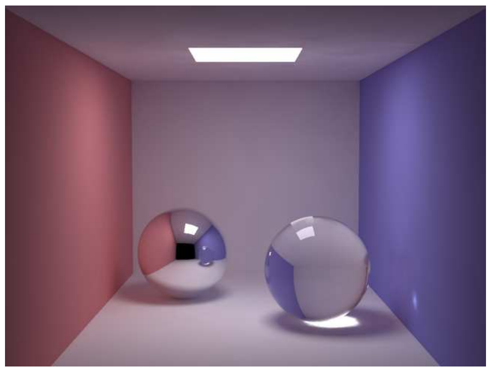
(b) Global illumination

Figure 1.3: Results of applying two different illumination models to a simple scene. The image on the left was rendered using an OpenGL / hardware lighting model. The image on the right was rendered using the author’s global illumination ray tracer, *Pane*.

the local geometry is considered and any other geometry that may potentially be blocking the light is ignored.

Today there are a class of algorithms that accurately simulate light transport and produce realistic-looking images. These algorithms take into consideration the geometry of the entire scene and simulate *all* possible paths light can travel in order to illuminate a surface. They are based on a subset of physics describing energy transfer, known as radiometry. Simulating all paths light can travel between a light source and a camera is called *global illumination* [6].

Global illumination allows for natural phenomena such as penumbras (soft shadows), caustics (the focusing of light through a lens), and indirect lighting (highly reflective surfaces acting as light sources), including color bleeding. Figure 1.3(b) shows the scene in Figure 1.3(b) rendered using global illumination.

1.3.2 The importance of global illumination

A psychologist at the University of Minnesota conducted an experiment with human subjects to see if shadows and inter-reflection have an important effect on discerning surface contact [17]. Subjects were shown computer-generated images of a cube either slightly above or in contact with a flat surface. In order to gauge the importance of shadow and inter-reflection in distinguishing these two cases, several images of each case were generated. Some had shadows enabled, some had inter-reflection enabled, some had both enabled, and some had both disabled. For each configuration,

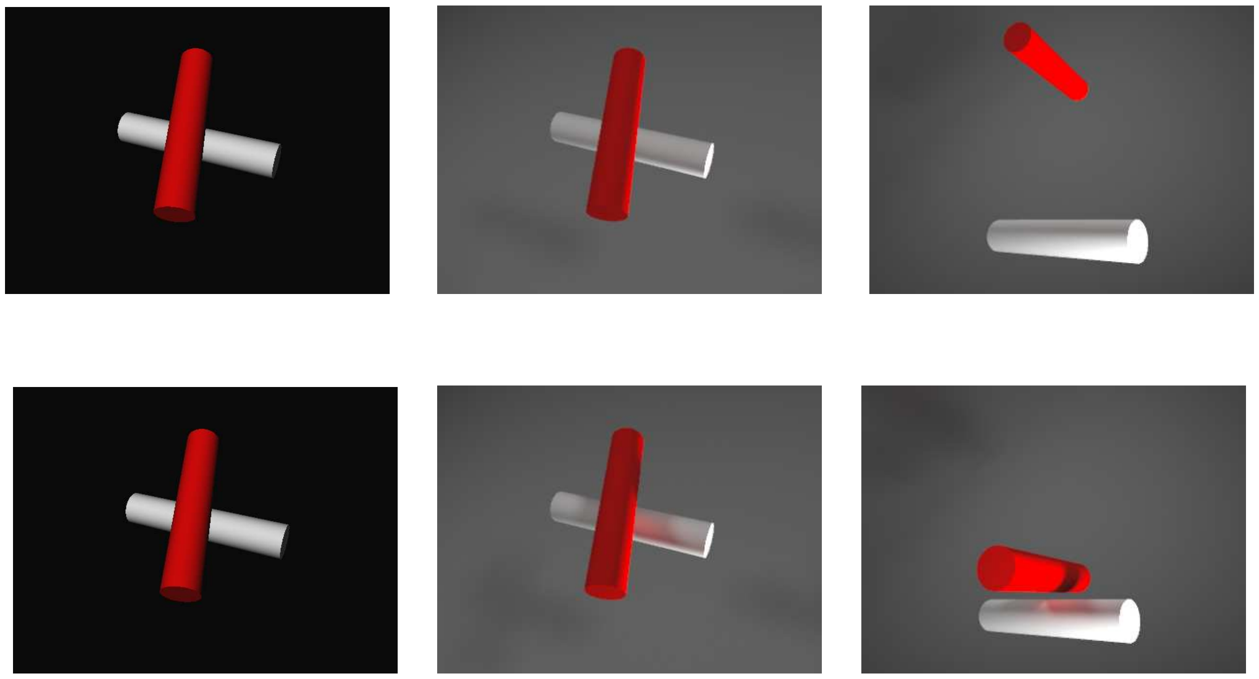

(a) Local illumination (b) Global Illumination (c) Side view

Figure 1.4: Example benefit of global illumination. In the top row the two cylinders are far apart. In the bottom row they are close. Viewed from above (a) it is difficult to discern the difference using local illumination (OpenGL). With global illumination (b) the shadow and inter-reflection present in the bottom scene provide natural distinguishing cues. A side view (c) further illustrates the difference between the two scenes.

the subjects were asked to decide whether or not the cube was touching the surface. The conclusion was that shadows played a very important role in correctly determining surface contact, and indirect illumination played an equally important role. The study found, however, that the greatest sensitivity to surface contact was achieved when *both* shadows and indirect illumination were present.

Figure 1.4 illustrates the benefit of these lighting components. The top row shows a scene where two cylinders are very close. The bottom row shows a similar scene where they are far apart. Viewed from above and rendered with local illumination (OpenGL), these scenes are indistinguishable. However, when rendered using global illumination the shadows and inter-reflection caused by the proximity of the tubes in the top row makes the difference obvious.

1.3.3 Computing global illumination

Simulating light transport is a challenging task. However, techniques exist to compute it efficiently. In image synthesis, the main goal is to find the color of each pixel in an image. The color represents light energy hitting the eye, so the problem becomes determining what energy is coming from the direction of each pixel.

What are the units of light energy for each pixel? The answer to this involves radiant flux. *Radiant flux*, Φ, is the time rate of flow of energy, Q, contained in the photons making up the light, and is expressed in Joules/second or Watts:

$$\Phi = \frac{\mathrm{d}Q}{\mathrm{d}t} \,.$$

The color of a pixel is determined by the radiance. *Radiance* is expressed in units of radiant flux per unit projected area per unit solid angle, or Watts per meters squared per steradian in SI units[1], and is given by:

$$L(\vec{x},\vec{\omega}) = \frac{\mathrm{d}^2\Phi}{\mathrm{d}A\ \cos\theta\ \mathrm{d}\vec{\omega}} \,,$$

where $\mathrm{d}A$ is the differential area receiving light from direction $\mathrm{d}\vec{\omega}$, and θ is the angle between $\vec{\omega}$ and the surface area normal.

Radiant energy is composed of photons at different wavelengths, however this explanation will ignore any wavelength dependence. The task of global illumination algorithms is to determine the radiance for each pixel. This value comes from the rendering equation (Equation 1.1) explained in the next section.

The Rendering Equation

The formula for radiance from a surface was first published by Kajiya in 1986 [18]. Today this formula is well known and understood to be the standard model for light transport between surfaces, and is called the *Rendering Equation*:

$$L(\vec{x},\vec{\omega}) = L_e + \int_{\Omega} f_r(\vec{\omega},\vec{\omega}')\, L_i(\vec{x},\vec{\omega}')\, (\vec{N}\cdot\vec{\omega}')\, \mathrm{d}\vec{\omega}' \,. \tag{1.1}$$

[1] In practice, the radiance is usually scaled by the spectral response of the human visual system, thereby turning it into luminance, and then the luminance is stored as the color of the pixel. However, this post-process is not always necessary and is ignored in this thesis.

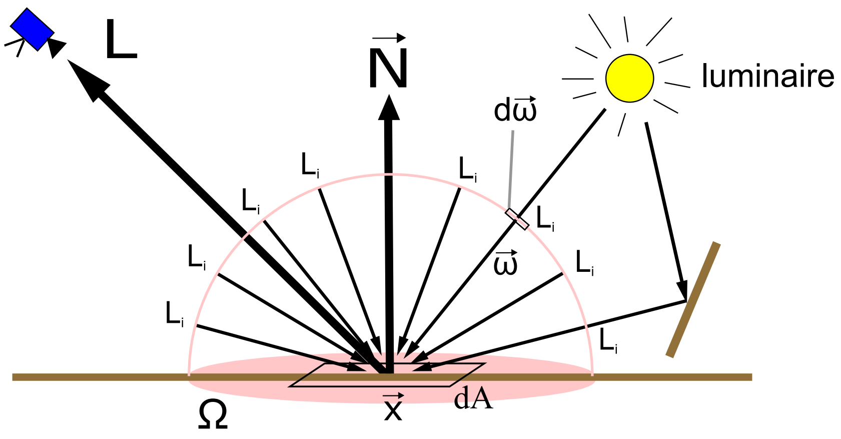

Figure 1.5: Diagram of components of the Rendering Equation (Equation 1.1). Incident radiant flux from the luminaire strikes a surface in the neighborhood dA of point $\vec{x}$. The incident radiance arrives from direction L_i and subtends a solid angle dω of the hemisphere Ω.

The rendering equation states that the radiance, $L(\vec{x},\vec{\omega})$, coming from a surface at point $\vec{x}$ in direction $\vec{\omega}$, is equal to the emitted radiance, L_e, plus the integral (sum) of the incident radiance, L_i, over a hemisphere, Ω, scaled by a Bidirectional Reflectance Distribution Function (BRDF) [19], f_r, and the dot product of $\vec{\omega}'$ and the surface normal $\vec{N}$. See Figure 1.5 for a diagram of these components.

The rendering equation is a Fredholm integral equation of the second kind because one of the unknowns appears outside the integral, making the equation recursive. That is, in order to calculate the outgoing radiance, the incoming radiance must be known, which uses the same formula. I show how to solve this equation, and thus global illumination and light transport, by using ray tracing.

Ray tracing

A *ray* is a parametric line specifying a position $\vec{r}$ given a parameter t, starting position $\vec{o}$, and direction vector $\vec{d}$ using the formula $\vec{r} = \vec{o} + t\vec{d}$ [20]. *Ray tracing* is the process of tracing a ray through a scene to find the first object it intersects, and the point of intersection. Ray tracing was introduced by Whitted in 1980 [21] in order to create an image of a scene. First a camera and an image plane are determined, then rays are traced from the camera through pixels in the image plane. Once the point of intersection between the ray and the scene is found, a color is computed and stored at the corresponding pixel. The program that performs this computation is called a *ray tracer*.

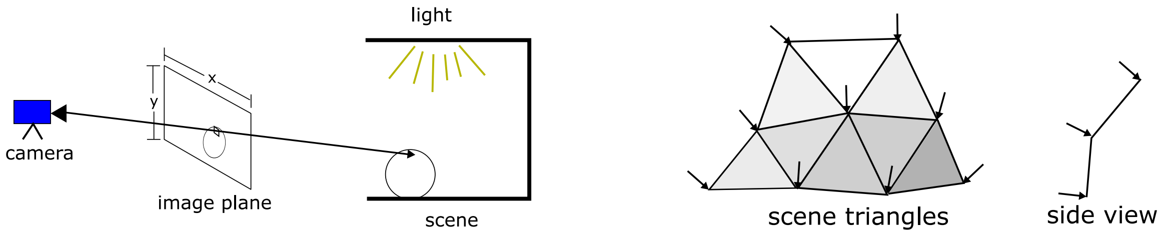

(a) Rendering an image: Color sample for each pixel

(b) Rendering a scene mesh: Color sample for each vertex

Figure 1.6: (a) In ray tracing an image, an imaginary image plane is positioned in front of the scene camera. For each pixel in the image plane, a ray is shot from the camera through the pixel. At the point of intersection of the ray with the scene, a color is computed and this color is stored in the image at the corresponding pixel. (b) For ray tracing a scene mesh, a ray is shot at each vertex, the color is computed, and then the color is stored at the vertex. These colors are then used the next time the scene is viewed.

It is simple to modify a ray tracer to store the computed colors at the vertices of the triangles that make up a scene mesh rather than at the pixels the rays go through. To do this, rays are fired at each vertex of each triangle in the scene from a small distance above the triangle and very close to the vertex. The computed color is then stored along with the vertex in the scene description. In Open Inventor, this is done using a per-vertex material binding. Figure 1.6 illustrates these two methods of ray tracing.

The speed of the ray-object intersection computation is critical in solving global illumination in a timely manner. A naive straight-forward approach of testing every n objects in a scene for intersection with a ray has time complexity $\mathrm{O}(n)$ (linear). This is prohibitively expensive for typical scenes, for which n may be several million or more. Instead, space subdivision techniques, including uniform grids [20], BSP trees [22], hierarchical bounding volumes [23], and octrees [24], are employed to test only those objects likely to be intersected. These intersection algorithms typically have time complexity $O(\log n)$, a significant improvement.

Photon mapping

Photon mapping is a global illumination algorithm, developed by Henrik Wann Jensen in 1996 [25] that uses ray tracing. It belongs to a class of global illumination algorithms that perform Bidirectional Path Tracing and, compared to other techniques, is extremely efficient.

For example, Monte Carlo path tracing (MCPT) [20], a straightforward technique to solve the

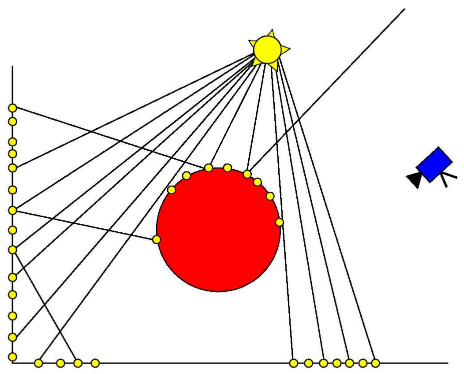

Figure 1.7: First pass of the photon mapping algorithm. Photons are fired from the light E into the scene using ray tracing. A photon is stored where a ray intersects the scene. Some intersections spawn a reflected ray, which may intersect the scene at a new point. (Redrawn from Figure 9.2 of of [6])

rendering equation, requires eight hours on a Dual 3.0 Gigahertz (GHz) PC to compute the image shown in Figure 1.3(b), and the result contains noise. Photon mapping, however, renders the image with virtually no noise in just six minutes on the same machine.

The idea of bidirectional path tracing algorithms such as photon mapping is that rays are not only fired from the camera (as in MCPT), but are also traced from the light sources into the scene. In photon mapping these interactions are stored as particles named *photons* in a data structure called the *photon map*.

Photon mapping is a two-pass algorithm. In the first pass photons are emitted from the light sources into the scene. The photons reflect, absorb, transmit, and scatter throughout the scene just as real photons would. See Figure 1.7. The number of photons used is user-controlled, but their sum carries the radiant power of the light source. For example, using n photons for a light source with power Φ, each photon p has power $\frac{\Phi}{n}$. That is,

$$\Phi_p = \frac{\Phi}{n}, \qquad p \in 1, \ldots, n . \tag{1.2}$$

The photon map approximates the light power distribution in the scene. Each photon represents a discrete amount of flux. The sum of the power of several photons on a small surface area patch gives an estimate of the total flux arriving at that surface patch. Dividing this total flux by the area

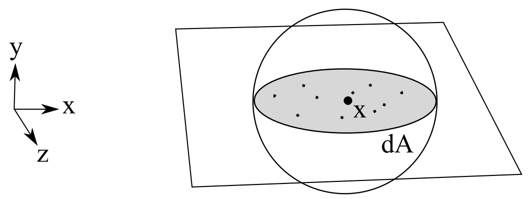

Figure 1.8: The reflected radiance estimate is $L_r = \sum f_r(\vec{\omega}, \vec{\omega}_p{}') \frac{\Phi_p}{\Delta A}$, where $f_r(\vec{\omega}, \vec{\omega}_p{}')$ is the BRDF, Φ_p is the power of photon p at distance d_p, and ΔA is the area of a circle with radius $\mathbf{max}(d_p)$ [6].

of the surface patch yields an estimate of the local flux density, or power per unit area:

$$E \approx \sum_{p=1}^{n} \frac{\Phi_p}{\Delta A} . \tag{1.3}$$

Multiplying each photon's power Φ_p by the BRDF $f_r(\vec{\omega}, \vec{\omega}_p{}')$ yields the following estimate of the reflected radiance:

$$L_r \approx \sum_{p=1}^{n} f_r(\vec{\omega}, \vec{\omega}_p{}') \frac{\Phi_p}{\Delta A}, \tag{1.4}$$

where ΔA is a small area containing n photons, $\Delta\Phi_p$ is the power of the pth photon, and f_r is the BRDF. See Figure 1.8 for a diagram. When added to the emitted radiance L_e, Equation 1.4 provides an estimate of the total radiance leaving a point on the surface patch, approximating the rendering equation, Equation 1.1.

Figure 1.9 shows the example scene in Figure 1.3 rendered using the photon map. The scene is blotchy, which is typical, but this is corrected during a second pass. The second pass splits the radiance computation into four parts and uses the power distribution approximation contained within the photon map to create a final image. This splitting is done as follows. Incident light, L_i, is split into three components: direct illumination, $L_{i,l}$, indirect illumination, $L_{i,d}$, and specular illumination, $L_{i,c}$ (*e.g.*, off mirrors or glass). The BRDF, f_r, is also split into two parts: a diffuse component, $f_{r,D}$, and a specular component, $f_{r,S}$. The rendering equation (Equation 1.1) then becomes:

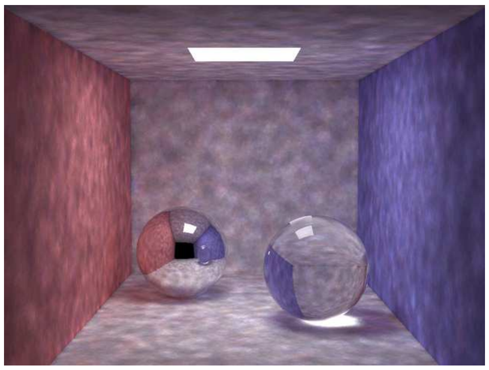

Figure 1.9: A simple box scene rendered using the photon map and the reflected radiance estimate (Equation 1.4). The image took 8 seconds to render on a Dual 3.0 GHz PC.

$$
\begin{aligned}
L(\vec{x},\vec{\omega}) =& L_e + \int_\Omega f_r(\vec{\omega},\vec{\omega}')\, L_i(\vec{x},\vec{\omega}')\, (\vec{N}\cdot\vec{\omega}')\, \mathrm{d}\vec{\omega}' \\
=& L_e + \int_\Omega (f_{r,S}(\vec{\omega},\vec{\omega}') + f_{r,D}(\vec{\omega},\vec{\omega}'))\, (L_{i,l}(\vec{x},\vec{\omega}') + L_{i,c}(\vec{x},\vec{\omega}') + L_{i,d}(\vec{x},\vec{\omega}'))\, (\vec{N}\cdot\vec{\omega}')\, \mathrm{d}\vec{\omega}' \\
=& L_e + \\
& \int_\Omega f_{r,D}(\vec{\omega},\vec{\omega}')\, L_{i,l}(\vec{x},\vec{\omega}')\, (\vec{N}\cdot\vec{\omega}')\, \mathrm{d}\vec{\omega}' + \qquad (1.5a) \\
& \int_\Omega f_{r,S}(\vec{\omega},\vec{\omega}')\, (L_{i,l} + L_{i,c} + L_{i,d})(\vec{x},\vec{\omega}')\, (\vec{N}\cdot\vec{\omega}')\, \mathrm{d}\vec{\omega}' + \qquad (1.5b) \\
& \int_\Omega f_{r,D}(\vec{\omega},\vec{\omega}')\, L_{i,c}(\vec{x},\vec{\omega}')\, (\vec{N}\cdot\vec{\omega}')\, \mathrm{d}\vec{\omega}' + \qquad (1.5c) \\
& \int_\Omega f_{r,D}(\vec{\omega},\vec{\omega}')\, L_{i,d}(\vec{x},\vec{\omega}')\, (\vec{N}\cdot\vec{\omega}')\, \mathrm{d}\vec{\omega}'. \qquad (1.5d)
\end{aligned}
$$

Briefly, the four integral components in Equation 1.5 are computed as follows. Equation 1.5a, the direct lighting estimate, is computed by using Monte Carlo integration and “shadow rays” to test visibility of the light source [26]. In this case, the shadow rays are shot directly at the lights rather than randomly (as in MCPT) and there is no recursion.

Equation 1.5b accounts for specular lighting, and is computed by sending a ray in the specular direction, and where the ray intersects, recursively solving Equation 1.5. While the calculation is recursive, for mirror-like surfaces only one recursive ray at each level of recursion is needed. This is a great simplification over having two (or more) recursive rays, because such recursion would result in an exponential growth in the number of rays for which Equation 1.5 must be solved.

Equation 1.5c computes caustics. The pattern of light on the table in Figure 1.10 is an example

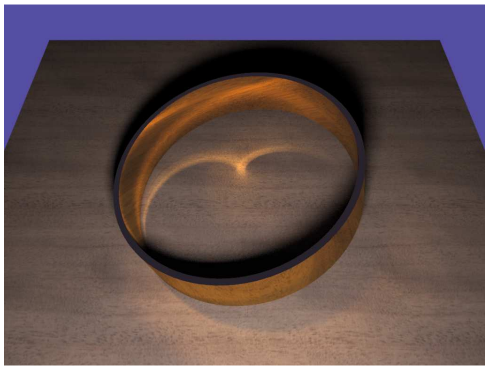

Figure 1.10: The pattern of light on the table is a caustic created by a metal ring. This is computed using a special photon map. The image took 7 minutes to render on a dual 3.0 GHz PC using the author's implementation of photon mapping.

of a caustic, and is caused by the metal ring focusing light from the source. Caustics are computed using a separate caustic photon map, reserved exclusively for specularly reflected photons. The radiance estimate in Equation 1.4 is then used directly, using the caustic photon map. Note that this computation is not recursive.

Equation 1.5d is computed in yet a different fashion. It captures inter-reflections between diffuse surfaces. That is, it accounts for incoming light that has been diffusely reflected at least once. This step is known as the "final gather" because it "gathers" the incoming indirect radiance from every direction in the hemisphere. Typically this final gather is the most costly component of Equation 1.5. Figure 1.11 shows a diagram illustrating the parts of this computation. The hemisphere is sampled using rays and Monte Carlo integration, and where the rays intersect the scene the photon map is consulted to get an estimate of the reflected radiance using Equation 1.4. This averaging of the incoming indirect radiance is not recursive because the photon map is used at the first bounce, however it remains expensive because many (several hundred, or more) rays must be traced to compute a noise-free estimate of the indirect illumination.

The sum of these four components is a solution to the inherently recursive Rendering Equation, *i.e.*, a solution for light transport, where the solution has only a single level of recursion (shadow and final gather rays) in most cases. The exceptions are for mirrors and glass, and other specular surfaces, where some simple recursion is required. A reader interested in more details of the photon mapping algorithm should refer to Jensen's comprehensive book [6].

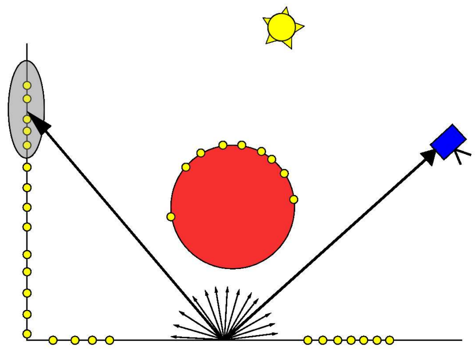

Figure 1.11: Inter-reflection is computed in the second pass of the photon mapping algorithm. This component of Equation 1.5 accounts for the reflection of incoming light that has already been diffusely reflected at least once. Monte Carlo path tracing is used to send rays in random directions and "gather" the incoming indirect radiance. This radiance is computed at the intersection of the ray with the scene using the photon map radiance estimate (Equation 1.4). By using a fast density estimation to compute the radiance instead of recursing, the scene is rendered much faster. Still, this component, the "final gather," remains the most costly to compute. (Redrawn from Figure 9.7 of [6])

1.4 Level Sets

Often a scientist has a dataset that defines a real value at points in a 3D subset of space, or volume, forming an explicit function $h : \mathbb{R}^3 \to \mathbb{R}$. Alternatively, the function may be parametric with parameters in $\mathbb{R}^3$. Datasets of this type may be referred to as volume datasets, 3D scalar fields, or 3D scalar heightfields.

Such a dataset may be from a boat wake simulation[2] where each point in space represents the signed distance to the water's surface, as shown in Figure 1.12(a); it may be an MRI scan, recording the water (H_2O) density throughout a patient's brain[3], as shown in Figure 1.12(b); or it may be a 3-dimensional joint density function, whose minimum represents the solution to a three-parameter optimization problem[4], as shown in Figure 1.12(c).

A 3D subspace is a continuous set of points. For a complex, non-parametric function, it is impossible to store the function's value at all points on the subspace with infinite precision, due

[2] The boat wake dataset is courtesy of Mark Sussman of Florida State University Department of Mathematics.
[3] The brain dataset is the same MRI scan from McGill University introduced previously.
[4] The maximum likelihood estimation dataset is from a class assignment by Anuj Srivastava at Florida State University Department of Statistics.

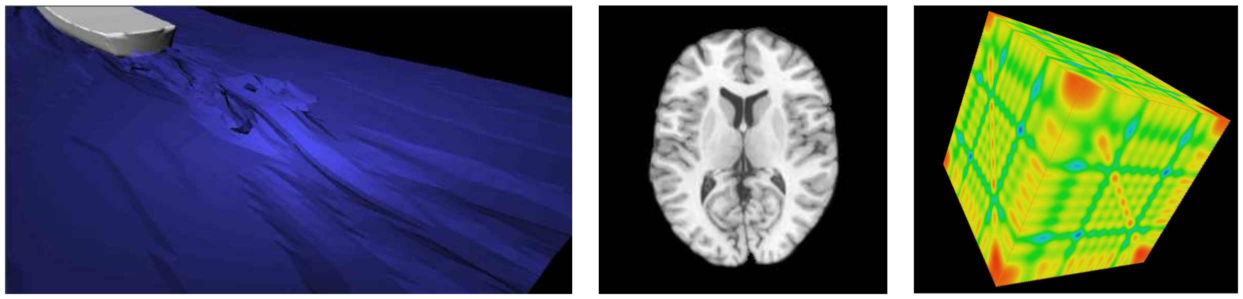

(a) (b) (c)

Figure 1.12: Example scientific datasets. (a) Ship wake from a computational fluid dynamics simulation (b) Slice of a MRI scan of a human brain (c) Maximum Likelihood Estimation for angles of three incoming signals.

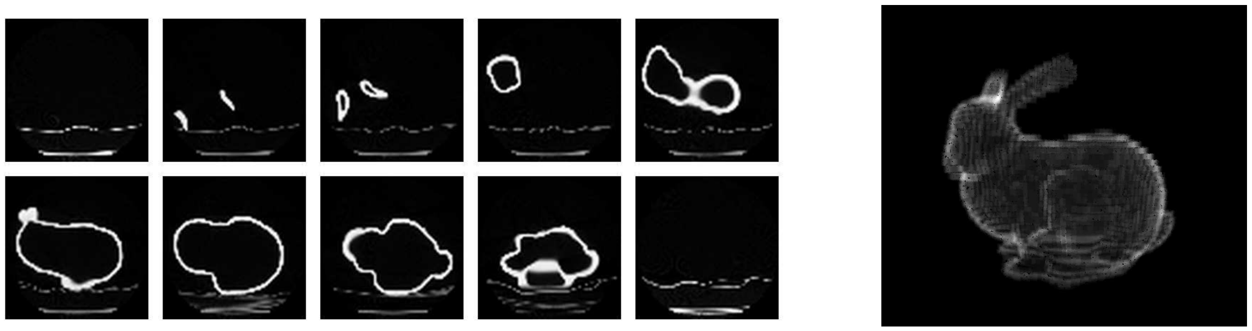

Figure 1.13: Example volume dataset. Left: slices from the volume. Right: volume rendering of the dataset created by my volume renderer.

to memory limits. In these cases the subspace is approximated using a regular grid of points, or 3D array. In this thesis I assume all datasets (functions) are defined on such a regular grid. If the dataset is defined at non-regular points, it can be converted to a regular grid using scattered data interpolation, discussed in Section 3.4.2.

Figure 1.13 illustrates an example volume dataset. The data is from a computed tomography (CT) scan of a clay bunny statue provided by Stanford University [27]. In CT, several x-rays scans of a volume from various angles are composited to form a 3D density image of the volume [28]. For the bunny dataset, the density of the bunny statue was stored at regular points in a rectangular volume at a resolution of $256 \times 256 \times 113$. On the left of Figure 1.13 are 10 slices from the dataset, following by a volume ("cloud") rendering of the dataset.

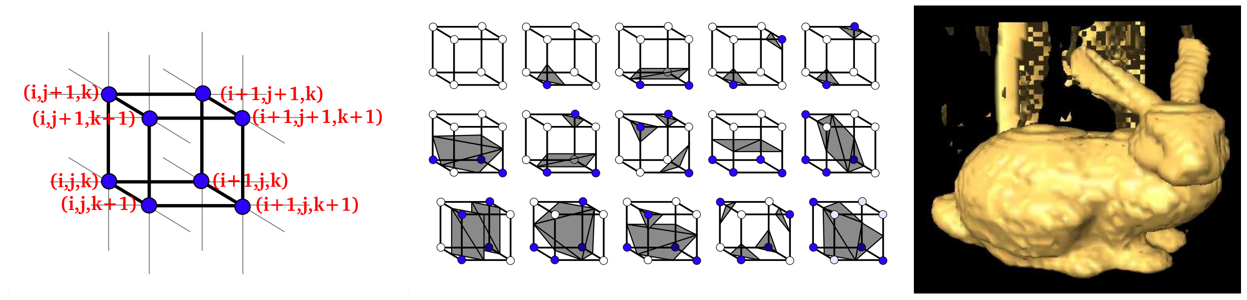

(a) (b) (c)

Figure 1.14: (a) A single grid cell (b) All possible triangulation cases in “Marching Cubes” (MC) (c) isosurface of the bunny dataset, visualized by amira.

1.4.1 Isosurface visualization

For a volume dataset $h(\vec{p})$ and a constant *const*, the set of points that satisfies $h(\vec{p}) = const$ implicitly defines a surface. The surface specified by *const* is called an *isosurface*, or level set, of h and the value *const* is called the *isovalue* of the isosurface. Figure 1.14(c) shows an example isosurface along with slices of the dataset the isosurface was derived from. The isosurface was created by a popular scientific visualization software package called “amira”.

Marching cubes

The most popular algorithm to create an isosurface is “Marching Cubes” (MC). The MC algorithm was published by Lorensen in 1987 [29]. It creates a polygonal mesh representing an isosurface in a 3D dataset. The user inputs the dataset and an isovalue and MC returns a mesh composed of triangles following the isosurface.

MC is fast enough to run at interactive rates on reasonably sized datasets (256^3 or less) using a regular PC. In “amira” and other software programs that use MC, the user slides a dragger to change the isovalue and the program sweeps through the different isosurfaces, using MC to extract them. Isosurface extraction on an Intel Pentium 4 3.0 GHz PC generally takes between 0.1 to 10 seconds per isosurface, depending on the resolution of the dataset and the number of triangles needed to approximate the isosurface, fast enough to be performed while the user waits.

Recall that a volume dataset is a 3D array of values arranged in a grid. These grid-point-value pairs are called voxels. This grid can be thought of as an array of volume cells, wherein a cell’s corners are grid points (voxels) in the dataset. Figure 1.14(a) shows an example cell having a corner

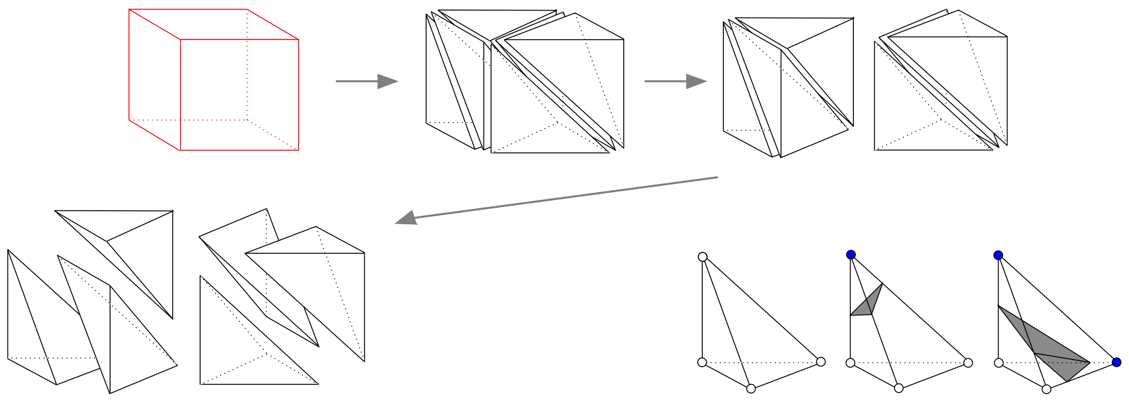

Figure 1.15: A cube is split into six tetrahedra. Each tetrahedron has only three cases for triangulation, which are shown.

at dataset coordinates (i, j, k). For any edge in a cell, if the value of h at one endpoint of the edge is higher than the isovalue and the value at the other endpoint is lower, then the isosurface passes through that edge. The same is true for the other edges; thus it is known where the isosurface intersects the cell edges. The edge crossings can be connected to form triangles, and the result is a surface within the cell that roughly approximates the isosurface within that cell. Repeating this process for each cell in the dataset (the “Marching” part of the algorithm) results in a triangular mesh that approximates the isosurface throughout the subspace spanned by the grid.

There is a finite combination of scenarios wherein a cell’s edge’s endpoints (the corners of the cell) have either a higher or lower value than the isovalue. Thus, there is a finite combination of edges that must be connected. In fact, by ignoring symmetry and rotation, there are only 15 different cases. These cases are illustrated in Figure 1.14(b).

Marching tetrahedra

In some of these MC cases there is ambiguity (two or more choices) over how to connect the edge crossings. If speed is not a priority this ambiguity can be removed by using another isosurface generation algorithm, “Marching Tetrahedra.”

Marching Tetrahedra works in almost the same way as MC except that the cells are further broken down into six[5] tetrahedra [30]. If symmetry and rotation are ignored, each tetrahedron has

[5] There are multiple ways to break a cube into tetrahedra. As few as five tetrahedra can be used, but doing so may present unwelcome asymmetry.

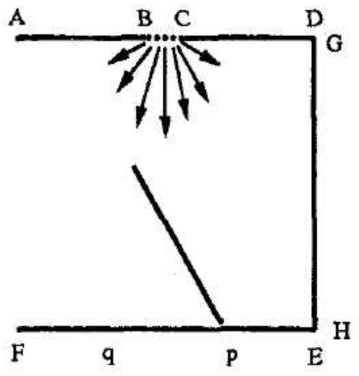

(a)

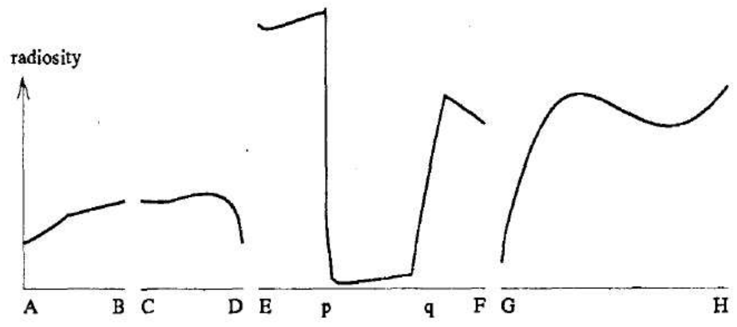

(b)

Figure 1.16: (a) Flatland test scene: all edges are reflective except light source *BC*, and angled edge, which is black. The angled obstacle causes a sharp penumbra at *p* and a gradual one at *q*. (b) Radiosity as a functino of arc length along the non-black edges of test scene. Note the sharp shadow edge at *p* and the gradual one at *q*. (Reproduced from [7])

only three possible cases for triangulation. Figure 1.15 shows the trivial case, the one-triangle case, and the two-triangles case.

The triangles through all six tetrahedra in the cell are created and the process is repeated for the remaining cells in the grid. The final result is a smoother surface than MC, with no ambiguity, but at the cost of more triangles and processing power.

1.5 Flattened light

The graph of a 3D heightfield $h : \mathbb{R}^3 \rightarrow \mathbb{R}$ is a volumetric 3-manifold in $\mathbb{R}^4$, just as the graph of a 2D heightfield $h : \mathbb{R}^2 \rightarrow \mathbb{R}$ is a surface in $\mathbb{R}^3$. It is sometimes useful to reason by analogy in a lower dimension in order to gain insight into the nature of objects in a higher dimension. Heckbert takes this approach and adapts the Rendering Equation (Equation 1.1) to two-dimensions in a world he calls “Flatland” [7]. In Flatland, light emits and reflects while remaining in a plane. He presents a rendering equation adapted for light transport in two dimensions and a technique for solving the modified rendering equation using radiosity. Although he does this as an investigation into the mechanics and underlying principles of normal 3D light transport, his equations are useful for my adaptations of light transport into other dimensions, as will be shown in Section 3.3.1.

1.6 Related work

Parker *et al.* published a technique in 1999 [9] with which they can display a ray traced volume dataset, rendered at interactive speed, with arbitrary lighting including real shadows. They achieved this by using bricking, an optimized storage pattern for the volume data that capitalizes on cache utilization, and a large supercomputer: a Silicon Graphics (SGI) Origin 2000 with 128 processors. They achieve interactive volume data ray tracing on the order of 15 frames per second. Unfortunately for most users today, this amount of processing power and memory bandwidth is out of reach.

Each of the Origin 2000's processors is 200MHz; 32 nodes combined is 6400MHz. One may compare this with a modern desktop machine with two 3.0GHz processors with a combined performance of 6000MHz, and ask if the desktop machine can perform volumetric ray tracing at similar speeds as the supercomputer. In this case the Origin 2000 has a significant advantage. Due to the bricking storage technique for the volume dataset, their algorithm exhibits extremely high coherence, with 99.44% L1 cache hits and 97.6% L2 cache hits, and only 2.1MB/sec/processor memory bandwidth. Each of the 32 200MHz R10000 CPU in the Origin has a 32 Kb L1 cache and a 4 MB L2 cache [31], while a single Intel Pentium 4 Xeon 3.0GHz processor has a 28 Kb L1 cache and 1 MB L2 cache [32]. Combining the caches of each of the 32 nodes of the Origin 2000, the SGI has 1 MB of L1 cache and 128 MB of L2 cache, while the Dual Xeon machine has only 56 Kb of L1 cache and 2 MB of L2 cache. The SGI supercomputer has a significant advantage over the desktop machine, and it is unlikely the desktop machine will be able to perform interactive ray tracing of volume datasets at similar speeds.

Stewart published a paper describing a technique called "vicinity shading" in 2003 [13]. He assumes a uniform diffuse lighting model (sphere or dome lighting) and calculates occlusions in a small region near each voxel. This method produces soft shadows, which is a partial global illumination solution. The shading is correct but is not a full solution since it does not account for color bleeding (indirect illumination), caustics, or non-uniform luminaires.

1.7 Organization

The remainder of this thesis is organized as follows. Chapter 2 discusses displaying scalar fields. Chapter 3 devises a new technique, called heightfield rendering, to interactively display isolines from a heightfield surface with global illumination. The purpose of this chapter is to explain heightfield rendering in two dimensions before explaining it for three dimensions in the next chapter. Chapter 4 uses heightfield rendering to interactively display isosurfaces from a heightfield volume, with full global illumination. Chapter 5 applies heightfield rendering to scientific datasets and presents the results along with timings.

CHAPTER 2

Using the Bump Box as a Reference Dataset

There are at least two ways to display a heightfield $h : \mathbb{R}^n \to \mathbb{R}$. The first way is a graph. Let the domain, $\mathbb{R}^n$, of h be called $\mathscr{D}$, and the range, $\mathbb{R}$, be called $\mathscr{R}$. The *graph* of h exists in $\mathbb{R}^{n+1}$ or $\mathscr{D} \times \mathscr{R}$ and is defined to be the set of points $\{(\vec{p},\, h(\vec{p})) \in \mathscr{D} \times \mathscr{R} : \vec{p} \in \mathscr{D}\}$. The graph of an example two-dimensional heightfield is shown in Figure 2.1.

Another way to display h is to view its level sets. A *level set* of $h : \mathbb{R}^n \to \mathbb{R}$ is the set of points $\mathscr{L}_c$ in $\mathscr{D}$ that have the same value c under function h. That is,

$$\mathscr{L}_c = \{\vec{p} \in \mathscr{D} : h(\vec{p}) = c\}.$$

A *foliation* of an n-manifold such as $\mathbb{R}^n$ is a partition of the manifold into disjoint and connected submanifolds called *leaves*. The graph and the level sets are related as follows. Let $\mathscr{D}_c$ be the subspace in $\mathscr{D} \times \mathscr{R}$ that projects to some isovalue c in the range. That is,

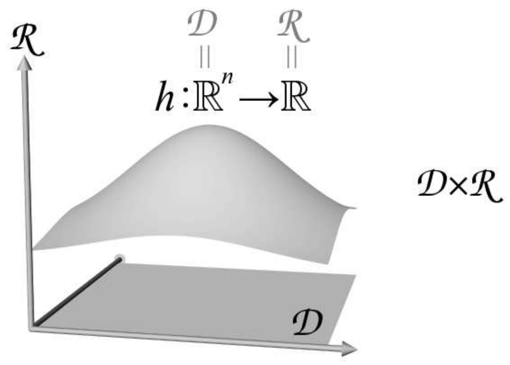
$\mathcal{R}$
$\mathcal{D}$ || $\mathcal{R}$ ||
$h : \mathbb{R}^n \to \mathbb{R}$
$\mathcal{D} \times \mathcal{R}$
$\mathcal{D}$

Figure 2.1: Graph of an example 2D heightfield $h : \mathbb{R}^n \to \mathbb{R}$, for $n = 2$. The graph exists as a surface in $\mathbb{R}^{n+1}$.

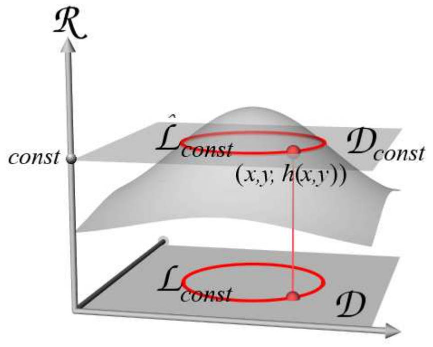

Figure 2.2: Graph and level set of an example 2D heightfield $h : \mathbb{R}^n \to \mathbb{R}$, with $n = 2$. The plane $\mathscr{D}_c$ projecting to c in the range $\mathscr{R}$ contains $\hat{\mathscr{L}}_c$ which projects to the level set $\mathscr{L}_c$ in the domain $\mathscr{D}$.

$$\mathscr{D}_c = \{\vec{p} \in \mathscr{D} \times \mathscr{R} : \pi_{\mathscr{R}}(p) = c\}.$$

This subspace has the same dimensions as the domain but exists at height c in $\mathscr{D} \times \mathscr{R}$, as illustrated Figure 2.2. Each $\mathscr{D}_c$ is a leaf of the Euclidian space $\mathbb{R}^{n+1}$ (or $\mathscr{D} \times \mathscr{R}$). Let the set of points in $\mathscr{D}_c$ that project down to the domain to form $\mathscr{L}_c$ be called $\hat{\mathscr{L}}_c$. $\hat{\mathscr{L}}_c$ is just a raised version of the level set $\mathscr{L}_c$ at height c. More precisely,

$$\hat{\mathscr{L}}_c = \{\vec{p} \in \mathscr{D}_c : h(\pi_{\mathscr{D}}(\vec{p})) = c\}.$$

The union of all raised level sets $\hat{\mathscr{L}}_c$ for every c forms the graph of h. In other words, each $\hat{\mathscr{L}}_c$ is a leaf of the graph of h. The graph of h is the set of all level sets, spread continuously through the range $\mathscr{R}$, such that each level set $\hat{\mathscr{L}}_c$ exists in it's own raised domain $\mathscr{D}_c$. Chapter 3 explains how a conventional 3D ray tracer is adapted to ray trace the level sets of a 2D heightfield by ray tracing the *raised* level sets $\hat{\mathscr{L}}_c$, in the form of the 3D graph of h, instead of ray tracing the 2D level sets directly.

2.1 Bump box

I created a 2D and a 3D heightfield function to serve as a standard example. This standard example is a novel contribution of this thesis. The two functions are almost identical, as they are both analytically defined as a superposition of five Gaussian-like functions. The difference between

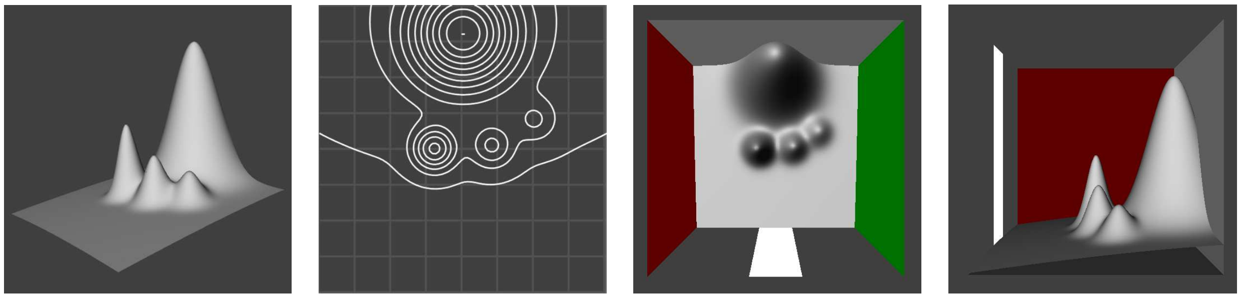
(a) Graph (b) Isolines (c) Overhead (d) Side

Figure 2.3: An example 2D heightfield $h : \mathbb{R}^2 \rightarrow \mathbb{R}$. (a) The graph of the heightfield (b) Several isolines from the heightfield (c) Overhead view of the graph placed in a box scene with a light, forming the “bump box”. (d) Side view of the “bump box”

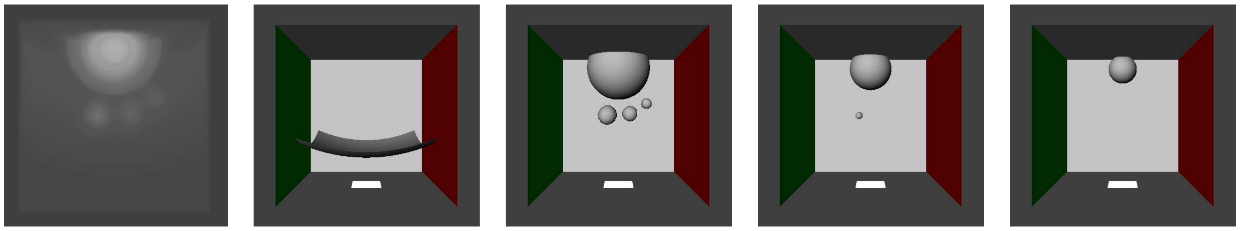
(a) Volumetric graph (b) L_{10} (c) L_{50} (d) L_{100} (e) L_{150}

Figure 2.4: (a) Volume rendering of an example 3D heightfield $h : \mathbb{R}^3 \rightarrow \mathbb{R}$ (b-e) Isosurfaces of the 3D heightfield in the 3D “bump box” test scene, for isovalues 10, 50, 100, and 150, respectively

them is that the 3D version is evaluated in three dimensions over a cubic domain, forming a 3D heightfield volume (Figure 2.4(a)), whereas for the 2D version z is set to zero and the function is evaluated over a square plane, forming a 2D heightfield surface (Figure 2.3(a)). I chose the functions because they exhibit multiple critical points and can easily be evaluated by anyone who wishes to reproduce this portion of my work.

In both the 2D and 3D versions, the evaluations of the function form a graph which is then placed in a special scene containing a light. The scene has four walls situated so that they surround the graph and provide indirect illumination from the light. The light is constructed so that it extends through the range of the graph, thereby illuminating each raised level set at its height c. For the 2D version this means the light extends along an entire side, while for the 3D version it is understood that both the walls and the light extend in the 4th dimension.

Table 2.1: Parameters for the 2D and 3D “bump box” scalar function in Equation 2.1.

a_1	=	0.0125	σ_1	=	0.036	$\mathbf{p}_1$	=	$(0.75, 0.60, 0.5)$
a_2	=	0.0200	σ_2	=	0.036	$\mathbf{p}_2$	=	$(0.60, 0.51, 0.5)$
a_3	=	0.0330	σ_3	=	0.036	$\mathbf{p}_3$	=	$(0.40, 0.50, 0.5)$
a_4	=	0.1670	σ_4	=	0.090	$\mathbf{p}_4$	=	$(0.50, 0.90, 0.5)$
a_5	=	1.6670	σ_5	=	1.350	$\mathbf{p}_5$	=	$(0.50, 1.50, 0.5)$

The 2D heightfield surface scene is called the “2D bump box” and is shown in Figure 2.3(c). The 2D bump box is used to study illumination of isolines of 2D heightfields in Chapter 3.

The 3D heightfield volume scene is called the “3D bump box,” and is shown in Figure 2.4(b). Chapter 3 uses the 3D bump box in order to explain how to create globally illuminated level sets of the example heightfield at interactive rates, thereby demonstrating my thesis.

Equation 2.1 is the explicit definition of the function used in these bump box scenes. In order to evaluate the 2D version z should be set to zero. The parameters used are given in Table 2.1. Equation 2.1 is slightly different than a true 1D Gaussian function due to an error in my function evaluation code.

$$F(\mathbf{x}) = \sum_{i=1}^{5} G_i(\mathbf{x}) \tag{2.1}$$

$$G_i(\mathbf{x}) = \frac{a_i}{\sigma_i\sqrt{2\pi}} \exp\left(\frac{-|\mathbf{x}-\mathbf{p}_i|^2}{(2\sigma_i)^2}\right)$$

CHAPTER 3

ILLUMINATING A HEIGHTFIELD SURFACE

This chapter explains how to display isolines from a 2D scalar heightfield $h : \mathbb{R}^2 \to \mathbb{R}$ with global illumination at interactive rates. The steps involved are: (1) solving a modified version of the light transport equation on the graph of h, (2) storing the solution in a 2D texture, and (3) applying the texture to a piecewise approximation of the isoline.

First, what is global illumination of an isoline? An isoline exists in two dimensions. Global illumination in two dimensions is explained in Heckbert's "Radiosity in Flatland" in the following way. The isoline, the scene containing the isoline, and the luminaire in the scene live in a flat 2D world, "equivalent to a three dimensional world where all objects have infinite extent along one direction" [7]. Light flowing in such a world could be obstructed by line segments, creating shadows on line segments in the background. Lines not directly facing the luminaire should be dimmer than those facing it, as they receive less light per unit length. Also light can reflect onto other segments to create indirect lighting. In this chapter global illumination is applied to isolines not to illuminate them so they appear in some sense "real," but to demonstrate the thesis in a lower dimension for ease of understanding.

In this spirit, one approach to illuminating the isoline is to extrude the isoline in the orthogonal direction, as shown in Figure 3.1, and then use a standard ray tracer to solve the light transport equation on the extruded isoline surface. In physics, *e.g.*, an electric field calculation, symmetry is exploited to reduce 3D problems into 2D ones since they are easier to solve. (This is possible due to the cancellation of non-orthogonal components of the electric field. While radiant power does not cancel out, per se, power leaving the plane is equal to power flowing into the plane, so the net flux is parallel to the plane.) Taking the reverse approach of physics, the 3D rendering solution of the extruded scene could serve as the 2D rendering solution of the isoline. A problem with this approach is creating a scene having infinite extent. While this may be achieved, or approximated

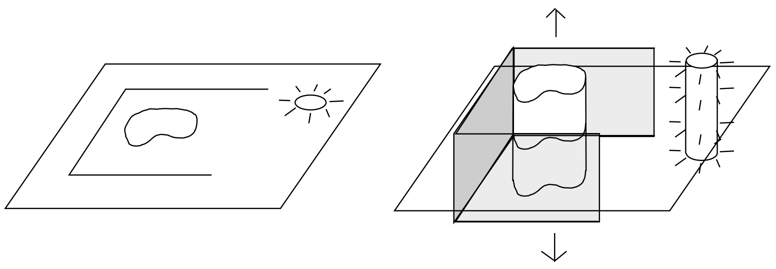

Figure 3.1: One approach to illuminating a 2D scene is to turn extrude it into a 3D scene. Left: An isoline with three "walls" and a light. Right: The same scene extruded along the orthogonal direction.

very closely, by extending a surface extremely far, other data structure problems would arise, such as creating and storing a photon map of infinite or very large size. Another flaw with this approach is that there are an infinite number of isolines to extract and construct a scene for ray tracing.

These problems are avoided by modifying the light transport equation to operate in just two dimensions and rendering the *graph* of h rather than individual isolines. The next two sections serve to motivate this approach.

3.1 Ordinary illumination

To understand why the light transport equation needs modification, it helps to first consider a result of unaltered light transport. Recall from Chapter 2 that the graph of h is the continuous set of level sets of h, where each level set $\mathscr{L}_c$ is raised to a height equal to its respective isovalue c. The graph of a two dimensional heightfield $h : \mathbb{R}^2 \to \mathbb{R}$ is a surface in $\mathbb{R}^3$, so it can therefore be illuminated using "ordinary" light transport as explained in Section 1.3. If the surface is rendered using global illumination, shadows and inter-reflections will be computed and it will have a photo-realistic appearance. Rendering can be done efficiently because solving light transport for a surface in three dimensions is a well-understood area of computer graphics and efficient techniques (such as photon mapping) already exist.

Figure 3.2 shows the graph of the 2D "bump box" as a surface illuminated with global illumination. Light emits and scatters in three dimensions to create an ordinary rendered surface, complete with shadows and inter-reflection. Figure 3.2(a) shows an emission of a photon from the luminaire in a random direction $\vec{\omega} \in \mathbb{S}^2$, and the subsequent 3D scattering distribution after the first bounce. Figure 3.2(b) shows the resulting rendered surface.

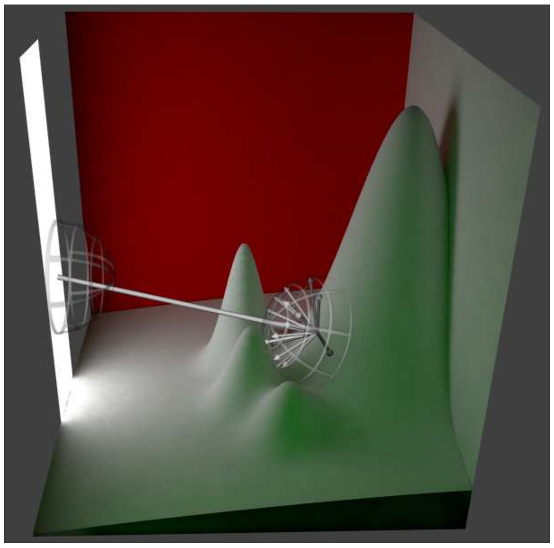
(a) Ordinary emission and reflection

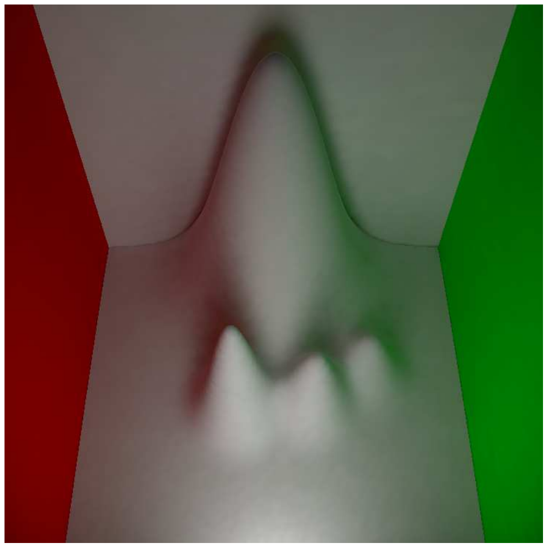
(b) Rendered surface

Figure 3.2: Graph of heightfield $h : \mathbb{R}^2 \to \mathbb{R}$ illuminated using ordinary 3-dimensional light transport. (a) Emission and reflection occur in three dimensions (b) Resultant illuminated graph.

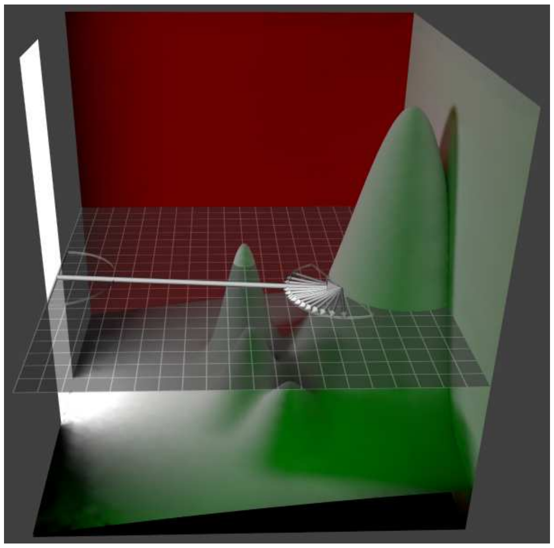
(a) Flattened emission and reflection

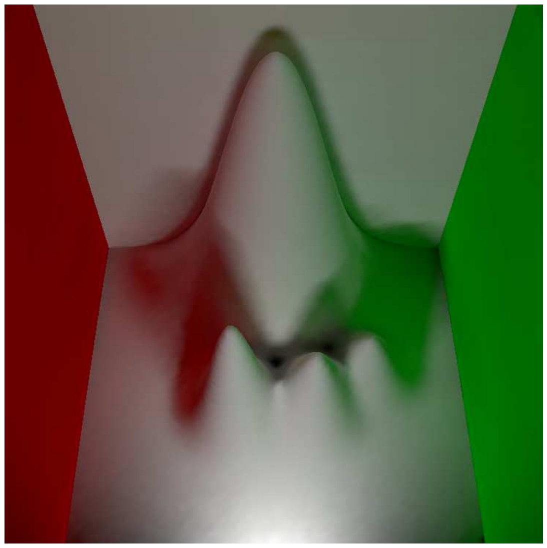
(b) Rendered surface

Figure 3.3: The surface can also be illuminated with “flattened” light transport. In flattened light transport, emission and reflection occur only within a 2D leaf. (a) Emission and reflection occur in two dimensions. (b) Resultant illuminated graph.

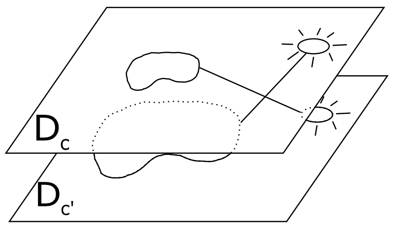

Figure 3.4: Light should not flow from one layer $\mathscr{D}_c$ to another layer $\mathscr{D}_{c'}$, for $c \neq c'$.

The graph is illuminated and, being a graph, contains all the level sets of h. While it may be possible to assign any level set $\mathscr{L}_c$ the color of its counterpart in the graph $\hat{\mathscr{L}}_c$, this method would produce incorrect lighting information for individual level sets. The reason is that light transport is occurring in three dimensions, and for each level set $\hat{\mathscr{L}}_c$ the lighting is dependent on the radiance of all the other level sets. Simply put, the inherent problem is that every level set $\hat{\mathscr{L}}_c$ receives illumination from every plane $\mathscr{D}_c \in \mathscr{D}$. That is, light can travel from one leaf $\mathscr{D}_c$ to another $\mathscr{D}_{c'}$ for $c \neq c'$, as shown in Figure 3.4.

The solution to this problem is to restrict light transport to two dimensions. That is, the solution is to "flatten" the transport so that light in layer $\mathscr{D}_c$ remains in $\mathscr{D}_c$ and only affects the level set $\hat{\mathscr{L}}_c$ contained within the layer, for every $c \in \mathscr{R}$.

3.2 Flattened light

If light was restricted to remain within its respective planes $\mathscr{D}_c$, $\forall\, c \in \mathscr{R}$, then the level set $\hat{\mathscr{L}}_c$ in each such plane would have a unique global illumination solution, independent of the other planes, offering all the benefits of global illumination such as shadows and inter-reflection. Previously introduced in Heckbert's Flatland [7], I call this light transport 3D "flattened" light transport. The "3D" part arises from the fact that light is flowing in a stack of 2D planes in three dimensions, while the "flattened" part refers to the light being restricted to a flat, 2D plane. This restricted light transport is a novel contribution of this thesis. The defining characteristics of flattened light transport within a 2D layer $\mathscr{D}_c$ are that:

- Luminaires emit only within the raised 2D layer $\mathscr{D}_c$.
- Reflection occurs only within the 2D leaf $\mathscr{D}_c$.

Figure 3.3(a) illustrates flattened light transport for a 2D heightfield surface. A photon emits in a plane $\mathscr{D}_c$ and intersects the graph of h. More specifically, the photon strikes the raised level set $\hat{\mathscr{L}}_c$. The photon then reflects using a distribution in 2D restricted to the plane of emission $\mathscr{D}_c$. Figure 3.3(b) shows the resulting graph rendered with 3D flattened light transport.

The surface rendered with flattened light transport appears different from the same surface rendered with ordinary light transport shown in Figure 3.2(b). The shadows behind the bumps are sharper because the luminaire is no longer able to shine at a downwards angle from above the bumps and partially fill in the shadowed regions, because there is no vertical transport of light. Additionally, the shadow regions on the walls are illuminated because of indirect illumination received from the red and green side walls, however there is a black region in the center where light is unable to penetrate laterally.

Unlike ordinary light transport, flattened light transport provides a lighting solution where the lighting in any single plane is independent of the other planes. The lighting in each slice of the graph of h is independent of the other slices, therefore the level set contained within each slice receives an independent lighting solution, offering all the features of global illumination, such as soft shadows, indirect lighting, and caustics. Furthermore, the graph represents the global illumination solutions for not just a few level sets, but *all* level sets of h. This is a useful result because global illumination solutions were found in a single rendering step without any explicit level set extraction.

Thus, the solution to rendering all level sets of a 2D surface heightfield function is to *flatten* light transport to two dimensions. By restricting light to leaves of the domain, each level set can receives an independent lighting calculation. This same idea will be applied in the next chapter to simultaneously render all level sets of a 3D volume heightfield.

The next section describes how to compute flattened light transport for a heightfield surface, and thus acquire illumination for all level sets of the corresponding 2D scalar field. Later sections address storing the transport solution and then displaying globally illuminated isolines using the stored solution. Chapter 4 adapts these techniques for heightfield volumes.

3.3 Flattened radiance for $h : \mathbb{R}^2 \to \mathbb{R}$

Let “flattened radiance” be the radiance of a point on a line segment within a 2D plane, and be denoted by $L^\flat$. Here the musical symbol for “flat,” $\flat$, is appended as a superscript to indicate that

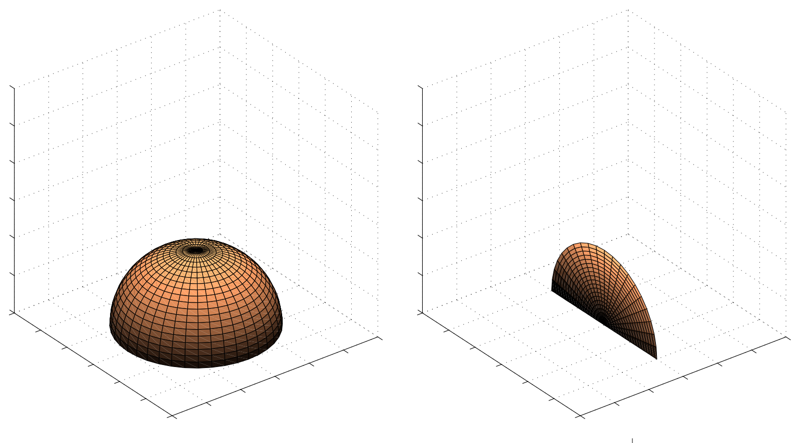

(a) E (b) $E^\flat$

Figure 3.5: (a) The emittance distribution $E : \mathbb{S}^2 \to \mathbb{R}^1$ for 3D light transport is a hemisphere. (b) The emittance distribution $E^\flat : \mathbb{S}^1 \to \mathbb{R}^1$ for 3D flattened light transport is a hemicircle.

the radiance is flattened.

The governing principles of flattened light transport are that emission and reflection of light, or energy, occur within the originating plane of the light. Whereas in ordinary 3D light transport the emission distribution is a modulated hemisphere, or half of $\mathbb{S}^2$, in 3D flattened light transport the emission distribution is a modulated hemicircle, or half of $\mathbb{S}^1$. See Figure 3.5 for a qualitative comparison of these two types of distributions:

$$\begin{array}{ll} \text{Ordinary light transport:} & E : \mathbb{S}^2 \to \mathbb{R}^1 \\ \text{Flattened light transport:} & E^\flat : \mathbb{S}^1 \to \mathbb{R}^1 \end{array} .$$

Similarly for reflection, in ordinary transport light reflects from one direction $\vec{\omega} \in \mathbb{S}^2$ in the hemisphere to another direction $\vec{\omega}' \in \mathbb{S}^2$, but in flattened transport light reflects from one direction $\vec{\theta} \in \mathbb{S}^1$ in the hemicircle to another direction $\vec{\theta}' \in \mathbb{S}^1$. The Bidirectional Reflectance Distribution Function fully captures this reflection and so its domain is altered:

$$\begin{array}{ll} \text{Ordinary light transport:} & f_r : \mathbb{S}^2 \times \mathbb{S}^2 \to \mathbb{R}^1 \\ \text{Flattened light transport:} & f_r^\flat : \mathbb{S}^1 \times \mathbb{S}^1 \to \mathbb{R}^1 \end{array} .$$

Furthermore the definition of radiance in Equation 1 changes from a quotient involving two dimensional area A and two dimensional direction $\vec{\omega}$ to a quotient involving one dimensional

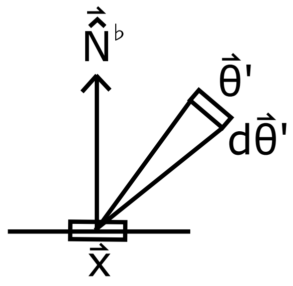

Figure 3.6: Flattened radiance is the radiant flux per unit angle per unit projected length, where $\mathrm{d}\vec{\theta}$ is the differential angle in direction $\vec{\theta}$, $\mathrm{d}\Lambda$ is the differential length, and $\vec{N}^\flat$ is the segment normal.

length Λ and one dimensional direction $\vec{\theta}$. Flattened radiance is then the radiant flux per unit *angle* per unit projected *length*:

$$L^\flat(\vec{x},\vec{\theta}) = \frac{\mathrm{d}^2\Phi}{\mathrm{d}\Lambda\, \cos\theta\, \mathrm{d}\vec{\theta}} \ ,$$

where $\mathrm{d}\Lambda\cos\theta$ is the projected differential length at position $\vec{x}$ receiving light from differential angle $\mathrm{d}\vec{\theta}$ in direction $\vec{\theta}$. The $\cos\theta$ scale factor can be computed as the dot product between $\vec{\theta}'$ and the normal $\vec{N}^\flat$ as shown in Figure 3.6.

Additionally, in 3D a surface of area A has an irradiance, $E = \frac{\mathrm{d}\Phi}{\mathrm{d}A}$, which specifies the radiant flux area density; in 2D a segment of length Λ has a 2D irradiance specifying the radiant flux *length* density, or incident radiant flux per unit length:

$$E = \frac{\mathrm{d}\Phi}{\mathrm{d}\Lambda} \ .$$

3.3.1 Flattened rendering equation

The rendering equation from Section 1 has also changed to reflect the loss of a dimension within a layer $\mathscr{D}_c$. The 3D flattened rendering equation is shown in Equation 3.2. It differs from the ordinary rendering equation in that the BRDF and incoming radiance are now one-dimensional rather than two-dimensional functions, and the integral is over the hemicircle rather than the hemisphere:

$$\text{Ordinary} \qquad L(\vec{x},\vec{\omega}) = L_e + \int_\Omega f_r(\vec{\omega},\vec{\omega}')\, L_i(\vec{x},\vec{\omega}')\, (\vec{N}\cdot\vec{\omega}')\, \mathrm{d}\vec{\omega}' \tag{3.1}$$

$$\text{Flattened} \qquad L^\flat(\vec{x},\vec{\theta}) = L_e^\flat + \int_\Theta f_r^\flat(\vec{\theta},\vec{\theta}')\, L_i^\flat(\vec{x},\vec{\theta}')\, (\vec{N}^\flat\cdot\vec{\theta}')\, \mathrm{d}\vec{\theta}' \ , \tag{3.2}$$

where, for the latter equation, $L^\flat(\vec{x}, \vec{\theta})$ is the flattened radiance leaving a point $\vec{x}$ in direction $\vec{\theta}$, $L_e^\flat$ is the flattened emittance, Θ is the set of π directions in the hemicircle above $\vec{x}$, $f_r^\flat(\vec{\theta}, \vec{\theta}')$ is the flattened BRDF, $L_i^\flat(\vec{x}, \vec{\theta}')$ is the flattened radiance incident to $\vec{x}$ from incoming direction $\vec{\theta}'$, and $\vec{N}^\flat$ is the segment's normal, as shown in Figure 3.6. This formulation of light transport within $\mathscr{D}_c$ is a novel contribution to the theory of rendering.

3.3.2 Solving the flattened rendering equation efficiently

Having a rendering equation to solve, it is now important to solve it *efficiently*. While it is not strictly necessary to have an efficient radiance calculation in order to perform heightfield rendering, it is definitely worthwhile in order to avoid the lengthy computational time and noise problems associated with the most general approach, Monte Carlo path tracing.

As discussed in Section 1, photon mapping is an efficient technique to solve the rendering equation. For this thesis I have adapted ordinary photon mapping to compute flattened light transport, thus solving the flattened rendering equation. For a surface heightfield, I call this modified algorithm “3D flattened photon mapping.” The following sections go into detail documenting the changes necessary in order to modify ordinary photon mapping into 3D flattened photon mapping and to compute flattened radiance. The main purpose of this discussion is to prepare the reader for the greater application of the technique to isosurfaces of a heightfield volume, addressed in Chapter 4.

3.3.3 Emissive radiance

For an ideal diffuse luminaire in three dimensions, the emitted radiance at any spot in any direction is a constant value. By integrating the radiance over the entire area and set of outgoing directions, a formula relating the total power output to the surface area and radiance is found [6]. Solving for the radiance produces the following formula:

$$\begin{aligned}
\Phi &= \int_A \int_\Omega L_e \cos\theta \, \mathrm{d}\vec{\omega} \mathrm{d}A \\
&= L_e \int_A \mathrm{d}A \int_\Omega \cos\theta \, \mathrm{d}\vec{\omega} \\
&= L_e A \pi, \qquad \text{therefore} \\
L_e &= \frac{\Phi}{\pi A}. \qquad (3.3)
\end{aligned}$$

The same deductive process can be used to solve for the emitted radiance of a diffuse two-dimensional luminaire of length Λ, a novel contribution of this thesis. This derivation uses the fact that $\int_\Theta \cos\theta \, \mathrm{d}\theta = 2$:

$$\begin{aligned}
\Phi &= \int_\Lambda \int_\Theta L_e^\flat \cos\theta \, \mathrm{d}\vec{\theta} \mathrm{d}\Lambda \\
&= L_e^\flat \int_\Lambda \mathrm{d}\Lambda \int_\Theta \cos\theta \, \mathrm{d}\vec{\theta} \\
&= 2L_e^\flat \Lambda, \qquad \text{therefore} \\
L_e^\flat &= \frac{\Phi}{2\Lambda}. \qquad (3.4)
\end{aligned}$$

For the 2D bump box, a two dimensional luminaire is formed by taking the cross section of a three dimensional polygonal luminaire. The luminaire has surface area A and total radiant flux Φ, but this presents a problem because the luminaire's power is specified for the entire surface area as it exists in three dimensions, and only a cross section is seen (the intersection of the luminaire with the plane $\mathscr{D}_c$). The radiant flux of this cross section is therefore a fraction of the whole luminaire's total flux.

This fraction can be computed as follows. The luminaire has power Φ and area A. Spread evenly over the area A is a flux density, $E = \frac{\Phi}{A}$. The Cartesian product of the area with this density gives a volume equal to the total flux of the luminaire, *i.e.*, $V = AE = A\frac{\Phi}{A} = \Phi$. The intersection of $\mathscr{D}_c$ with the luminaire yields a segment of length Λ. The *area* of the cross section of the flux volume containing this segment specifies the flux of the segment, Φ_s. Figure 3.7 illustrates this idea.

That is,

$$\begin{aligned}
\Phi_s &= \Lambda E \qquad (3.5) \\
&= \Phi\frac{\Lambda}{A}. \qquad (3.6)
\end{aligned}$$

Substituting the segment flux Φ_s for Φ in Equation 3.4 yields:

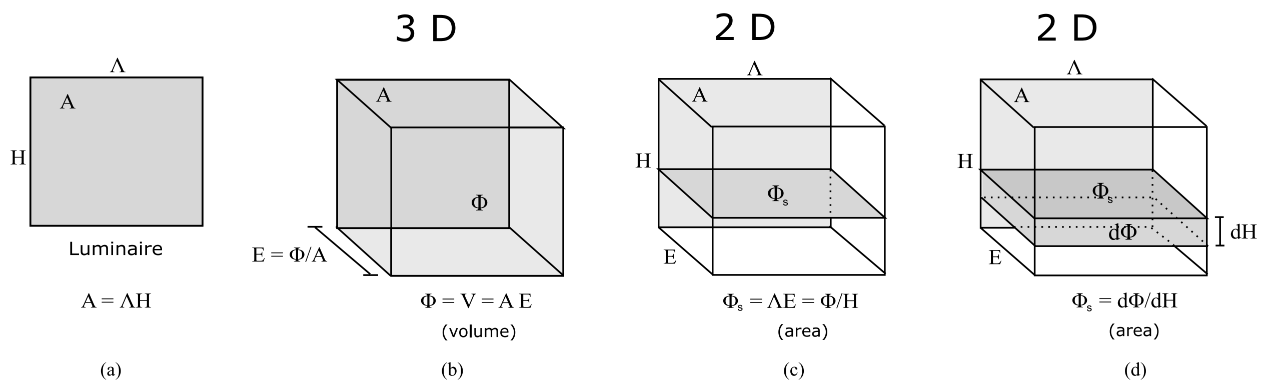

Figure 3.7: (a) A polygonal luminaire (b) In 3D the emitted flux of the luminaire is just the total flux Φ, which is the volume of the area A times the area flux density $E = \Phi/A$. (c) In 2D the emitted flux of a segment of length Λ, a cross section of the luminaire, is the area $\Phi_s = \Lambda E = \Phi/H$ of the cross section of the flux volume $V = AE = \Phi$ along the segment. (d) $\Phi_s = \Phi/H$ generalizes to $\Phi_s = \mathrm{d}\Phi/\mathrm{d}H$, where $\mathrm{d}\Phi/\mathrm{d}H$ is the ratio of the differential flux volume $\mathrm{d}\Phi$ to the differential height $\mathrm{d}H$. This is useful for when the area flux density is known but the length flux density is sought.

$$\begin{aligned} L_e^\flat &= \frac{\Phi_s}{2\Lambda} \\ &= \frac{\Phi\frac{\Lambda}{A}}{2\Lambda} \\ &= \frac{\Phi}{2A}. \end{aligned} \tag{3.7}$$

This formula for emitted radiance in two dimensions is exactly the same as the one in three dimensions (Equation 3.3) but replaces π in the denominator with 2. This particular change of constants is seen again in the Section 3.3.7, which describes the BRDF in two dimensions.

3.3.4 Direct lighting calculation

The flattened reflected radiance due to direct illumination from luminaire segments in a plane $\mathscr{D}_c$ is calculated by first finding the intersections of the 3D luminaires with the plane $\mathscr{D}_c$, calculating those segments' emissive radiances, and then integrating their direct contribution to the reflected radiance.

Calculating the position and length of the intersecting segments is straightforward; sample implementations can be found by searching the internet. Equation 3.7 relates a luminaire's total emissive flux and the length of its intersecting segment to the segment's emissive radiance. The emissive radiances for the n luminaire segments are then integrated using the following formula for the reflected flattened radiance due to direct lighting:

$$\begin{aligned} L^{\flat}_{r,d}(\vec{x},\vec{\theta}) &= \int_{\Theta} f_r(\vec{\theta},\vec{\theta}')L_{i,d}(\vec{x},\vec{\theta}')\cos\phi \mathrm{d}\theta' \\ &= \sum_{i=1}^{n}\int_{\Lambda_i} f_r(\vec{\theta},\vec{\theta}')L_{i,d}(\vec{x},\vec{\theta}')g(\vec{x},\vec{x}')\frac{\cos\phi\cos\theta_i''}{\|\vec{x}-\vec{x}'\|^2}\mathrm{d}\vec{x}' \ . \end{aligned}$$

The second equation results when the first integral is rewritten as an integration over the lengths of the luminaires rather than over the angles they subtend, by substituting $\mathrm{d}\theta'$ with $g(x,x')\frac{\cos\theta''}{\|x-x'\|}\mathrm{d}x'$, where θ'' is the angle between a luminaire segments's normal and the ray $x-x'$. The function $g(x,x') \in \{0,1\}$ is a geometry term representing whether x' is visible from x, and is determined using ray tracing. The integral is then integrated over the length of the luminaire Λ_i and finally the integrals for each of the n luminaires are summed.

3.3.5 Photon storage and emission

Photons in 3D flattened photon mapping are stored in a 3D k-d tree exactly the same as with regular photon mapping [6]. No changes are necessary. The emission algorithm, however, requires modification.

For a diffuse planar luminaire using ordinary photon mapping, the direction $\vec{\omega} \in \mathbb{S}^2$ of an emitted photon is chosen using a probability distribution over the hemisphere proportional to the cosine of the angle between the outgoing direction and the normal. Specifically, the distribution is $\vec{\omega} \sim \frac{\cos(\theta)}{\pi}$, where the constant $\frac{1}{\pi}$ is used to normalize the distribution over the hemisphere. Computing a sample from this distribution can be accomplished by choosing two uniformly distributed numbers $\varepsilon_1, \varepsilon_2 \in [0,1]$ and using the following formula from [6]:

$$\vec{\omega} = (\theta,\phi) = (\cos^{-1}(\sqrt{\varepsilon_1}),\ 2\pi\varepsilon_2) \ .$$

In two dimensions a similar cosine weighted distribution is used, however the distribution is over the hemicircle rather than the hemisphere. To reflect this change, all that needs to be done to arrive at the new distribution is to change the normalization constant from $\frac{1}{\pi}$ to $\frac{1}{2}$ since the integral over the hemicircle is $\int_{\Theta}\cos\theta \ \mathrm{d}\theta = 2$. Making this substitution yields the hemicircular probability distribution function $\vec{\theta} \sim \frac{\cos(\theta)}{2}$. Applying the Inverse Transform Method to simulate a continuous

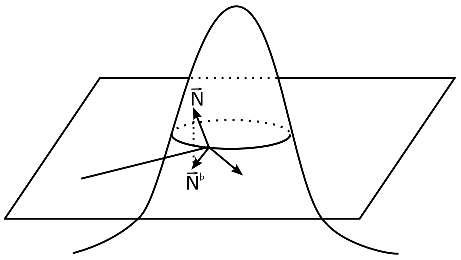

Figure 3.8: Reflectance should be about the *projected* normal, projected to the plane of incidence, $\mathscr{D}_c$.

random variable [20], the following formula for choosing a direction $\vec{\theta} \in \mathbb{S}^1$ in polar coordinates is found, using a uniformly distributed $\varepsilon \in [0,1]$:

$$\vec{\theta} = (\theta) = (\cos^{-1}(\sqrt{2\varepsilon - 1})) \tag{3.8}$$

Just as in regular photon mapping, photons should be emitted with individual flux equal to

$$\Phi_p = \frac{\Phi}{n}$$

for every photon $p \in \{1...n\}$. The justification of this is as follows. Let the extent (size) of the range of $h : \mathbb{R}^2 \to \mathbb{R}$ be denoted H. Given a rectangular luminaire with height H, width Λ, area $A = \Lambda H$, and radiant flux Φ, by using Equation 3.6 a segment of the luminaire has flattened radiant flux $\Phi_s = \Phi \frac{\Lambda}{A}$. If the luminaire is orthogonal to $\mathscr{D}_c$ and extends the entire range of h, then the relation $\frac{\Lambda}{A} = \frac{1}{H}$ can be substituted into Equation 3.6 to yield segment flux $\Phi_s = \frac{\Phi}{H}$ (and total flux $\Phi = \Phi_s H$). Using this relation, the flux of a single photon p can be expressed as:

$$\Phi_p = \frac{\Phi}{n} = \frac{\Phi_s H}{n} \tag{3.9}$$

meaning the photon carries a "flattened-flux-height" ($\Delta\Phi_s \cdot \Delta H$), in units Watts-meters. The significance of this fact is important for calculating the 3D flattened photon map radiance estimate, explained in Section 3.3.8.

3.3.6 Reflection

Reflection in flattened light transport is similar in principal to reflection in ordinary light transport, with the caveat that energy remains in the same flat plane $\mathscr{D}_c$ after being reflected. In the 2D plane

$\mathscr{D}_c$, surfaces that intersect the plane transversely, such as the graph of h, appear as curves. The curves have normals in the plane, here called $\vec{N}^\flat$, that are found by taking the surface normal $\vec{N}$ and projecting it onto the plane, as shown in Figure 3.8. $\vec{N}^\flat$ can be found by using the following formula:

$$\vec{N}^\flat = \frac{\vec{N} - (\vec{D} \cdot \vec{N})\vec{D}}{\|\vec{N} - (\vec{D} \cdot \vec{N})\vec{D}\|} \tag{3.10}$$

where $\vec{D}$ is the normal to the plane $\mathscr{D}_c$. This formula, and flattened reflection in general, are a novel contribution of this thesis.

For specular reflection, the mirror direction is found just as in ordinary 3D ray tracing, by using this projected normal $\vec{N}^\flat$:

$$\vec{v_{out}} = \vec{v_{in}} - 2(\vec{N}^\flat \cdot \vec{v_{in}}) \ .$$

For diffuse reflection, a uniform random direction should be chosen. Since the reflection must remain in the plane, there is only one degree of freedom, namely the angle $\theta \in [-\frac{\pi}{2}, \frac{\pi}{2}]$ from the projected normal $\vec{N}^\flat$. For diffusely reflecting photons, θ should have a distribution proportional to the cosine of θ, exactly the same as emission in Section 3.3.5. This angle can be found by using Equation 3.8.

3.3.7 BRDF

The BRDF relates the incident flux density from one direction to the exitant radiance in another. In three dimensions, the BRDF of a diffuse surface is a constant,

$$f_{r,d}(\vec{\omega}, \vec{\omega}') = \frac{\rho}{\pi} \ ,$$

where $\rho \in [0,1]$ is the reflectance (the ratio of reflected energy to incident energy) and $\frac{1}{\pi}$ is a normalization factor [6].

In two dimensions the normalization factor changes again from $\frac{1}{\pi}$ to $\frac{1}{2}$ because the function's domain and range are over a hemicircle rather than a hemisphere. The two dimensional diffuse BRDF is then:

$$f_{r,d}(\vec{\theta}, \vec{\theta}') = \frac{\rho}{2} \ .$$

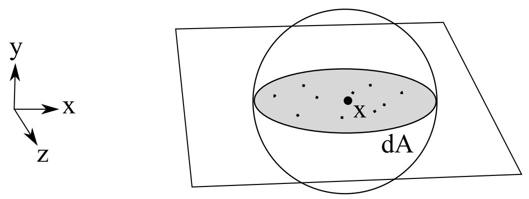

Figure 3.9: The radiance estimate in 3 dimensions is $L_r = \sum f_r(\vec{\omega}, \vec{\omega_p}') \Phi_p / \mathrm{d}A$, where $f_r(\vec{\omega}, \vec{\omega_p}')$ is the BRDF, Φ_p is the power of photon p at distance d_p, and dA is the area of a circle with radius $\mathbf{max}(d_p)$ [6].

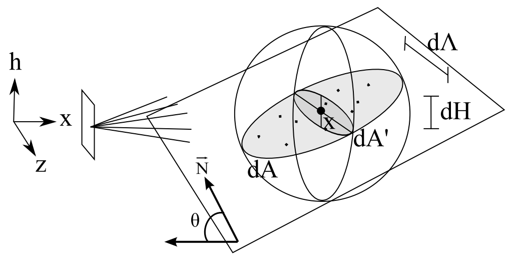

Figure 3.10: The radiance estimate in 2 dimensions is $L_r = \sum f_r(\vec{\theta}, \vec{\theta_p}') \Phi_p / (\mathrm{d}H \mathrm{d}\Lambda)$, where $f_r(\vec{\theta}, \vec{\theta_p}')$ is the BRDF, Φ_p is the power of photon p at distance d_p, and dHdΛ is the projected area dA of a circle with radius $\mathbf{max}(d_p)$.

3.3.8 Photon map radiance estimate

In ordinary photon mapping, a group of photons in a circular region is found, their flux is summed and then divided by the area of the circle to find the irradiance, or flux area density. The irradiance is then multiplied by the BRDF to get a reflected radiance.

In 3D flattened photon mapping, the BRDF must be multiplied by a flux *length* density to attain a flattened radiance value. The direct approach would be to gather photons in a small line segment, sum their fluxes, and divide by the length of the segment. Unfortunately this proves impossible to implement because the probability of finding photons in an infinitely thin segment is zero.

Therefore a volume for gathering must be used, but this presents the following problem: How is the flux of a line segment found from a volume of photons not lying on the segment? The answer, which constitutes a novel contribution of this thesis, arises from the fact that each photon flux Φ_p is really the flattened-flux-height $\Phi_s H$, according to Equation 3.9.

To arrive at a formula for the 3D flattened flux at point x on a line segment, it is assumed that photons found in a small sphere of radius d about x lie on a circular disc-shaped region dA, which is a surface in 3D, parallel to the graph of h at x. This is the same assumption that is made in ordinary photon mapping, but now a further assumption is made. See Figure 3.10 for a diagram.

This disc dA makes an angle θ with the plane $\mathscr{D}_c$ containing x, also illustrated in Figure 3.10. Depending on the angle θ, the disc region may subtend a larger or smaller height dH. It is assumed that photons in the disc region dA represent the flattened flux through a second region dA' which is the projection of the disc dA to the plane orthogonal to $\mathscr{D}_c$ and containing the line segment through x. The area of dA' has a simple relation to the area of dA:

$$\mathrm{d}A' = \cos\theta \ \mathrm{d}A\ .$$

The flux of the line segment through x is then approximated by summing the flux-height Φ_i of the photons and dividing the result by the height dH of dA', since $\Phi_s = \frac{\Phi}{H}$. This yields a total flattened flux. This flux should also be divided by the length dΛ to turn the flux into a flux length density. That is, $E^\flat = \frac{\Phi_s}{\Lambda}$. The result suggests the following formula for the flux length density $E^\flat$:

$$E^\flat = \sum_{i=1}^{n} \Phi_i \frac{1}{\mathrm{d}H\mathrm{d}\Lambda}\ .$$

The above formula has one problem. The product dHdΛ is the area of a rectangular region when it should be the area of the scaled disc, $\mathrm{d}A' = \cos\theta\ \mathrm{d}A$. Then the correct formula for the approximation of the flux length density is:

$$\begin{aligned} E^\flat &= \sum_{i=1}^{n} \Phi_i \frac{1}{\mathrm{d}A'} \\ &= \sum_{i=1}^{n} \Phi_i \frac{1}{\cos\theta\ \mathrm{d}A}\ . \end{aligned}$$

The approximation for the flattened radiance at x is then found by multiplying the flux length density $E^\flat$, also known as the flattened irradiance, by the BRDF f_r, yielding the following formula for the 3D flattened photon map radiance estimate:

$$\begin{aligned} L^\flat &= f_r\, E^\flat \\ &= \frac{\rho}{2} \sum_{i=1}^{n} \Phi_i \frac{1}{\cos\theta\ \mathrm{d}A}\ . \end{aligned}$$

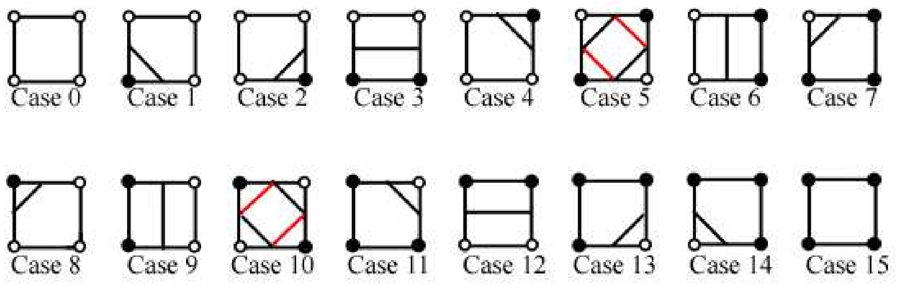

Figure 3.11: Chart showing the 15 cases for Marching Squares [8]. A case exists for each combination of the cell's corners being greater than (white) or less than (black) the isovalue. If an edge straddles the isovalue (meaning one corner is higher while another is lower), an intersection exists and is connected to other intersections according to the chart. Red lines indicate a possible ambiguity in connectivity (in these cases the connections chosen are arbitrary).

3.4 Texture generation

Since the isolines sweep out $\mathscr{D}$, a subset of a 2D plane, a 2D texture is a natural choice for storing the illumination. Storing the illumination of the isolines in a 2D texture is a novel contribution of this thesis. With a 2D scalar dataset and a 2D texture, a linear mapping exists from the domain of the surface heightfield to the texture and vice versa.

Illuminated isolines for user-selected values of isovalue c are created by using "marching squares" to produce a piecewise approximation of the line set $\mathscr{L}_c$ and then using vertex shading with texture lookups from the stored illumination texture. Marching squares operates similarly to marching cubes but in one lower dimension. For a given isovalue and 2D scalar dataset defined on a rectilinear grid, the dataset is traversed one "cell" at a time, where a cell is the smallest rectangular grouping of four dataset points. For each edge of the cell the endpoints are tested to see if they straddle an isovalue (meaning one is higher while the other is lower), and if so, an approximation of the intersection is found using linear interpolation. The edge intersection's color is found by doing a lookup in the texture with bilinear filtering. This is done for each of the four edges of the cell, and the edge intersections are connected with line segments in a nearly deterministic fashion to create a shaded approximation of the isoline through that cell. See Figure 3.11 for a chart showing the various cases of connectivity for marching squares. These cases are similar in concept to those for marching cubes shown in Figure 1.14(c). This procedure is applied to all the cells in the 2D scalar dataset, and by drawing the lines' color as a smooth blending from one endpoint's color to the other's, a colored, piecewise approximation to the isoline is displayed.

The only remaining problem is creating the texture. The texture's texels should have the property that isolines inheriting the texel's color receive the same color as if they had been rendered using global illumination. An approach to creating a texture satisfying this property is to apply it backwards: each texel is the same color as rendered isolines passing through the texel.

This approach leads to the following general algorithm:

1. Pick a point (x_i, y_i) in the domain $\mathscr{D}$ of the heightfield. This point has function height $h_i = h(x_i, y_i)$. There are now two isolines associated with this point: $\mathscr{L}_c$ which lies in the domain $\mathscr{D}$ and contains the point, and $\hat{\mathscr{L}}_c$ which lies in the plane $\mathscr{D}_c$ and contains the point (x_i, y_i, h_i). This point lies on the graph of h.

2. Determine the color of the graph at point (x_i, y_i, h_i). The color can be found by using 3D flattened photon mapping on the graph of h. The result will be the color of the point (x_i, y_i, h_i) as well as (x_i, y_i).

3. Store the color in the texture at the texel corresponding to (x_i, y_i).

Step 1, picking sample points, is discussed next in Section 3.4.1. Step 2, 3D flattened photon mapping, has already been discussed in Sections 3.3.1-3.3.8. Step 3, storing the colors, is discussed in Section 3.4.2. The results of these steps are presented in Section 3.5.

3.4.1 Sampling strategies

Sample points $(x_i, y_i) \in \mathscr{D}$ can be picked in a variety of ways. Following is a brief description of three selected strategies. The first strategy is believed to be best; the second strategy is provided as an alternative to illustrate what can go wrong when samples are placed poorly; the third strategy represents an initial, alternative approach with a serious flaw. All three sampling strategies are novel contributions of this thesis.

Uniform sampling Sample points (x_i, y_i) are chosen randomly using a uniform distribution within the domain. This is achieved by picking two uniformly and identically distributed numbers $\varepsilon_1, \varepsilon_2 \in [0, 1]$ and choosing $(\varepsilon_1 X, \varepsilon_2 Y)$ as the sample point, where $X \times Y$ is the domain of h.

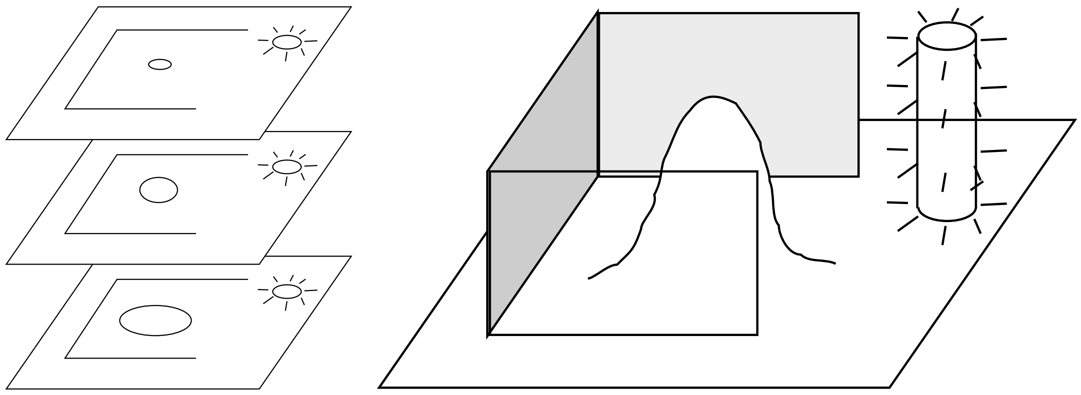
(a) Level-set illumination (b) Graph illumination

Figure 3.12: Two competing approaches to illuminating the graph of a heightfield function: (a) Sampling level sets and illuminating them in the domain $\mathscr{D}$. (b) Sampling positions on the graph and computing the illumination in $\mathscr{D} \times \mathscr{R}$ using flattened illumination.

Non-uniform sampling Sample points (x_i, y_i) are chosen poorly, in an illogical, misguided, or just plain bad fashion. This sampling strategy is presented just for illustrative purposes to show the consequence of poorly choosing sample locations.

Level-set sampling Another sampling technique is to choose several isovalues, construct the isolines through those isovalues, and then to compute global illumination solutions for the constructed isolines (perhaps using Heckbert's Flatland radiosity solver or any other global illumination algorithm for isolines). Figure 3.12(a) illustrates this strategy, which I call "level-set sampling", in contrast to illuminating the entire graph shown in Figure 3.12(b).

This sampling technique is presented to illustrate problems with the idea of explicitly constructing isolines and then subsequently illuminating them. Sampling all isovalues of a heightfield function, extracting their level set, and computing a corresponding illumination solution would require infinite computing time and infinite storage in order to store the illumination solution, so therefore the isovalues must be sampled. Many isovalues should be chosen so that the level sets through them adequately fill the domain $\mathscr{D}$ of h, incurring considerable overhead for extraction and illumination solution storage.

Choosing a good set of isovalues is non-trivial. The isovalues may be regularly spaced in the domain of h, regularly spaced in the range of h, randomly chosen, or as in this thesis, adaptively spaced [33] to minimize the maximum distance between isolines. Samples are then distributed uniformly across the chosen isolines.

No matter what technique is chosen to sample isovalues, one problem that may present itself is the *undersampling* of isovalues. If an important isovalue (and corresponding isoline) is missing then the illumination for that isoline may also be missing or inaccurate. The one-dimensional undersampling of the range of h results in an even greater undersampling of the two-dimensional domain of h by the sampled isolines. In particular, regions in the domain where the isolines are furthest apart for any two successive isovalues will be the most affected as samples are only distributed along isolines.

The idea of decoupling illumination sampling from level-set sampling, *i.e.*, rendering the *graph* of h instead of extracting individual level sets and rendering them, illustrated in Figure 3.12, is a key idea of this thesis. By decoupling sampling the illumination from level set extraction, uniform sampling has an advantage over level-set sampling in that no level sets must be extracted or stored. Doing so frees the user from having to choose the number of level sets to sample, store, and render, thereby risking under-sampling in order to save computational time and storage costs.

3.4.2 Scattered data interpolation

To create a texture given a set of sample points and their computed colors, it is necessary to merge the colors into a texture. If a sample point and color exist for every texel, then one approach is to just set every texel to the color of the sample point for that texel. However, if for some texels there are no sample points, it is then beneficial to interpolate (or extrapolate) color samples to fill in gaps due to missing sample points.

Filling in gaps in the texture is accomplished by using *scattered data interpolation*. Given a set of n samples located at positions (x_i, y_i) and having color value C_i,

$$(x_i, y_i, C_i)\,, \quad \text{for } i = 1, \ldots, n\,,$$

scattered data interpolation can be used to find a function $\bar{C}(x,y)$, defined at all points (x,y) within the domain of the heightfield, such that

$$\bar{C}(x_i, y_i) = C_i\,, \quad \text{for } i = 1, \ldots, n\,.$$

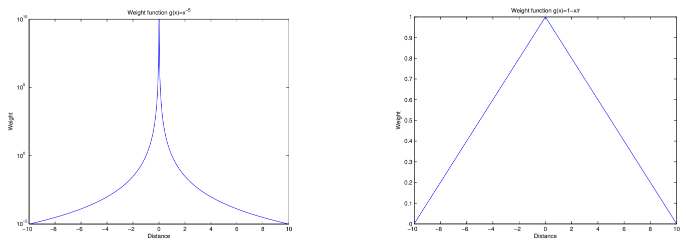

(a) Inverse power (b) Tent

Figure 3.13: Weighting functions for scattered data interpolation, as a function of distance d from a texture voxel. (a) Inverse power function, $w_i(x,y) = d^{-5}$. This function has infinite support and is shown with a log scale for the vertical axis. (b) Tent filter function, $w_i(x,y) = 1 - d/R$, where R is the radius of the filter. This function has a support of $2R$.

One of the earliest and simplest algorithms to create such an interpolation function is Shepard's method [34]. It defines the interpolating function as the weighted average of the sampled points' values, where the weights w_i for each sample point value i depend on the distance between the sample point and the evaluation point.

Figure 3.14 shows the result of using the weight function $w_i(x,y) = d^{-q}$ to interpolate 200 scattered sample point values for various exponents q, where d is the distance from the sample point to the evaluation point. Choosing $q = 5$, one weight function used in this thesis is:

$$w_i(x,y) = d^{-5}, \text{ where } d = \|(x,y) - (x_i,y_i)\|_2 .$$

This function is shown in Figure 3.13(a). The normalized interpolating function is:

$$\bar{C}(x,y) = \sum_{i=1}^{n} \frac{C_i w_i(x,y)}{\sum_{k=1}^{n} w_k(x,y)} . \tag{3.11}$$

For efficiency, it is useful to only consider sample point colors for sample points within some small maximum radius d_{max} of the evaluation point. If this is done, the summations in Equation 3.11 should be over the number of included sample points rather than n.

Another function that can be used to weight samples is a tent filter:

$$w_i(x,y) = 1 - \frac{d}{d_{max}}, \text{ where } d = \|(x,y) - (x_i,y_i)\|_2 ,$$

and d_{max} is the maximum filter radius. This function is shown in Figure 3.13(b). It has finite support, defining positive weights for distances less than the chosen filter radius d_{max}. Additionally,

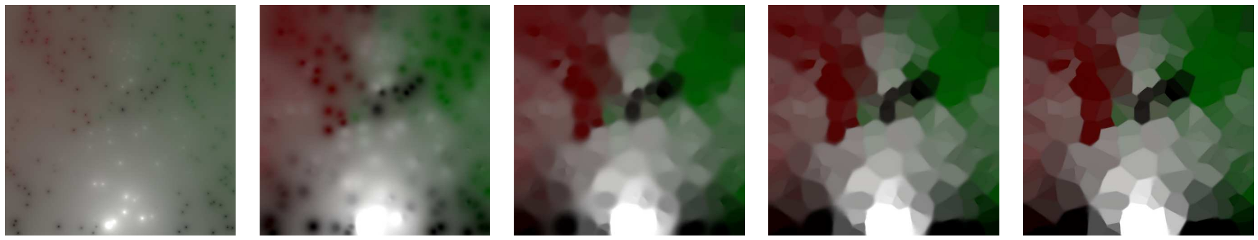

Figure 3.14: Interpolation of 200 samples into texture using weight function $w_i(x,y) = d^{-q}$, where d is the distance between (x,y) and sample point (x_i,y_i), for varying values of q. Here $d_{max} = \infty$ so all points were considered.

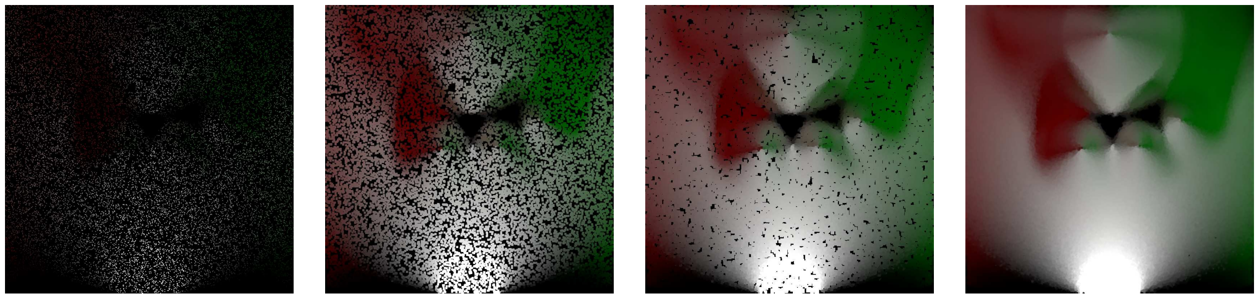

Figure 3.15: Interpolation of 20,000 samples using Equation 3.11 into a texture using sample weighting function $w_i(x,y) = d^{-5}$ for samples with distance $d < d_{max}$ for varying values of d_{max}.

it does not fulfill the preference for equivalency expressed in Equation 3.4.2. However, if d_{max} is the width of a few voxels or less it produces adequate results, sometimes better.

Figure 3.15 shows a texture being generated from 20,000 sample points by using the inverse power weighting function in Equation 3.11 and increasing the maximum distance of influence, d_{max}, for each sample. d_{max} is the maximum distance away from the evaluation point that a sample point can exist and be included in the evaluation of the interpolating function.

3.4.3 Radiance to luminance conversion

The flattened rendering equation yields radiance values which must be converted to luminance values before being displayed. Luminance values are the same as radiance values but have been multiplied by the response of the human visual system to spectral stimuli. These luminance values are the colors that are stored in an image. There are two issues to consider when computing these final colors for a surface rendered using flattened light transport.

Tone mapping

When ray tracing images, it is often necessary to use a tone mapping operator to compress the luminance values for display on a computer monitor or printed page which has, in comparison, a very low range of contrast and luminance.

Tone mapping works by first computing the global range of luminances in an image and then compressing and shifting the luminance range of all luminances so that they can be displayed on a computer screen. Typically these colors end up being represented using 24 bits, eight bits each for red, green, and blue.

Tone mapping the surface colors for the entire graph of h will produce different results than if each isoline is tone mapped individually, because in the former case the entire range of isovalues is used to compute the compression for all isolines, while in the latter case different ranges local to each isoline would be used and each would receive a unique compression.

Tone mapping each isoline individually, so that each isoline can take advantage of the full luminance range of the display, is the most desirable approach, but requires a tone mapping procedure that only considers colors in the graph of the same isovalue when computing a range for compressing them. Creating such an algorithm is beyond the scope of this thesis, so instead no compression is used while being careful to give luminaires the right power to yield reasonable brightness levels for the rendered scenes and textures. For example, the radiant flux of the luminaire in the bump box is approximately equivalent to a 90 Watt light bulb and the box is scaled to be 1 meter along each side.

Brightness correction

The emissive radiance for a diffuse luminaire in 3D is $L_e = \frac{\Phi}{\pi A}$ while in 2D it is $L_e^\flat = \frac{\Phi}{2A}$. From this difference in the emissive radiance it is easy to see why a scene rendered using flattened light transport, shown in 3.16(b), appears to be $\frac{\pi}{2} \approx 1.5708$ times brighter than a scene rendered with ordinary light transport, shown in 3.16(a). To compensate, scenes rendered using flattened light transport should have their luminance values scaled by $\frac{2}{\pi} \approx 0.6366$ in order to have similar brightness as their ordinarily rendered counterpart. Figure 3.16(c) shows the 2D bump box

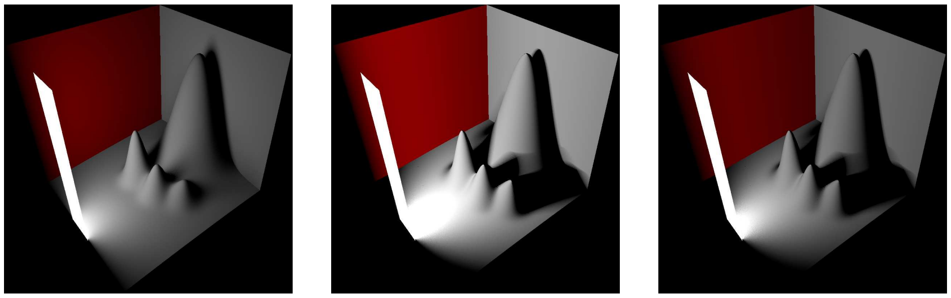

(a) 3D (b) 2D uncorrected (c) 2D corrected

Figure 3.16: (a) A surface rendered with ordinary light transport using only the direct lighting component. (b) A surface rendered with flattened light transport appears too bright by a factor of $\frac{\pi}{2}$ due to a different normalization constant. (c) The result of multiplying the final radiance by the inverse fraction $\frac{\pi}{2} \approx .6366$ more closely matches the appearance of the surface rendered using ordinary light transport.

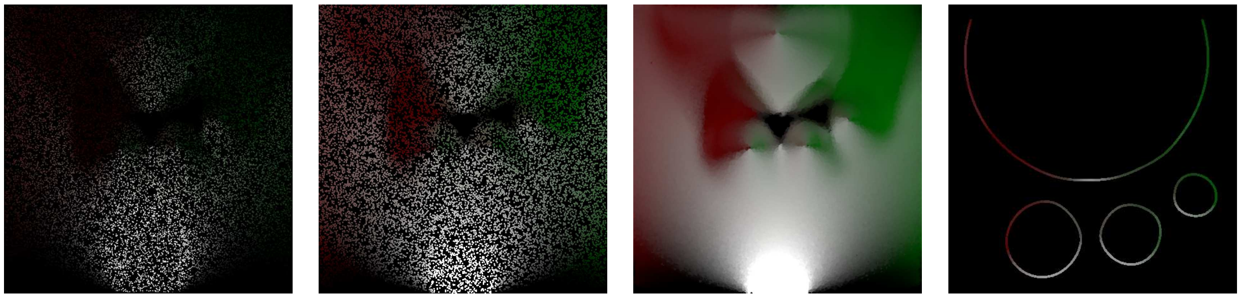

(a) Samples (b) Texture ($d_{max} = 1$) (c) Texture ($d_{max} = 16$) (d) Level set

Figure 3.17: (a) 20,000 samples uniformly spread throughout the graph of $h(x,y)$. (b) Resulting texture with $d_{max} = 1$ (c) Resulting texture with $d_{max} = 16$ (d) Colored isoline for isovalue=47.

rendered using flattened radiance after this brightness correction. This corrective factor is a novel contribution of this thesis.

3.5 Results

Results for level sets of $h : \mathbb{R}^2 \to \mathbb{R}$ for the three sampling strategies discussed in Section 3.4.1 are shown in Figures 3.17-3.19. The 2D bump box scene was used to create the textures, and 20,000 samples were used for each sampling technique. Each texture has pixel dimensions of 800x800.

A fourth reference texture was created using 10^7 regularly spaced samples in the domain $\mathscr{D}$ of

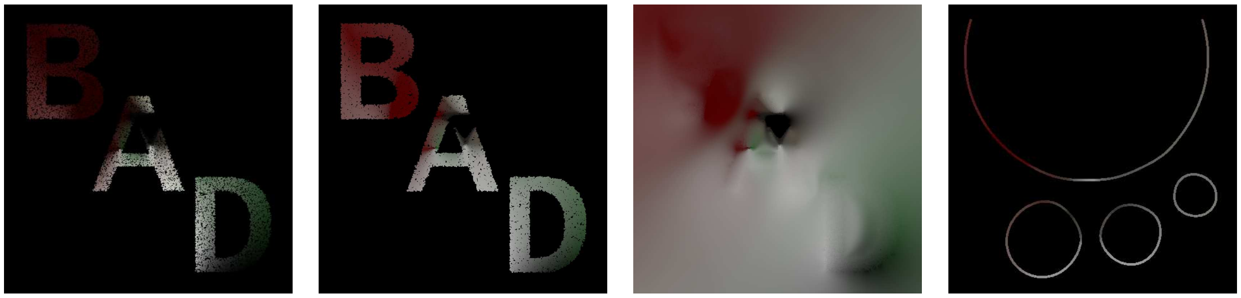

(a) Samples (b) Texture ($d_{max} = 1$) (c) Texture ($d_{max} = 566$) (d) Level set

Figure 3.18: (a) 20,000 non-uniform samples located in the region contained in the letters “B”, “A”, “D”. Note that the region at the bottom (near the luminaire) is unsampled, so the interpolated radiance there poorly matches Figure 3.20(a). (b) Resulting texture with $d_{max} = 1$ (c) Resulting texture with $d_{max} = 566$ (d) Colored isoline for isovalue=47.

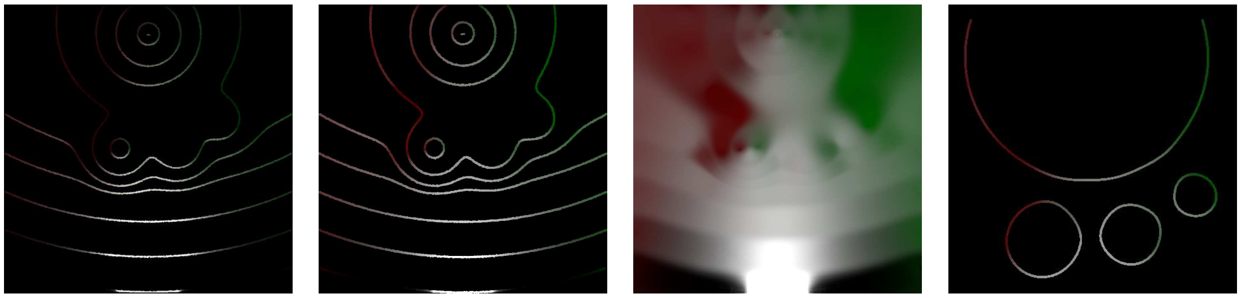

(a) Samples (b) Texture ($d_{max} = 1$) (c) Texture ($d_{max} = 400$) (d) Level set

Figure 3.19: (a) 20,000 uniform samples located along 10 level sets L_c of $h(x,y)$. (b) Resulting texture with $d_{max} = 1$ (c) Resulting texture with $d_{max} = 400$. Notice that aliasing (seen as bands) is clearly visible. (d) Colored isoline for isovalue=47.

h. A comparison of the three sampling strategies and the reference texture is shown in Figure 3.20. To determine quantitatively the accuracy of the results of the sampling strategies, the textures were compared against the reference texture by calculating their root mean square (RMS) error, where error is the difference between the measured texture and the reference texture, computed using:

$$\text{RMS error } \% = \frac{\sqrt{\langle \frac{(r_1-r_2)^2+(g_1-g_2)^2+(b_1-b_2)^2}{3} \rangle}}{100} .$$

Here (r_1, g_1, b_1) are the RGB colors for a single pixel in the texture to be compared, (r_2, g_2, b_2) are the RGB colors for the corresponding pixel in the reference surface, and $\angle\rangle$ represents a mean

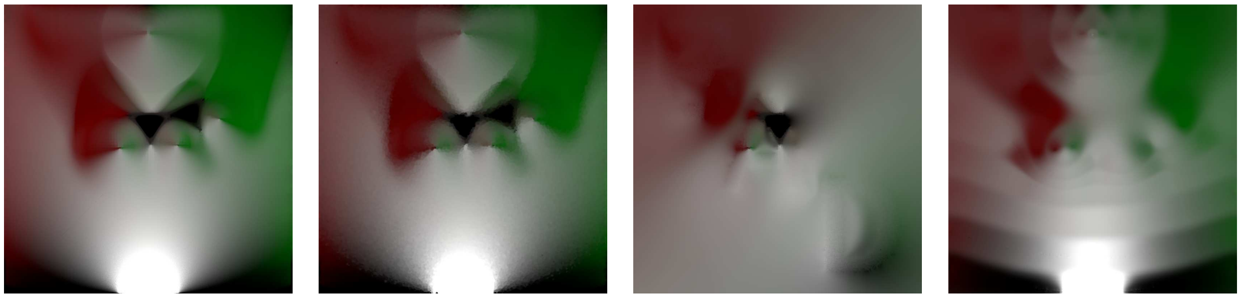
(a) Reference (b) Uniform (c) Bad (d) Level-set sampling

Figure 3.20: Textures for 2D bump box data set. (a) Reference texture, created with 10^7 regularly spaced samples (b) Uniform sampling texture, created with 20,000 uniformly distributed samples (c) Non-uniform sampling texture, created with 20,000 non-uniform samples located in the region contained in the letters “B”, “A”, “D” (d) Undersampling texture, created with 20,000 samples distributed across level sets of 10 isovalues.

operation for all pixels in the texture. Table 3.1 shows the error of the three sampling techniques, computed using this measure. As Table 3.1 shows, uniform sampling in the domain is by far the best of the three techniques.

The reasons for this are easy to identify. Non-uniform sampling, shown in Figure 3.18, has zero samples near the bright light source at the bottom of the image, completely missing that region, and others less important regions as well. This results in a large RMS error of almost 20%. Level-set sampling fairs better, as shown in Figure 3.19. However, there is noticeable banding in the texture due to the samples being concentrated along sampled level sets. Having samples roughly distributed across the domain but with banding yields an improved RMS error of about 7%. In uniform sampling the samples are more evenly distributed and thus the resulting texture shown in Figure 3.17 has no banding and an improved RMS error of only 2%. There is still some error due to the fact that the reference image has 500 times as many samples.

This chapter has covered the details of an algorithm to calculate a global illumination solution for all isolines of a 2D scalar heightfield and interactively display them. The technique, called heightfield rendering, was demonstrated by 1) using 3D flattened illumination to precompute global illumination for the heightfield, 2) storing the illumination in a 2D texture, and 3) applying the texture to interactively created piecewise approximations to the isolines.

The next chapter uses these ideas in one higher dimension to interactively create globally illuminated isosurfaces from a 3D scalar heightfield.

Table 3.1: Root mean square (RMS) percent error of textures for the bump box scene created by taking 20,000 samples with three sampling techniques. Textures were compared against a reference texture created by using 10^7 regularly spaced samples. The sampling technique with the lowest error is uniform sampling, with a RMS percent error in pixel color of 2.16%.

Samples	20,000
Sampling strategy	RMS Error (%)
Uniform	2.2
Non-uniform	18.9
Level-set	7.4

3.6 Physical bump box

In order to gain insight into the behavior and appearance of flattened light transport, I (with Hui Song, Brad Futch, David Banks) created a physical version of the 2D bump box in order to demonstrate flattened light transport in the real world.

The Master Craftsman program at FSU assisted in this endeavor by sculpting a model of the 2D bump box function This model was then placed in a fish tank with colored walls made out of posterboard painted to match the walls of the 2D bump box scene. A light segment was constructed by channeling a fluorescent light through a 1 cm thick slab of lucite. Figure 3.21(a) shows this light illuminating the physical bump box in an otherwise dark room.

In order to simulate flattened radiance, the tank was partially filled with water and a thin layer of mineral oil was floated on top. The height of light was adjusted so that the light shone into the oil. Mineral oil has a higher refractive index (1.5) than air (1.0) and water (1.3), causing light propagating in the oil layer incident to the air interface to achieve total internal reflection for angles less than 48° from horizontal, and similarly for angles less than 29° for the water interface. Ideally, under these circumstances all light within 29° of horizontal will remain inside the layer of oil, using the same principles that allow light to travel over 80 kilometers inside a fiber optic cable [35].

Figure 3.21(b) shows a slice of the graph sculpture illuminated in this manner. A significant amount of light was escaping the oil into the water below and causing and illuminating the underlying graph. To better isolate the oil layer, black tempera paint was added to the water, shown in Figure3.21(c).

Water was added to the tank to raise the oil layer and at each height photographs were taken of the scene from two different angles. These photographs were then assembled to produce the

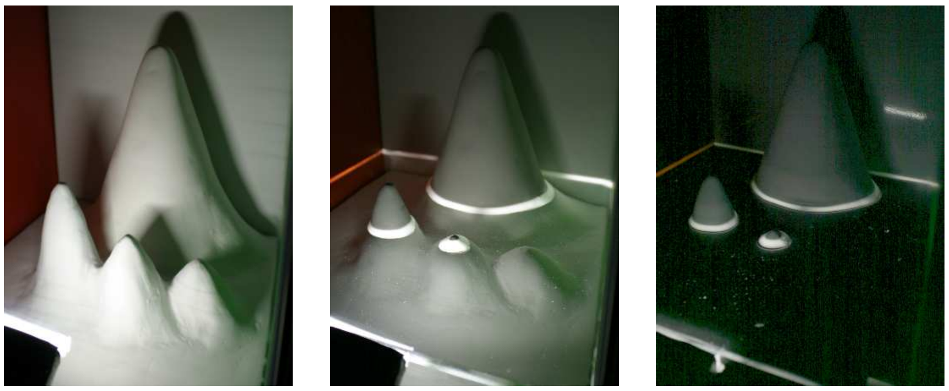
(a) Empty (b) Water + Oil layer (c) Water + Ink + Oil

Figure 3.21: The bump box illuminated by a line segment.

images shown in Figures 3.22(c) and 3.22(d). Figures 3.22(c) and 3.22(d) show the results of flattened radiance for comparison and are provided for comparison.

Several problems were encountered in this undertaking, such as persistent water bubbles in the oil, too thick of an oil layer, too long of a camera exposure, light bouncing off the graph and leaving the oil layer, non-ideal-diffuse reflection and emission, etc. Despite these problems, the setup illustrates the nature of flattened light transport within a 2D leaf of $\mathbb{R}^3$, and gives a result that is qualitatively consistent with flattened light transport.

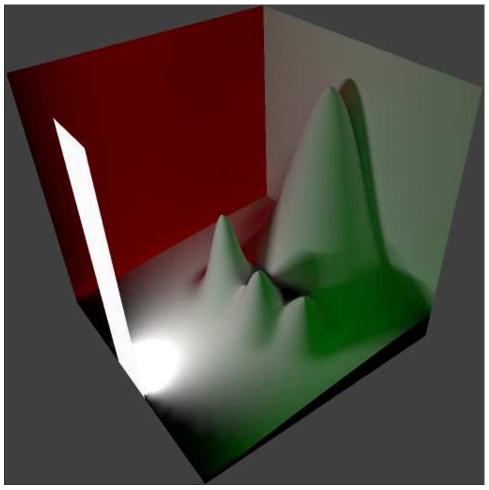
(a) Rendering

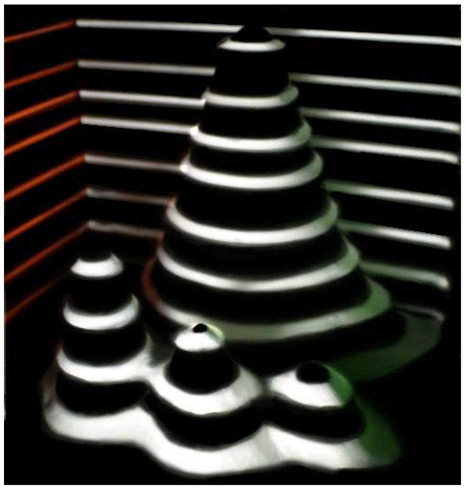
(b) Physical bump box

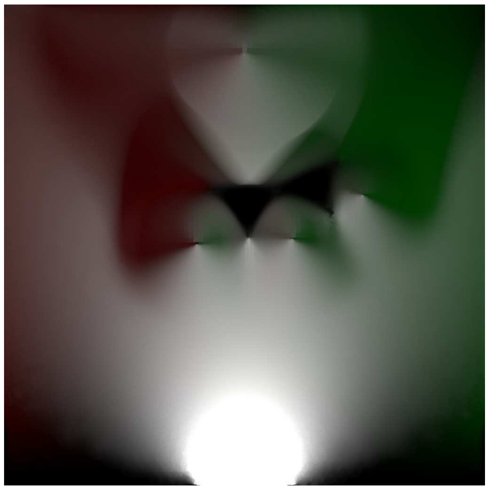
(c) Rendering

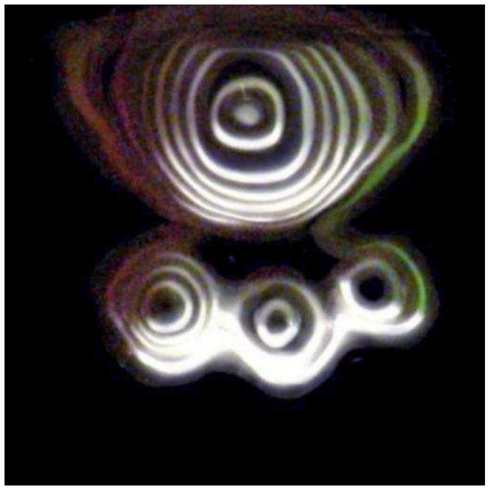
(d) Physical bump box

Figure 3.22: Illuminating the bump box. The upper row shows the function $f : \mathbb{R}^2 \to \mathbb{R}$ graphed as a height field in $\mathbb{R}^3$. The lower row shows the illumination grid, which is the height field's color as seen from overhead, projected to the domain of f.

CHAPTER 4

ILLUMINATING A HEIGHTFIELD VOLUME

This chapter explains how to display isosurfaces from a 3D scalar heightfield $h : \mathbb{R}^3 \rightarrow \mathbb{R}$ with global illumination at interactive rates. The steps involved are: (1) solving a modified (flattened) version of the light transport equation on the graph of h, (2) storing the solution in a 3D texture, and (3) applying the texture to a piecewise approximation of an isosurface. The result is an isosurface displayed with the interactive speed of hardware local illumination but with the high-quality appearance of being rendered with global illumination, including the same valuable interpretative cues such as shadows and inter-reflection.

4.1 Ordinary illumination

The graph of a three dimensional volume heightfield $h : \mathbb{R}^3 \rightarrow \mathbb{R}$ exists in four dimensions because $\mathscr{D} \times \mathscr{R} = \mathbb{R}^3 \times \mathbb{R} = \mathbb{R}^4$. Ordinary illumination of such a graph in which light flows freely throughout all four dimensions is both difficult to imagine and illustrate. The emittance becomes a function of three variables $(\phi,\ \theta,\ h)$ and the BRDF becomes a function of six variables $(\phi_{in},\ \theta_{in},\ h_{in},\ \phi_{out},\ \theta_{out},\ h_{out})$. Banks [36] [37], Hollasch [38], and Hanson *et al.* [39] discuss diffuse and specular reflection of surfaces in four dimensions. but do not address full global illumination. Full global illumination in four dimensions is an area of possible future research.

4.2 Flattened light

Recall from Section 3.2 that 3D flattened light transport is light transport restricted to remaining within originating leaves of dimension $\mathbb{R}^2$ for flattened light transport in $\mathbb{R}^3$. In general, flattened light transport for dimension $\mathbb{R}^n$ is light transport with the restriction that light remains in its emitting leaf of dimension $\mathbb{R}^{n-1}$ during emission and reflection.

In physics, brane cosmology postulates that the 4D universe exists as a “brane” in a higher dimensional space [40]. According to this protoscience, the electromagnetic, weak, and strong forces interact exclusively within the 4D 4-brane of our universe while the gravitational force can interact outside the brane with other branes in the higher dimensional space, thus “leaking” and explaining gravity’s relative weakness compared to the other forces. Scientists are currently investigating this leaking phenomenon, in the search for a grand unification theory.

In the case of a heightfield volume a level set is a 3D surface (a leaf of the graph) existing in a 3D subset of 4D space (a leaf of $\mathbb{R}^4$). The level set and this 3D subset of space can be considered to be a 3-brane existing in the 4D space of $\mathscr{D} \times \mathscr{R}$. Flattened light transport occurring on the 4D graph of a heightfield volume is the transport of light where light must remain in its originating 3D leaf of $\mathbb{R}^4$. Within this 3D leaf, or space, or 3-brane, light transport operates exactly the same as normal light transport for 3D surfaces. The only difference is that the 3D surfaces are slices of a four dimensional graph, *i.e.* level sets. In the brane analogy, flattened light would be akin to the electromagnetic force in that it operates entire within the brane without leaking to any other brane, as opposed to gravity which is (theoretically) free to move between branes. The defining characteristics of 4D flattened light transport are:

- Luminaires emit only within the 3D leaf $\mathscr{D}_c$ where $h = c$.
- Reflection occurs only within the 3D leaf $\mathscr{D}_c$ where $h = c$.

Within the 3D leaves of $\mathbb{R}^4$ light transports in the ordinary fashion. This result is reversed from the case for a surface heightfield, where ordinary light transport was easy while flattened light transport required new emission and reflection models.

In contrast, depicted in Figure 4.1, for a heightfield volume, 4D emittance is difficult to imagine, but 4D flattened emittance is the same as ordinary 3D emittance:

Ordinary 4D light transport:	$E : \mathbb{S}^3 \to \mathbb{R}^1$	(Difficult)
Flattened 4D light transport:	$E^\flat : \mathbb{S}^2 \to \mathbb{R}^1$	(Routine; same as 3D emittance E).

Similarly, a six dimensional 4D BRDF is formidable while a 4D flattened BRDF is the same as an ordinary 3D BRDF, and is easy because it is already understood by using ordinary light transport:

Ordinary 4D light transport:	$f_r : \mathbb{S}^3 \times \mathbb{S}^3 \to \mathbb{R}^1$	(Difficult)
Flattened 4D light transport:	$f_r^\flat : \mathbb{S}^2 \times \mathbb{S}^2 \to \mathbb{R}^1$	(Routine; same as 3D reflectance f_r).

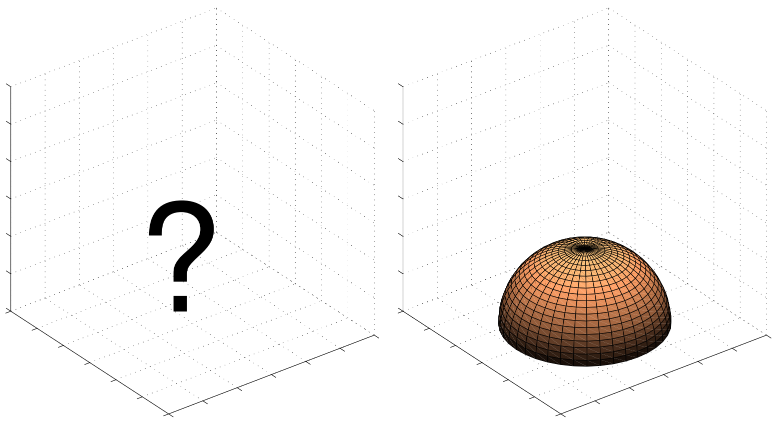

Figure 4.1: Left: The emittance distribution $E : \mathbb{S}^3 \rightarrow \mathbb{R}^1$ for 4D light transport is difficult to imagine and draw. Right: The emittance distribution $E^\flat : \mathbb{S}^2 \rightarrow \mathbb{R}^1$ for 4D flattened light transport is just the same as in ordinary 3D light transport: a hemisphere.

4D flattened light transport behaves the same as ordinary light transport because it is the same; the only change is that the space the light travels in is a 3D leaf of the 4D space containing the 4D graph of the volume heightfield, h, and the 3D surface it interacts with is a leaf of the graph, *i.e.*, a level set.

4.3 Ray tracing a 4D graph

4.3.1 Flattened radiance

Flattened radiance for a heightfield volume uses the same definition of radiance as ordinary light transport and uses nearly the same rendering equation. Indeed,

$$L^\flat \text{ in 4D} \equiv L \text{ in 3D} ,$$

and more specifically,

$$L^\flat(\vec{x}, h(\vec{x}), \vec{\omega}) \equiv L(\vec{x}, \vec{\omega}) = \frac{\mathrm{d}^2\Phi}{\mathrm{d}A \cos\theta \, \mathrm{d}\vec{\omega}} .$$

Differences in computing $L^\flat$ arise out of the fact that the equation is now being applied to a continuous set of surfaces: the graph of h. The 4D flattened rendering equation, shown in Equation 4.2,

$$\text{Ordinary} \qquad L(\vec{x},\vec{\omega}) = L_e + \int_\Omega f_r(\vec{\omega},\vec{\omega}')\, L_i(\vec{x},\vec{\omega}')\, (\vec{N}\cdot\vec{\omega}')\, \mathrm{d}\vec{\omega}' \tag{4.1}$$

$$\text{Flattened} \qquad L^\flat(\vec{x},\vec{\omega}) = L_e^\flat + \int_\Omega f_r^\flat(\vec{\omega},\vec{\omega}')\, L_i^\flat(\vec{x},\vec{\omega}')\, (\vec{N}\cdot\vec{\omega}')\, \mathrm{d}\vec{\omega}', \tag{4.2}$$

is functionally equivalent to the original rendering equation, shown in Equation 4.1 and recalled from Section 1, and appears nearly the same. However, it represents flattened light transport interacting with a 4D graph of a 3D scalar function, and its notation is altered to reflect the difference. Here $L_r^\flat$ is the 4D flattened radiance, $f_r^\flat$ is the 4D flattened BRDF, $L_i^\flat$ is the incident 4D flattened radiance, and the other variables are the same as in the original rendering equation (Equation 1.1). This formulation of light transport within $\mathscr{D}_c$ is a novel contribution to the theory of rendering.

4D flattened reflection is exactly the same as ordinary 3D reflection, with the restraint that the reflecting radiance remains in the same 3D leaf of $\mathbb{R}^4$. Therefore the 4D flattened BRDF is equivalent to an ordinary 3D BRDF. That is, $f_r^\flat$ in 4D $\equiv f_r$ in 3D.

In heightfield rendering the goal is to sample the flattened radiance, or illumination, of the graph of the heightfield function, and store the illumination in a 3D texture. The position in the texture is linearly related to the projection of the graph sample to the 3D domain of the heightfield (the position of $\vec{x}$ within the domain).

4.3.2 Solving the flattened rendering equation efficiently

For each sample point of the graph, the illumination is found by solving the 4D flattened rendering equation in Equation 4.2. Rather than performing straight Monte Carlo path tracing and suffering the low quality and slow speed associated with that technique, it is advantageous to apply a more efficient algorithm such as photon mapping. Building on the ideas presented in Chapter 3, the following sections detail the changes necessary in order to alter photon mapping to solve the 4D flattened rendering equation. This new version of photon mapping, called “4D flattened photon mapping,” can be used to compute the flattened illumination on the graph of a volume heightfield, and concomitantly on the isosurfaces that foliate the graph.

4.3.3 Scene extrapolation

First, the level sets (or the whole graph) should be placed in a scene containing at least one light source in order to provide illumination. Alternatively the level sets could emit their own

Table 4.1: Psuedocode for augmented ray data structure.

```
// ray data structure
class Ray {
  Vec3D pos;          // origin position
  Vec3D dir;          // direction (normalized)
  float c;            // isovalue
}
```

illumination. This is entirely left up to the designer of the scene. In any case, the simplest solution is to use the same scene for all level sets of the heightfield function. This is achieved by placing the graph and the surrounding scene together in an appropriate data structure, and considering the scene to exist for each level set of the function. In effect, each triangle of the scene (if the scene is composed of triangles) is extruded through the range of h, to become a volume, namely a triangular prism, stretching through the entire range of h.

The function h is defined over a regular grid, where each point in the dataset represents a function value. A cubic grouping of eight data points is called a cell. Each cell is a four dimensional volume, having level sets in the form of 3D surfaces throughout the cell.

4.3.4 Ray intersections

In order to perform photon mapping, and ray tracing in general, it is necessary to be able to intersect rays with the scene and the graph. Intersecting rays with the scene and the heightfield volume is simplified because of flattened illumination. Since light transport is restricted to constant level sets, light only moves through space and not through the fourth dimension, the range of h.

Definition of ray

Likewise, rays only move through the 3D space where h is constant and remain static in the fourth dimension, or range of h. They propagate in the same subspace where they are emitted. The data structure for such a ray is realized by simply appending a constant $c \in \mathscr{R}$, representing the leaf $\mathscr{D}_c$ the ray is in, to the regular 3D position and 3D direction that normally describe a ray, as shown in Table 4.1.

Ray-prism and ray-graph intersection generally proceeds by examining prisms and data cells along the ray, and checking them, in order, to see if the ray intersects each, and choosing the first intersected object (the one closest to the origin of the ray).

Ray-prism intersection

Rays are intersected with the triangular prisms by first checking that the ray's c-value is within the range of isovalue-space that the triangular prism extends. If this is true, then the ray is tested against the triangle face using ordinary ray-triangle intersection, ignoring any extra fourth dimension. Since the prisms are considered to span the entire range of isovalues (the entire range of h, or $\mathscr{R}$), the first test is always true and can be skipped, resulting in ordinary ray-triangle intersection [41].

Ray-graph intersection

Ray-graph intersection is initially the same as ray-prism intersection. First the ray's c-value is compared against the extent (min and max) in isovalue-space (range of h) of the eight data points making up the data cell. If the ray's c-value is within this isovalue range of the data cell, then further checking is required to see if the ray intersects the isosurface of the data cell with isovalue c.

To accomplish this the "Ray-Isosurface Intersection for Trilinear Boxes" test described in appendix A of Parker *et al.* [9] is used. The eight function values at the corners of the cell are interpolated to find the function value within the volume using trilinear interpolation. Given a cell with coordinates and function values labeled $(x_i, y_j, z_k, h_{ijk})\ \forall\, i,j,k \in 0,1$ as shown in Figure 4.2, the function value in the interior is given by the following function [9]:

$$\begin{aligned} h(u,v,w) = (1-u)(1-v)(1-w)h_{000} + (1-u)(1-v)(w) \qquad & h_{001}+ \\ (1-u)(v)(1-w)h_{010}+ & \\ (u)(1-v)(1-w)h_{100}+ & \\ (u)(1-v)(w)h_{101}+ & \\ (1-u)(u)(v)h_{011}+ & \\ (u)(v)(1-w)h_{110}+ & \\ (u)(v)(w)h_{111}, & \end{aligned} \tag{4.3}$$

where

$$u = \frac{x-x_0}{x_1-x_0} \qquad v = \frac{y-y_0}{y_1-y_0} \qquad w = \frac{z-z_0}{z_1-z_0}.$$

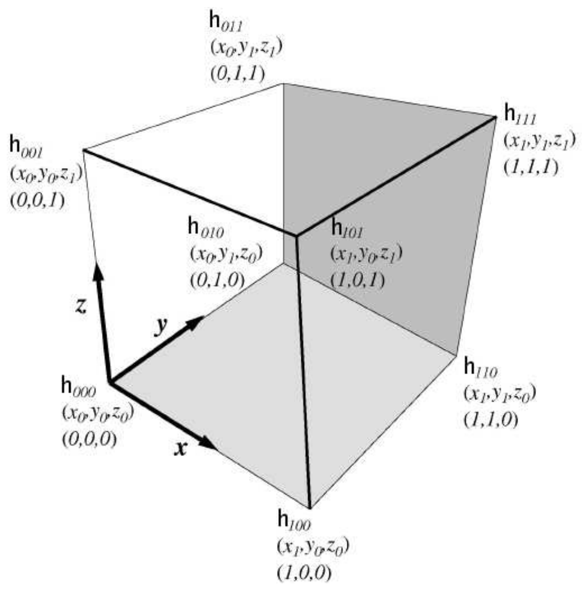

Figure 4.2: Labelling of a cell. The cell's corner are eight neighboring voxels in a rectilinear grid, a small piece of a volume heightfield $h : \mathbb{R}^3 \rightarrow \mathbb{R}$. Figure reproduced from [9] Fig. 15

.

Recall a ray's position is given by the ray equation:

$$\vec{r} = \vec{o} + t\vec{d}.$$

To intersect a ray with the interpolated interior of a cell, Parker *et al.* derive a function $h(\vec{r})$, similar to Equation 4.3, yielding the interpolated function value of a point along the ray $\vec{r}$ as a function of the a ray and its parameter t. Setting $h(\vec{r})$ equal to the ray's function value c and simplifying produces a cubic polynomial equation in t. Solving the cubic equation for t and substituting into the ray equation yields the position of the intersection of the ray with the isosurface of the interpolated function; if the intersection is *within* the cell then the ray intersects the cell at that point. If there is no intersection or if the intersection is outside the cell then no intersection is considered to exist. The definition and derivation of $h(\vec{r})$ that Parker *et al.* provide [9] contains a slight error. For the full and correct definition see Appendix A.

To solve the cubic equation, I follow Parker *et al.*, and use the source code given in an article by Schwarze [42], available online at numerous *Graphics Gem* archives. However, two modifications to his code must be made. First, the constant EQN_EPS should be changed to 1.0e-30 for maximum stability. Additionally, special cases for when the cubic equation is really a quadratic or linear equation must be added. This happens when the leading coefficients are sufficiently close to zero, *i.e.*, less than 1.0e-8. A few iterations of root polishing [43] should be applied to counter any numerical instability, and finally, as mentioned above, it should be verified that the intersection is within the cube and not outside of it, since any extrapolated function values are invalid outside the cube.

Ray-object intersection acceleration

For ray-object intersection acceleration the scene's triangular prisms and the heightfield function's four-dimensional cells are placed into a octree data structure [24] augmented with isovalue bounding interval information for each voxel [44]. For example, the octree voxels containing prisms would have bounding values h_{min} and h_{max} equal to the minimum and maximum values of the heightfield, respectively. Another choice is $-\infty$ and ∞, respectively, which is fine as long as the prisms' extent in the fourth dimension h is greater than or equal to the graph's extent, and the octree voxels that contain prisms have an extent greater than or equal to the prisms' extent in h. For an octree voxel containing a cell or group of cells, h_{min} is equal to the minimum value of h for every grid point in every cell within the octree voxel, and similarly for h_{max}. This type of data structure is called an interval octree, and was first developed by Wilhelms and Gelder [44]. The main idea is that during traversal of the octree, only children whose bounding interval contains the ray's isovalue c are traversed.

Unlike Wilhelms and Gelder, I do not use a Branch On Need Octree (BONO) but instead use an octree with regular midpoint subdivision, for simplicity. However, I take care to position the octree center and initial size such that upon a small, sufficient number of subdivisions each octree leaf voxel contains exactly one whole cell. Of course, the presence of scene prisms may cause further subdivision. This voxel-cell matching is ensured by positioning the initial voxel's center at one of the corners of the domain of h and making its initial size a power-of-2 times the size of the domain $\mathscr{D}$ such that it is large enough to enclose the graph and the scene also.

A ray traverses the augmented octree by traditional methods, such as the parametric algorithm in Revelles *et al.* [45], with additional tests to first see if the ray's isovalue c is within the isovalue range of each octree voxel (that is, between h_{min} and h_{max}), before traversing that voxel. In this way, a ray will traverse only those octree voxels along its path containing scene geometry or data cells with c inside their bounding intervals of h. If a ray's c-value is within the bounding interval of a cell, then ray-prism and ray-cell intersection are used, as described in Sections 4.3.4 and 4.3.4.

4.3.5 4D photon mapping

Flattened illumination has a similarity in problem scope with another area of computer graphics: ray tracing moving scenes (motion blurring). In scenes where objects move, a fourth dimension, time, is present. Cammarano and Jensen derived a time-dependant radiance estimate using a single photon map for scenes with a continuous time domain [10]. I adapt their technique to use a single photon map for the entire volume heightfield while still being able to estimate the radiance at positions on individual isosurfaces. This estimate has only a very small dependance on the location of neighboring isosurfaces. The next sections describe implementing this 4D photon mapping technique.

Photon storage, emission, and reflection

First the photon data structure is modified to store a 4D position for the photon, augmenting the 3D position with a fourth value describing the photon's position in the range of h (like the c-value for rays). Similarly the 3D kd-tree used to store the photon map becomes a 4D kd-tree with four splitting dimensions [6]. This is a very simple and straightforward modification of Jensen's original 3D kd-tree nearest neighbor search [6].

Photons emit and reflect off the graph of h, remaining in their original subspaces $\mathscr{D}_c$ (leaves of $\mathbb{R}^4$) where $h = const$. For emission, the c-values of photons are uniformly distributed in the range of h and remain constant during reflection and absorption. Each photon's power is scaled by the extent of H, *i.e.*, $h_{max} - h_{min}$, similar to Section 3.3.5 and Equation 3.9, and thus really carries "flux-height." This is necessary in order to reconstruct the flux of points on individual isosurfaces, detailed in the next section. The formula for the flux-height of an emitted photon is:

$$F_p = \frac{\Phi H}{n}, \qquad p \in 1, 2, 3, \dots n \tag{4.4}$$

where F_p is the flux-height of a single photon p, Φ is the power (in Watts) of the light source, and H is the extent of the range of h, where $H = h_{max} - h_{min}$.

Photons are emitted exactly the same as in ordinary photon mapping, except their fourth dimensional coordinate (c-value) is initialized with a random value from the range of h. The photon is then propagated into the scene and graph, taking care to only reflect off of isosurfaces of the same c value and scene elements (the triangular prisms which extend through the fourth dimension). The c-value never changes and determines what level set the photon can interact with.

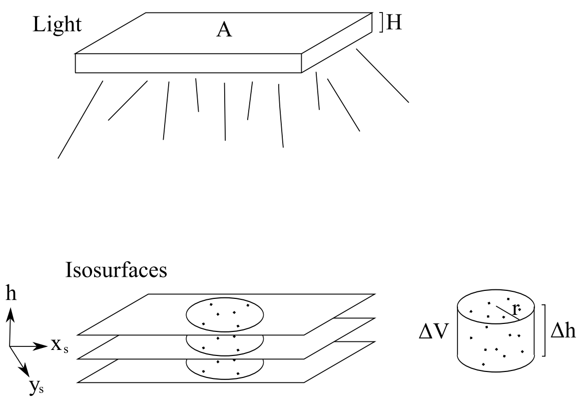

Figure 4.3: Top: Photons emit from a light carrying "flux-height". Bottom: (Left) The photons collect in leaves of the graph of h. (Right) A cylindrical volume of photons, extending through both the domain and range of h, is found in order to make a radiance estimate. The flux-height of the photons is added and the sum is divided by the height of the cylinder to yield the approximate flux. This flux is then divided by the surface area of the top of the cylinder, $A = \pi r^2$, to find the flux-area-density E.

The projection of the 4D photon map into the 3D domain of the function h will form a 3D volume of photons, which can be displayed as 3D points for debugging and visualizing the photon map.

Radiance estimate

To estimate the radiance at a point $(\vec{x}, h(\vec{x}))$ on the graph of h, the photons in a small region near $\vec{x}$ are located. In ordinary photon mapping, the photons are assumed to lie on a flat surface and the summed photon power is divided by the 2D disc area to find the flux area density (irradiance).

In 4D photon mapping, the photons in the vicinity of $\vec{x}$ are distributed spatially through the domain, lying on separate isosurfaces within various neighboring leaves of $\mathbb{R}^4$, as shown in Figure 4.3. Simply choosing a single isovalue and only including photons of that isovalue would select at most one photon since they are distributed uniformly through the range of h [1]. This is a problem because the accuracy of the photon-map-based radiance estimate is related to the number of photons used in the estimate, so several photons are desired but they lie on different isosurfaces.

Cammarano and Jensen solved a similar problem in an effort to produce a time-dependent photon map radiance estimate. They needed an accurate estimate for ray tracing motion-blur using

[1] The figure is slightly inaccurate as each photon very likely exists in its own unique leaf.

Photon Mapping, which involves taking time-dependent radiance samples and averaging. In such a scenario, emitted photons are distributed throughout a small time window (the shutter time of the camera). Since their scene may be moving, meaning the position of each surface depends on time, the photons may be spread out spatially or grouped together as the surface interacting with them moves. If a radiance estimate is made using neighboring photons regardless of their time, then the radiance estimate will be too small or large depending on whether the photons are spread apart or grouped together, respectively. They solve this problem by only using those photons nearest a point in *time* as well as space, using a formula they derived for estimating the radiance using photons from a subset of a larger time. They accomplished this by premultiplying the flux of the photon by the total shutter time, causing the photon to carry energy rather than flux. This solution can also be applied to 4D photon mapping where the fourth dimension is the value of a function h and the moving surfaces are level sets. By substituting the range of $h : \mathbb{R}^3 \to \mathbb{R}$ for time, their formulas can be used to make an h-dependent photon map based radiance estimate. Instead of premultiplying by time, the photon's flux is multiplied by the extent of the range H.

Consider a small continuous set of isosurfaces collecting photons in Figure 4.3. The flux for the isosurfaces can be approximated by summing the flux-height of the photons within the cylindrical volume region V and dividing by the height Δh of the volume, *i.e.*, its extent through the range:

$$\Phi = \frac{\sum F_p}{\Delta h}.$$

The flux area density, or irradiance E, for the isosurfaces is then approximated by dividing the estimated flux by the surface area, which is equal to the area of the top of the cylinder, ΔA:

$$\begin{aligned} E &= \frac{\text{flux}}{\text{area}} && (4.5)\\ &= \frac{\Phi}{A} && (4.6)\\ &= \frac{\sum F_p}{\Delta A\,\Delta h}\;. && (4.7) \end{aligned}$$

Multiplying the irradiance by the BRDF yields an approximation to the 4D flattened reflected radiance $L_r^\flat$:

$$L_r^\flat = f_r^\flat \sum_{i=1}^{n} \frac{F_p}{\Delta A\,\Delta h}\;,$$

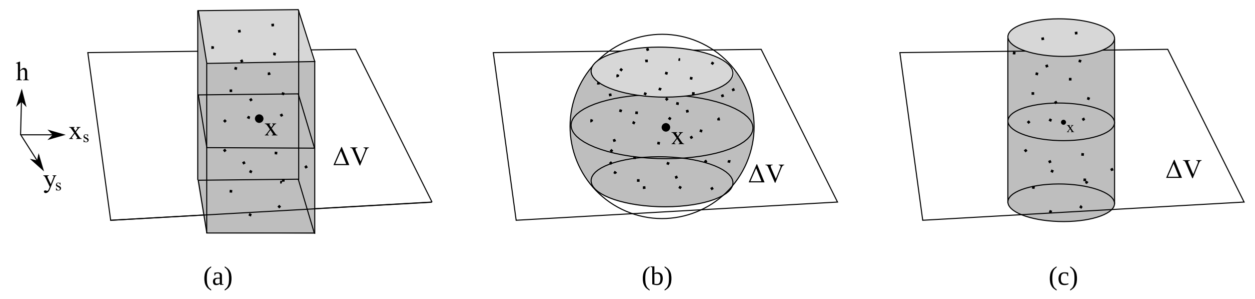

Figure 4.4: The radiance estimate in four dimensions is $L_r^\flat = f_r^\flat \sum F_p/\Delta V$, where f_r is the BRDF, F_p is the flux-height of photon p at distance d_p, and $\Delta V \approx \Delta A \Delta h$ is the volume of the region containing the photons. Shown are three possible choices of volumes to use in an estimate. (a) uses a box region (b) uses a clipped sphere (c) uses a cylinder. My implementation uses the clipped sphere (b) for simplicity when doing a photon search in the photon map (a four dimensional kd-tree) [10].

where $f_r^\flat$ is the BRDF. Instead of dividing by the product of the area ΔA and height Δh, one can just divide by the *volume* ΔV, which is equivalent. The general formula for the photon map based radiance estimate is:

$$L_r^\flat = f_r^\flat \sum_{i=1}^{n} \frac{F_p}{\Delta V}. \tag{4.8}$$

In general, any volume may be used, but note that only two of the dimensions of the volume are spatial, spanning a small approximate surface area, and the third is in the range of h. Three examples of volumes for making an estimate: a rectangular box, a sphere, and a cylinder, are shown in Figure 4.4.

The sphere volume is easiest to use because of the simplicity in doing a nearest-photon search. To do this, the n photons nearest $\vec{x}$ are found using the distance metric

$$d = \sqrt{\Delta x^2 + \Delta y^2 + \Delta z^2 + \Delta h^2}.$$

This search is accelerated using the 4D kd-tree and is very fast. The photons occupy a four dimensional spherical volume of radius r, and are distributed through the spatial domain $\mathscr{D}$ and the range $\mathscr{R}$ of h, as illustrated in Figure 4.4(b). The summed flux-height of photons in the spherical region is divided by the volume of the $(\vec{x}_s, \vec{y}_s, \vec{h})$ sphere where $\vec{x}_s$ and $\vec{y}_s$ are tangent to the isosurface, and have length r. This flux area density is then multiplied by the BRDF, yielding the reflected radiance:

$$L_r^\flat = f_r^\flat \sum_{i=1}^{n} \frac{F_p}{\frac{4}{3}\pi d_{\max}^2}.$$

The range of h has a different scale than the spatial domain. For example, in some datasets the domain is arbitrarily considered to be from $(0,0,0)$ to $(100,100,100)$. However the range may be from 0...255 or 0...1, depending on the data. Furthermore it may be desirable to search more or less closely in the range near the sample point $\vec{x}$ than in the domain. Both of these problems are resolved by *scaling* the sphere along the axis corresponding to the range of h. This can be achieved quite simply in the case of the spherical volume by modifying the distance metric d with a scalar constant κ:

$$d = \sqrt{\Delta x^2 + \Delta y^2 + \Delta z^2 + (\kappa \Delta h)^2}.$$

When estimating the radiance it is necessary to use the formula for the volume of a scaled sphere, $\Delta V = \frac{4}{3\kappa}\pi d^3$, yielding the following radiance estimate:

$$L_r^\flat = f_r^\flat \sum_{i=1}^{n} \frac{F_p}{\frac{4}{3\kappa}\pi d_{\max}^3}, \tag{4.9}$$

where $d_{\max}$ is the distance of the furthest photon, using the distance metric in Equation 6. As Cammarano points out, κ is an unintuitive parameter. A formula for κ that scales the sphere to a fraction g of the spatial size is:

$$\kappa = \frac{\max(|\mathscr{D}_x|, |\mathscr{D}_y|, |\mathscr{D}_z|)}{|\mathscr{R}|} g, \text{ where } |\mathscr{X}| \equiv \max_{x \in \mathscr{X}} x - \min_{x \in \mathscr{X}} x,$$

which works by first scaling the range to the size of the domain along the dimension with the greatest size. I set $g = 10$ to scale the sphere in the range dimension to one tenth the spatial size.

Regardless of what value of κ is chosen, it is likely that photons will not be equally distributed in both space and the range of h. A simple fix suggested by Cammarano and Jensen is to clip the sphere against the minimum and maximum values of h for the photons in the volume. The volume of this clipped sphere can be calculated using Equation 4.10. For reference, see Figure 4.5.

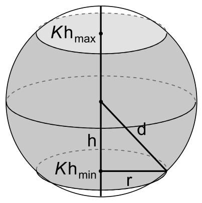

Figure 4.5: Labelling of components of a clipped sphere. d is the radius of the sphere, where $d = \sqrt{\Delta x^2 + \Delta y^2 + \Delta z^2 + (\kappa \Delta h)^2}$. At height h, the radius of the lateral disc is $r = \sqrt{d^2 - h^2}$. The volume of the sphere clipped at $h = \kappa h_{min}$ and $h = \kappa h_{max}$ is $\Delta V = \pi(d^2 \kappa h_{max} - \frac{(\kappa h_{max})^3}{3}) - \pi(d^2 \kappa h_{min} - \frac{(\kappa h_{min})^3}{3})$. This volume is used in the flattened 4D photon mapping radiance estimate in Equation 4.8.

$$
\begin{aligned}
\Delta V &= \int_{\kappa h_{\text{min}}}^{\kappa h_{\text{max}}} \pi r^2 \, \mathrm{d}h \\
&= \int_{\kappa h_{\text{min}}}^{\kappa h_{\text{max}}} \pi (d_{\text{max}}^2 - h^2) \, \mathrm{d}h \\
&= \pi (d_{\text{max}}^2 h - \frac{h^3}{3}) \Big|_{\kappa h_{\text{min}}}^{\kappa h_{\text{max}}} \\
&= \pi (d_{\text{max}}^2 \kappa h_{\text{max}} - \frac{(\kappa h_{\text{max}})^3}{3}) - \pi (d_{\text{max}}^2 \kappa h_{\text{min}} - \frac{(\kappa h_{\text{min}})^3}{3}) \qquad (4.10)
\end{aligned}
$$

For the best results, Equation 4.10 should be used in conjunction with Equation 4.8 to compute the 4D photon map based radiance estimate.

4.3.6 Other issues

The previous sections describe several alterations needed in order to use Photon Mapping to compute 4D flattened radiance. Computing the radiance of a point on the graph proceeds as in ordinary photon mapping: photons are shot into the 4D scene and graph, and scatter while remaining in their respective leaves. This is done using a 4D intersection test with a bounding interval octree and a 4D kd-tree for storing the photons. Solving the 4D flattened light transport equation is performed exactly as in ordinary photon mapping, described in Section 1, provided the 4D intersection test is used and a 4D photon map based radiance estimate is substituted for the ordinary 3D radiance estimate.

An important optimization when rendering static scenes with photon-mapping is the re-use of indirect illumination calculations using irradiance caching [46]. It may be possible to adapt irradiance caching to the computation of 4D flattened light transport, but this optimization was not used for the results in this thesis.

If a faster global illumination solution is desired, one alternative is to compute the direct lighting directly, by ray tracing shadow rays, but computing the indirect illumination by using the photon map radiance estimate directly, as proposed in Section 8.2.1 of Jensen [6]. This is performed by doing a radiance estimate using only those photons that do not come directly from a light source. Using this approach, a useful optimization is to only store indirect photons in the photon map, since that is all that is needed, thus streamlining the radiance estimate. Another important optimization with this technique is to only store photons that lie on isosurfaces and not those that lie on the surrounding scene. This is possible since no gather rays are used, and consequently no radiance estimates will be performed on anything other than isosurfaces of the volume. This memory optimization is important because a lot more photons can (and should) be used in order to have a high-quality radiance estimate.

4.4 Texture generation

The 3D texture is constructed in a similar fashion as explained in Section 3.4. The main idea is to store the illumination of the graph of a heightfield volume in a 3D texture. This idea bears resemblance to the technique used to store illumination values in vicinity shading [13]. However, in vicinity shading, only a single floating point number is stored per-voxel, representing the fraction of incident direct light unoccluded by neighboring geometry. In heightfield rendering, each voxel of the 3D texture stores a full solution to the rendering equation (Equation 1.1). Specifically, each voxel has a red, green, and blue component comprising a spectral exitant radiance value. The voxel's color value includes emitted, direct reflected, and indirect reflected light. This idea of storing a full solution of the rendering equation for the graph of a heightfield volume in a 3D texture is a novel contribution of this thesis.

The radiance is sampled at points $(\vec{x}, h(\vec{x}))$ on the graph of h and filtered into a 3D texture using Shepard's method. The filter kernel function used to determine the weight of a sample for a given texel t_{ijk} depends only on the 3D distance from $\vec{x}$ to the position of the texel, $\vec{t}_{ijk}$:

$$w_{ijk}(L^{\flat}(\vec{x}, h(\vec{x}))) = \left|\vec{x} - \vec{t}_{ijk}\right|^{-5} .$$

The final texture color is computed by taking the weighted average of nearby radiance samples

S, and computing

$$C_{ijk} = \frac{\sum\limits_{S} L^{\flat} w_{ijk}}{\sum\limits_{S} w_{ijk}} ,$$

where C_{ijk} is the color of the texel at texture texel coordinates i, j, and k.

This procedure is implemented by adding the radiance from each radiance sample to nearby texture texels as the samples are taken, by considering those texels in the texture whose coordinates differ from the coordinates of the nearest texel by no more than D, a small integer value (usually 3 or 4). If a sample is desired to have a long-distance influence, then a higher value of D is needed, which results in a longer computation time in order to add the sample to the $(2D+1)^3$ neighboring texels.

4.5 Sampling techniques

For comparison, three sampling approaches are considered, just as in Section 3.4.1.

Uniform sampling Sample points (x_i, y_i, z_i) are chosen randomly using a uniform distribution within the domain. This is achieved by picking three uniform, independent, identically distributed numbers $\varepsilon_1, \varepsilon_2, \varepsilon_3 \in [0,1]$ and choosing $(\varepsilon_1 X, \varepsilon_2 Y, \varepsilon_3 Z)$ as the sample point, where $X \times Y \times Z$ is the domain of h.

Non-uniform sampling Sample points (x_i, y_i, z_i) are chosen in an ill-conceived, plainly bad fashion. In this particular case, samples are placed on a small, discrete set of diagonal planes. This sampling strategy is presented just for illustrative purposes to show the consequence of poorly choosing sample locations.

Level-set sampling Isovalues are chosen and samples are distributed across level sets of the chosen isovalues. This sampling technique is presented to illustrate problems with the idea of explicitly constructing level sets and then subsequently illuminating them. Not only must level sets be constructed for many isovalues, but the isovalues must be chosen so that the isosurfaces through them adequately fill the domain $\mathscr{D}$ of h.

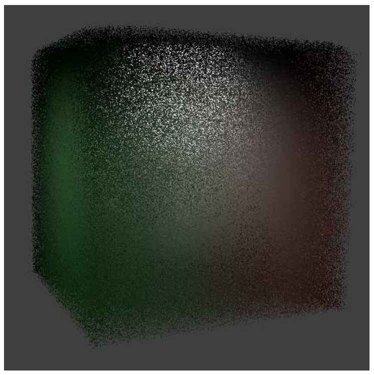
(a) Samples (Uniform)

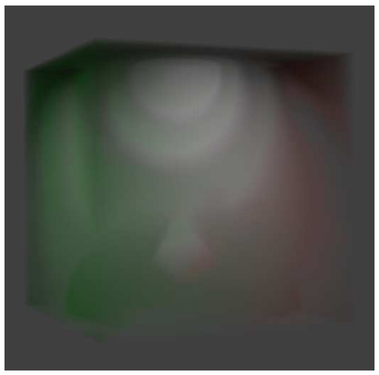
(b) 3D Texture

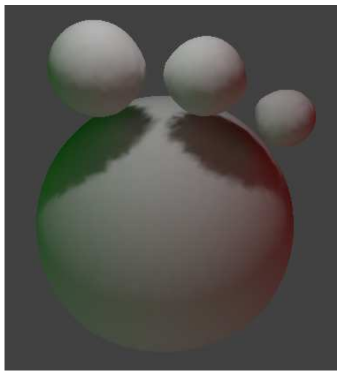
(c) Isosurface

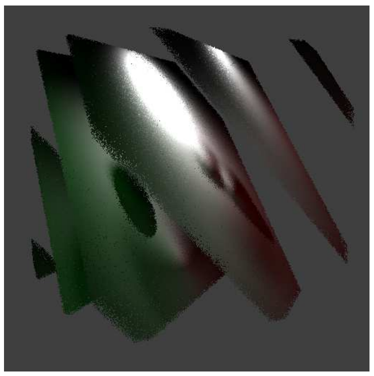
(d) Samples (Non-uniform)

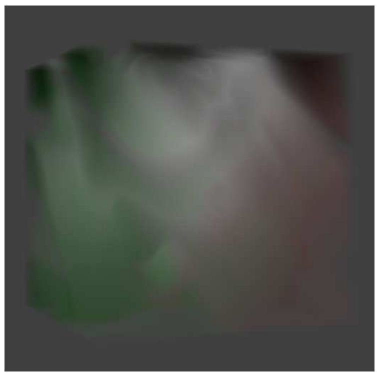
(e) 3D Texture

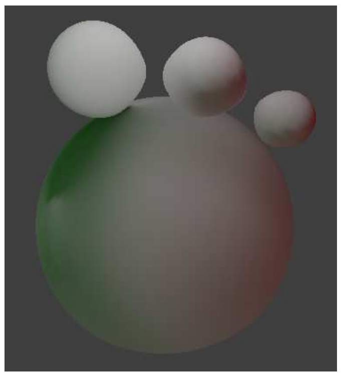
(f) Isosurface

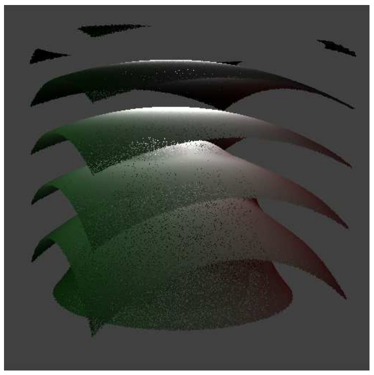
(g) Samples (Level-set sampling)

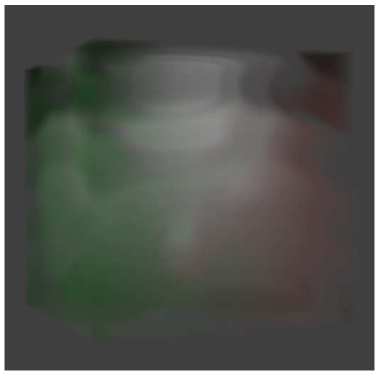
(h) 3D Texture

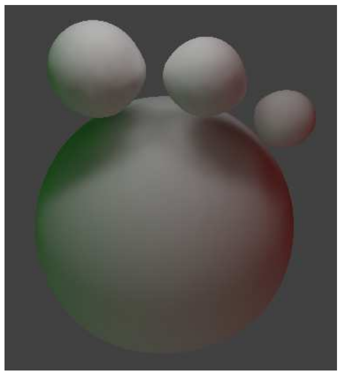
(i) Isosurface

Figure 4.6: Top row: (Left) 10^6 uniformly distributed samples of $L^\flat$ on the graph of h. (Middle) Resulting texture. (Right) Textured isosurface for $h = 47$. Middle row: (Left) 10^6 samples, distributed among small set of diagonal planes. (Middle) Resulting texture. (Right) Textured isosurface. Bottom row: (Left) 10^6 samples, distributed across a small set of isovalues. (Middle) Resulting texture. (Right) Textured isosurface.

4.6 Results

Interactively generating and displaying isosurfaces with global illumination can be achieved by performing heightfield rendering. First, the graph of a heightfield $h : \mathbb{R}^3 \to \mathbb{R}$ is sampled and the 4D flattened light transport equation 4.2 is solved at the sample positions. Next, these radiance samples are interpolated into a 3D texture. Finally, during display, polygonal mesh approximations of isosurfaces are generated at runtime for isovalues determined by the user, and the 3D texture is applied to these surfaces.

To demonstrate heightfield rendering the three sampling techniques described in Section 4.5 were used to sample the 4D flattened radiance of the volume heightfield in the 3D bump box test scene. For each sampling approach, 10^6 radiance samples were computed and interpolated into a 3D texture with 100^3 texel resolution.

Figure 4.6 shows the result of these sampling techniques. The top row illustrates the different stages of heightfield rendering for uniform sampling, the second row shows the stages for non-uniform sampling, and the third row shows the stages for undersampling. In each row, the left column shows the distribution of the samples and their resulting color, computed using 4D flattened photon mapping. The middle column shows the result of interpolating the radiance samples into a 3D texture, and finally the right column shows the result of extracting an isosurface for isovalue $h = 47$ and applying the texture to it.

Figure 4.7 shows a reference isosurface rendered with ordinary photon mapping alongside the three texture-mapped isosurfaces from Figure 4.6. By inspection it is immediately apparent that the uniform sampling approach much more closely matches the appearance of the directly rendered isosurface than the other two sampling techniques. In fact, it matches quite closely.

To confirm this qualitative assessment, a quantitative comparison was made by calculating the Root Mean Square (RMS) error of the three isosurfaces' colors versus the reference, directly rendered, isosurface. For a single vertex, the squared error between the reference surface and the textured surface was calculated using:

$$\text{Squared vertex error} = \frac{(r_1 - r_2)^2 + (g_1 - g_2)^2 + (b_1 - b_2)^2}{3},$$

where (r_1, g_1, b_1) are the RGB colors for a single vertex in the surface to be compared, and (r_2, g_2, b_2) are the RGB colors for a single vertex in the reference surface. The square root of the mean of the squared error for all vertices was computed, and then this value was divided by the

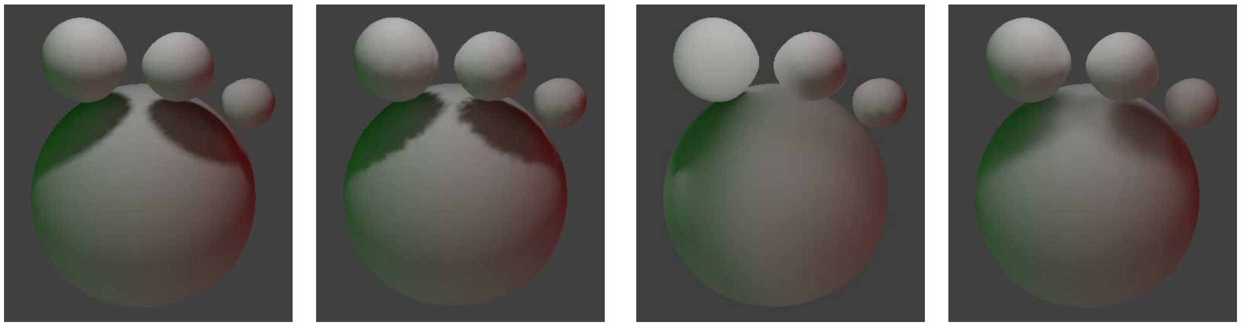

(a) Reference (b) Uniform (c) Non-uniform (d) Level set

Figure 4.7: Isosurface for isovalue 47 from 3D “bump box” data set. (a) Reference isosurface rendered with Pane using normal 3D light transport (b) Isosurface from texture sampled with 10^6 uniformly distributed samples (c) Isosurface from texture sampled with 10^6 samples distributed on angular slabs at regular intervals in the domain of the graph of h (d) Isosurface from texture sampled with 10^6 samples distributed across a small set of isovalues

maximum color possible error (1.0), and then finally divided by 100 to convert to a percentage of possible error. That is,

$$\text{RMS error \%} = \frac{\sqrt{\langle\text{Squared vertex error}\rangle}}{100}\,. \tag{4.11}$$

The percent error for the three sampling techniques used in heightfield rendering is shown in Table 4.2. This results-based comparison of texture sampling techniques is a novel contribution of this thesis. The table confirms the better performance of uniform sampling versus the other two sampling techniques. Furthermore, using uniform sampling, the result of heightfield rendering is 98.7% the same as directly rendering the isosurface, on average. Table 4.2 also shows the result of using 10 times as many samples, showing a slight improvement for each strategy. The sampling strategy with the lowest RMS error percentage, uniform sampling, still produces some artifacts seen as blotches, evident in Figure 4.7(b). These blotches are the result of undersampling the underlying graph and gradually improve as more samples are taken.

Precomputing the texture using uniform sampling of the domain and 4D flattened photon mapping required 52 minutes on a Dual Pentium 4 Xeon PC with 4 GB of RAM. Extracting the isosurface required 0.256 seconds during interactive viewing using an custom marching cubes implementation, and applying the 3D texture to the isosurface required an additional 0.055 seconds. Contrast this with rendering the isosurface using ordinary photon mapping, which required 5.2

Table 4.2: Average RMS percent error for the vertices of an isosurface rendered with heightfield rendering, for three sampling strategies used to create the texture. Errors are computed using Equation 4.11 in relation to a reference isosurface that was directly rendered with photon mapping. Table shows the errors for taking 10^6 and 10^7 samples using the three strategies.

Samples	10^6	10^7
Sampling strategy	RMS Error (%)	
Uniform	1.29	1.08
Non-uniform	9.55	9.57
Level-set	3.59	3.47

minutes: the former is able to be performed at interactive speeds while the latter is not.

Non-uniform sampling and level-set sampling both perform relatively poorly compared to uniform sampling because they leave large portions of the domain (and hence, the 3D texture) unsampled. These values are then filled in using interpolation, and consequently have higher error. In particular, the samples for level-set sampling were distributed across level sets having the following nine, adaptively-chosen [33] isovalues: 0.01, 6.4744, 13.17, 19.3451, 24.8489, 29.5883, 39.0118, 56.6704, and 160.873. The isovalue $h = 47$ chosen for the textured isosurface falls halfway between two of the sampled isovalues for undersampling. This choice of isovalue is the likely cause for the higher amount of error, and highlights a pitfall of distributing samples along level sets of a small set of sampled isovalues.

4.7 Uniform sampling optimizations

Figures 4.8(a) shows samples of the illumination on the graph of an example one-dimensional (1D) heightfield. The illumination samples are filtered into a 1D texture linear in the domain, shown beneath the graph. Purely random, uniform sampling in the domain of the graph can leave relatively large gaps in the domain where there are no samples. For example, the texel for the large, front facing bump, highlighted in red, does not receive a sample. This is a bad situation since the hill segment spans a great percentage of the total height and is thus visible in a large proportion of level sets (points, for a 1D heightfield). Regularly spacing the samples, or using stratified (jittered) samples [20], as shown in Figure 4.8(b), yields lower discrepancy in the samples and guarantees the aforementioned texel (highlighted) will have at least one sample. This improves the situation, however, since the lighting is varied on the hill, meaning the top majority is

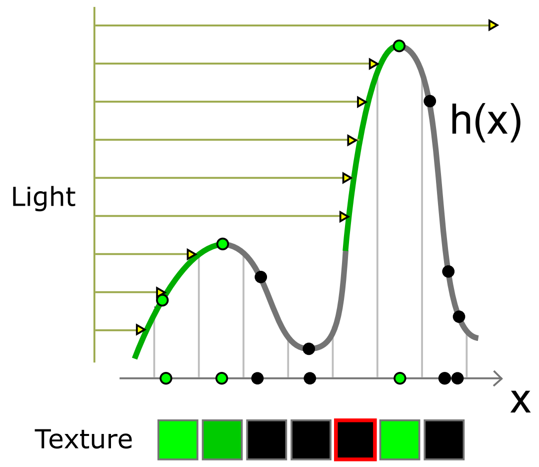

(a) Uniform

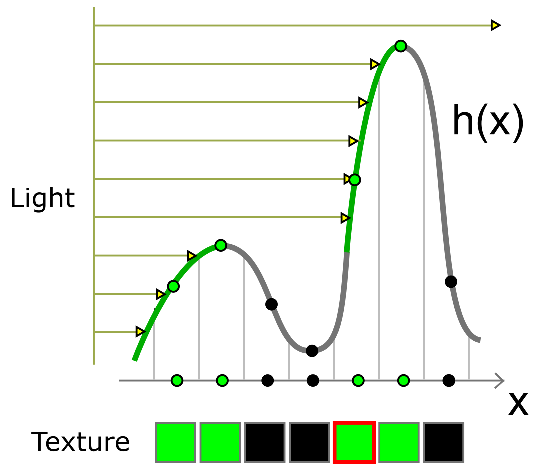

(b) Regular

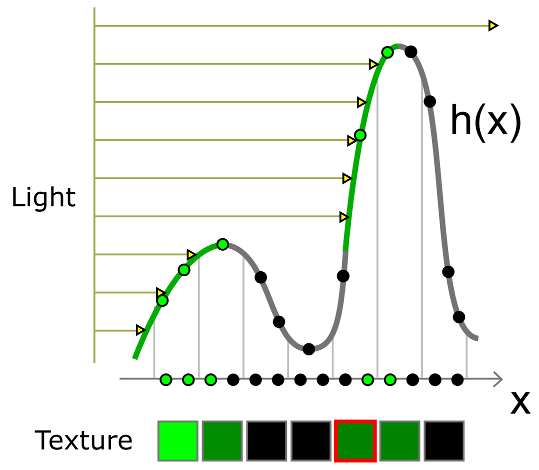

(c) 2*x* Regular

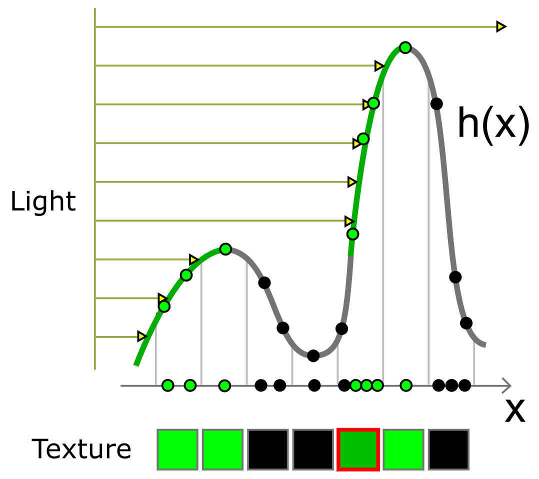

(d) 2*x* Importance

Figure 4.8: Samples of the illumination on the graph of an example one-dimensional (1D) heightfield. The illumination samples are filtered into a 1D texture linear in the domain. (a) Uniform sampling in the domain of the graph can leave relatively large gaps in the domain. For example, the texel for the large, front facing bump, highlighted in red, does not receive a sample. This is a bad situation since the hill is exists at many heights and is visible in a large proportion of level sets. (b) Regularly spacing the samples or using stratified (jittered) samples gives lower discrepancy, guaranteeing the aforementioned texel at least one sample. (c) Taking twice as many regular samples improves the texture quality, giving each texel two samples. However, the large bump is still under sampled. (d) One approach is to supersample these areas more than less important areas, thus saving samples. This is achieved by performing more supersampling in regions that span a greater total extent in the range. Here the large forward facing bump receives four samples while other regions receive only one sample, using the same number of samples as in (c).

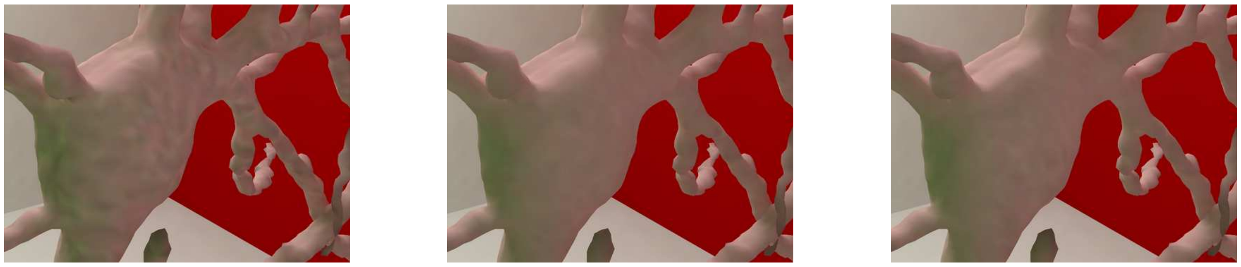
(a) $4 \cdot 10^6$ stratified samples (b) $64 \cdot 10^6$ stratified samples (c) $2 \cdot 10^6$ importance samples

Figure 4.9: Focusing samples in regions that span a large extent of the range of the function can greatly improve texture quality. (a) Result of 4 million stratified, uniformly distributed illumination samples on the neuron dataset. (b) Taking 64 million stratified, uniformly distributed illumination samples eliminates the noise. (c) Taking just 2 million importance samples using Equation 4.12 performs as well as well as taking 32 times as many samples (b).

illuminated while the bottom minority is in shadow, a single sample does not accurately represent the average lighting of the segment of the graph. In this example, any level sets in this region will receive the same lit color which is incorrect for level sets in the region that are in shadow. Taking twice as many samples, as in Figure 4.8(c), improves the texture quality, giving each texel two samples. Now all level sets that receive color from this texel will be shaded as being halfway lit and shadowed, an improvement. However, the large bump is still under sampled, since the correct average illumination is approximately 75% rather than the estimated value of 50%.

One answer to this problem is to just take more samples. However, some regions with slowly varying lighting will then receive too many samples, a computational waste. A better approach is to supersample [47] the areas that need it more than the areas that do not. This is achieved by performing more supersampling in regions that span a large total extent in the range, as shown in Figure 4.8(d). Here the large forward facing bump receives four samples while other regions receive only one sample, using the same number of samples as in Figure 4.8(c). This approach of focusing samples in important areas is a form of importance sampling [20]. A 3D texture sampled with importance sampling is sometimes equivalent in quality to one created with over thirty times as many stratified uniformly distributed samples. Figure 4.9 shows one such example.

To perform importance sampling, the data cells of the dataset are iterated over, taking n_{ijk}

samples in each data cell (i, j, k):

$$n_{ijk} = \lceil \text{fractionalExtentOfCell}(i, j, k) * \text{maxSamplesPerCell} \rceil \ , \tag{4.12}$$

where fractionalExtentOfCell is defined in Equation 4.14 and is the ratio of the cell's extent of h to the total extent of h, and maxSamplesPerCell is the maximum desired supersampling rate for a single data cell. Equation 4.12 yields a sample size $n_{ijk} \in [1, \text{maxSamplesPerCell}]$ for cells with a non-zero extent, and zero samples for cells with zero extent. Cells with zero extent have zero level sets through them so there is no need to take a single sample of them. Skipping them saves time and does not cause a noticeable effect. The fractional extent is computed by taking the difference of the maximum and minimum values of h for the eight voxel corners of the data cell, and dividing by the global maximum difference in h. The result takes on values in $[0, 1]$:

$$\begin{aligned} \text{fractionalExtentOfCell}(i, j, k) = &(\max(h(i+a, j+b, k+c) \ \forall \ a, b, c \in \{0, 1\}) - \qquad (4.13) \\ &\frac{\min(h(i+a, j+b, k+c) \ \forall \ a, b, c \in \{0, 1\}))}{h_{max} - h_{min}} \ . \qquad (4.14) \end{aligned}$$

This optimized sampling technique is a novel contribution of this thesis.

CHAPTER 5

RESULTS ON SCIENTIFIC DATA

5.1 Images

This chapter shows the result of applying heightfield rendering to four scientific datasets from medicine, astrophysics, neuroscience, and nanochemistry. Applying heightfield rendering to these datasets is a novel contribution of this thesis.

For these scenes a modified Cornell box with colored walls was placed around the data to simulate an environment and provide direct light from an overhead luminaire and indirect light from surrounding walls. During interaction with the level sets, a rendered version of this scene geometry is displayed in the background to provide context for the lighting.

The first dataset is a density convolution of the exotic atomic structures in the crust of a neutron star. This dataset is from Dr. Jorge Piekarewicz in the Department of Physics at FSU and Brad Futch in SCS at FSU. The nucleons dataset consists of two density convolutions of particle data, each of $101 \times 101 \times 101$ resolution. Rendering them simultaneously requires generating two textures, one for each particle convolution, and extracting and texturing an isosurface from each convolution. Figure 5.1(a) shows two such extracted isosurfaces, rendered with local illumination using OpenGL, requiring 1.40 seconds to create. Figure 5.1(b) shows the same isosurface rendered with global illumination using heightfield rendering, taking 1.46 seconds. The textures were precomputed using 4D flattened photon mapping with 4 million stratified uniformly distributed samples throughout each volume. Precomputing the radiance values and interpolating them into a 3D texture required 9685 seconds. For each texture, direct lighting was calculated using ray tracing while indirect lighting was calculated directly from the photon map, which contained roughly 15 million photons. Figure 5.2 shows another view.

Figure 5.4 shows level sets for four isovalues of the dataset illuminated using heightfield rendering. Extracting and texturing the level sets for each isovalue required an average of 0.885

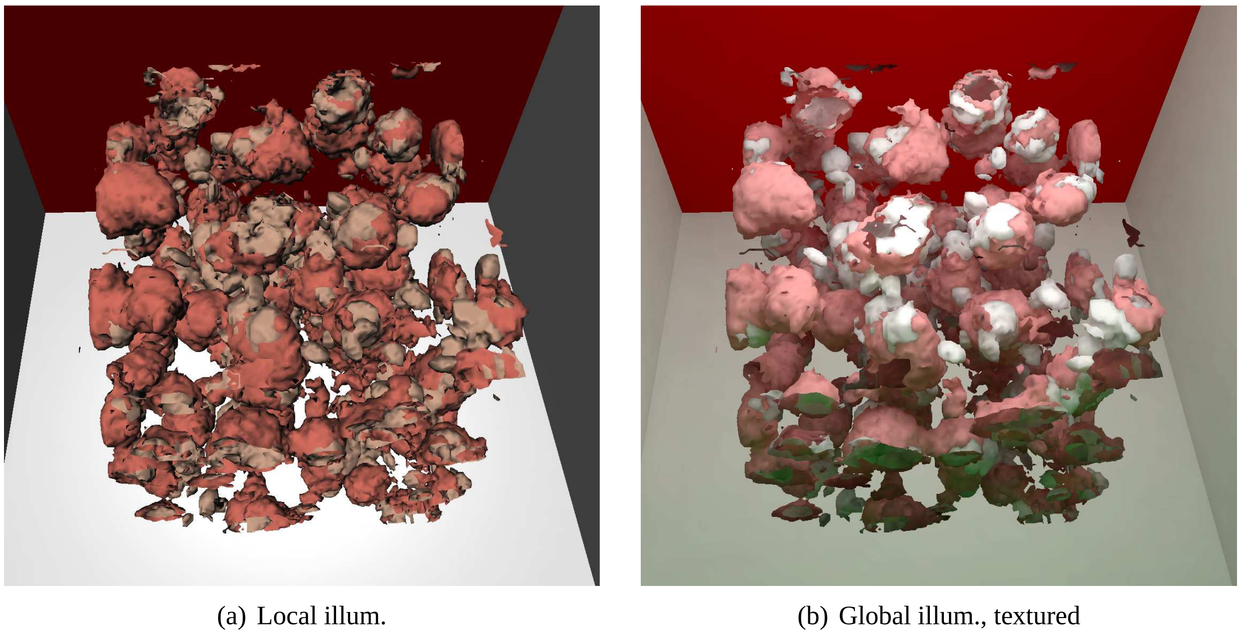
(a) Local illum. (b) Global illum., textured

Figure 5.1: (a) Level set of the nucleons dataset for $h = 39$, top angle view, rendered using local illumination (OpenGL), requiring 1400 milliseconds to extract and display. (b) The same level set rendered using heightfield rendering with global illumination, requiring 1460 milliseconds to extract and display. The precomputation time for the heightfield rendering 3D texture was 9685 seconds.

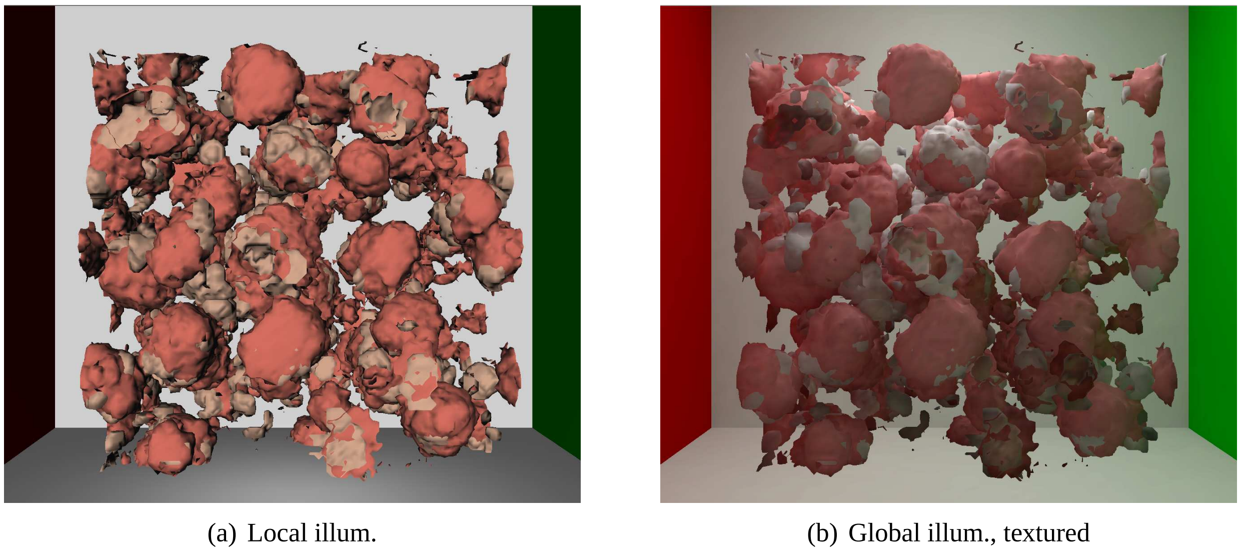
(a) Local illum. (b) Global illum., textured

Figure 5.2: (a) Front view of level set of nucleons dataset for $h = 39$, rendered with local illumination. (b) Level set rendered with heightfield rendering.

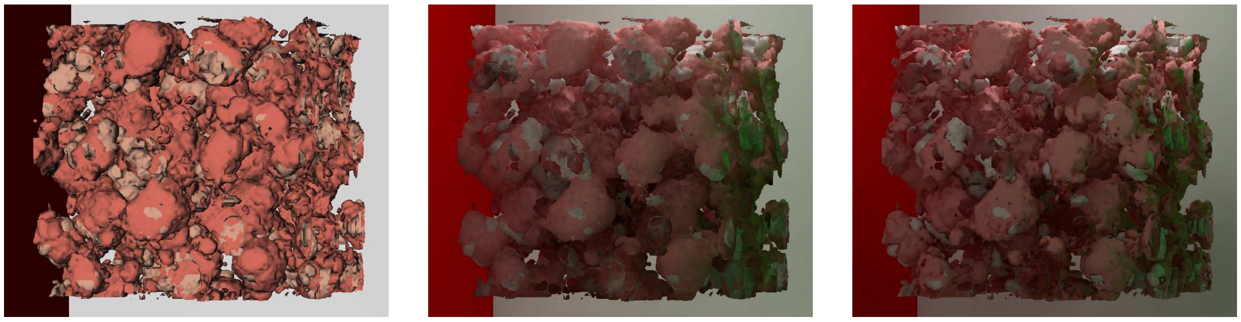

(a) Local illum. (b) Global illum., textured (c) Global illum., rendered

Figure 5.3: (a) Level set for $h = 24$ from the nucleon level set, rendered using local illumination (OpenGL), requiring XXX milliseconds to extract and display. (b) Level set for $h = 24$ rendered using heightfield rendering. (c) Level set for $h = 24$ rendered directly using ordinary photon mapping, requiring 2155 seconds to render. Notice that the heightfield-rendered and directly-rendered images are nearly identical. The average RMS error for the vertex colors between the heightfield-rendered level set and the directly-rendered version is 5.61%.

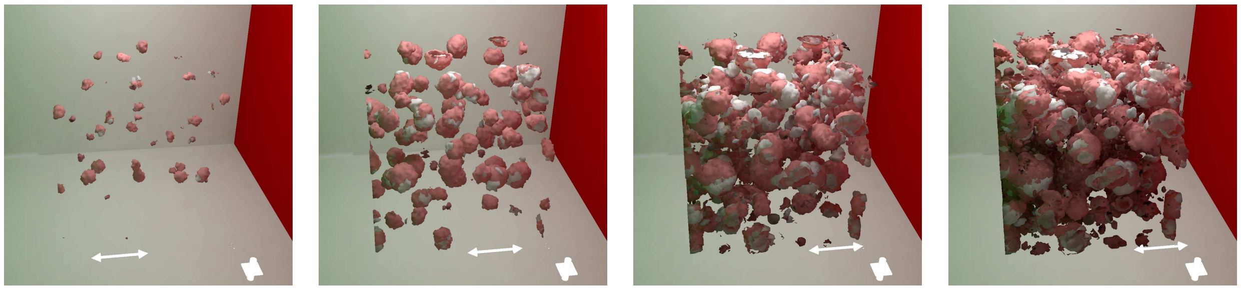

(a) $h = 170$ (b) $h = 79$ (c) $h = 39$ (d) $h = 24$

Figure 5.4: Level sets of the nucleon dataset for different isovalues: $h = 170$, $h = 79$, $h = 39$, and $h = 24$. Images were rendered using global illumination via heightfield rendering, requiring 3.473 seconds per level set (average) for extraction and displaying.

seconds. After extraction, the level sets could be rotated, moved, and zoomed at approximately 60 Hz by utilizing OpenGL and the hardware acceleration of the video card.

Figure 5.3 shows a comparison of local illumination, heightfield rendering with global illumination, and reference isosurface that was extracted and rendered directly with global illumination. The heightfield rendering image looks the same as the reference image but rendered as fast as the local illumination image, taking less than one second, while the reference image took 2155 seconds. There is a small error in the heightfield rendered image of 5.61%, although this error is

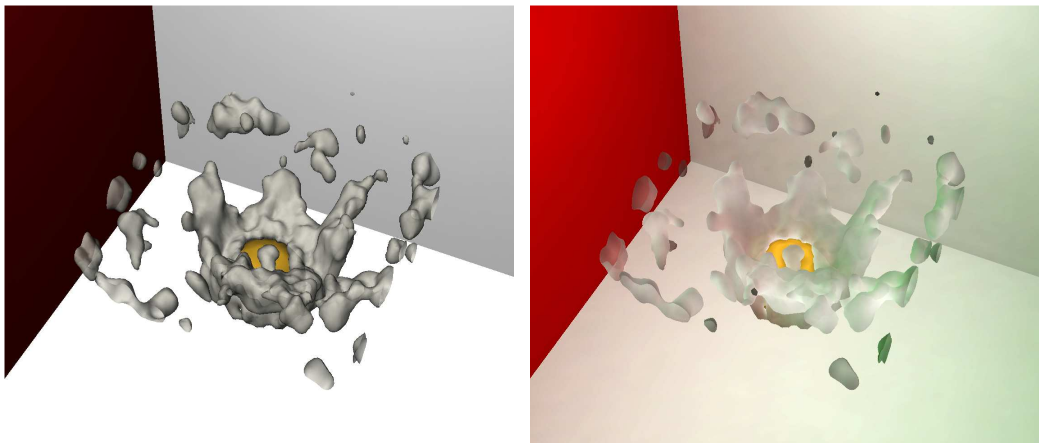
(a) Local illum. (b) Global illum., textured

Figure 5.5: (a) Level set of LAPR dataset for $h = 112$ rendered with local illumination, requiring 0.880 seconds to extract and display. (b) Same level set rendered with global illumination via heightfield rendering, requiring 0.920 seconds to extract and display. Heightfield rendering required 5565 seconds to precompute the illumination into a texture.

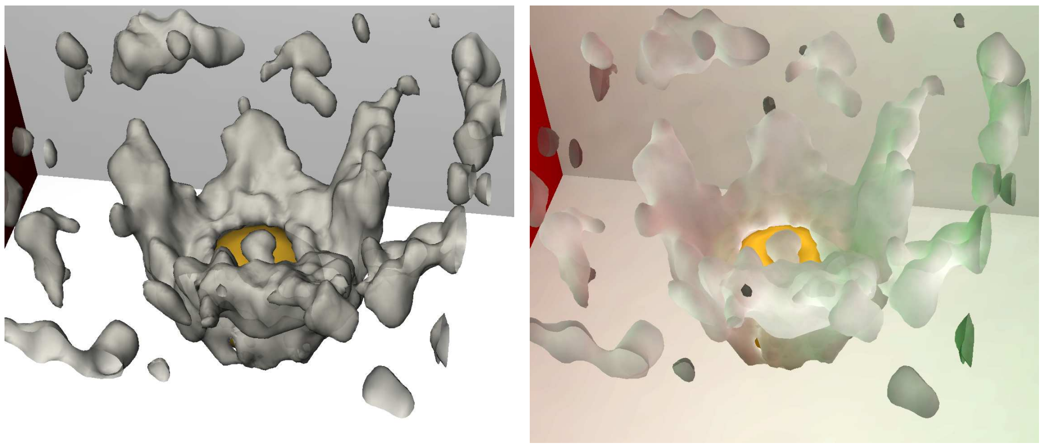
(a) Local illum. (b) Global illum.

Figure 5.6: (a) Level set of LAPR dataset for $h = 112$ rendered with local illumination. (b) Same level set rendered with global illumination via heightfield rendering.

mostly unnoticeable. There are two sources of error: 1) the rendering approximation of estimating indirect illumination directly from the photon map without a final gather, and 2) interpolating the radiance onto a texture and then texture-mapping the radiance onto the level set.

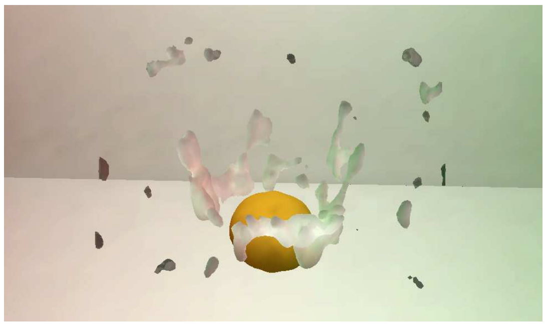

(a) $h = 201$

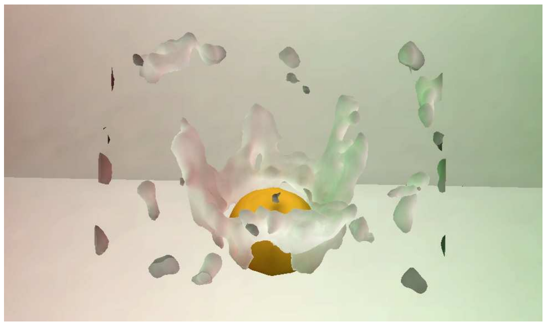

(b) $h = 166$

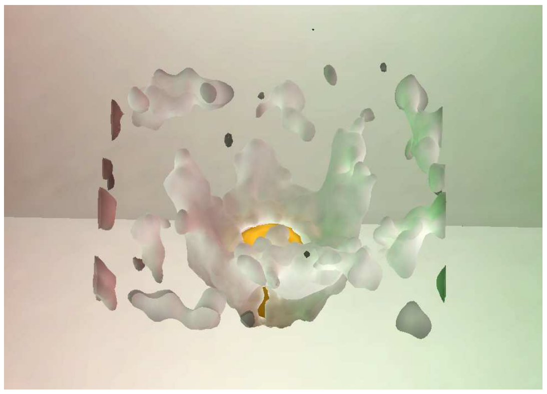

(c) $h = 116$

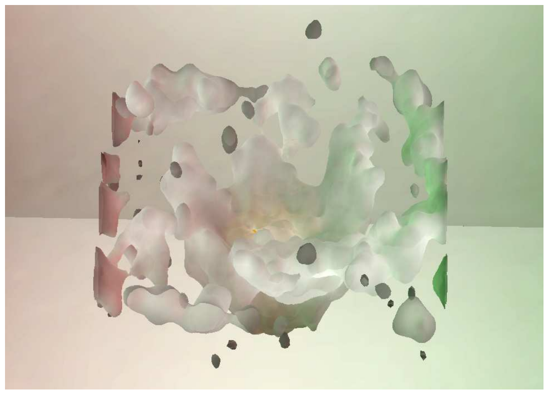

(d) $h = 76$

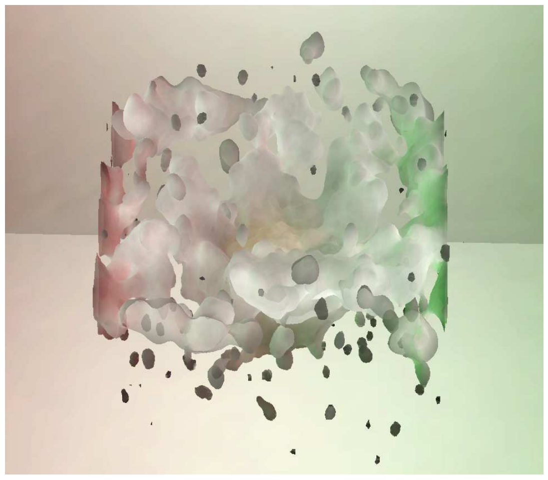

(e) $h = 52$

Figure 5.7: Five level sets of the LAPR dataset for isovalues $h = 201$, $h = 166$, $h = 116$, $h = 76$, and $h = 52$. Images were rendered using global illumination via heightfield rendering, and took 1.065 seconds per isovalue (average) for extraction and displaying.

Figures 5.5-5.7 shows density data from a molecular dynamics simulation of Laser Assisted Particle Removal (LAPR), conducted by Dr. M.Y. Hussaini and Dr. Kayne Smith in the School of Computational Science (SCS) at FSU. Like the nucleons dataset, the LAPR dataset is comprised of two convolutions: one for the dirt particle, and one for the explosively evaporating water that is

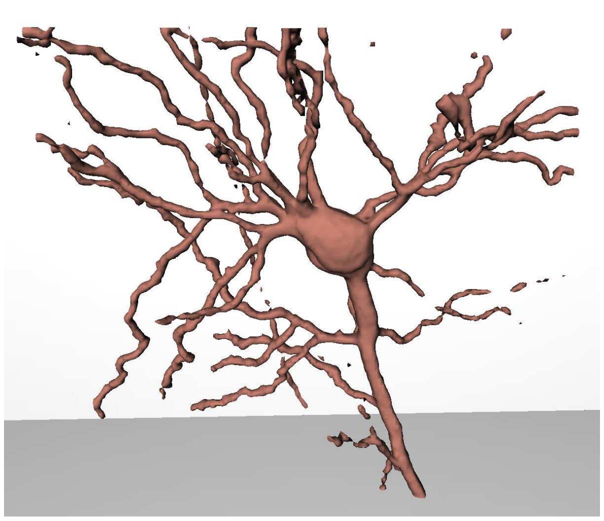
(a) Local illum.

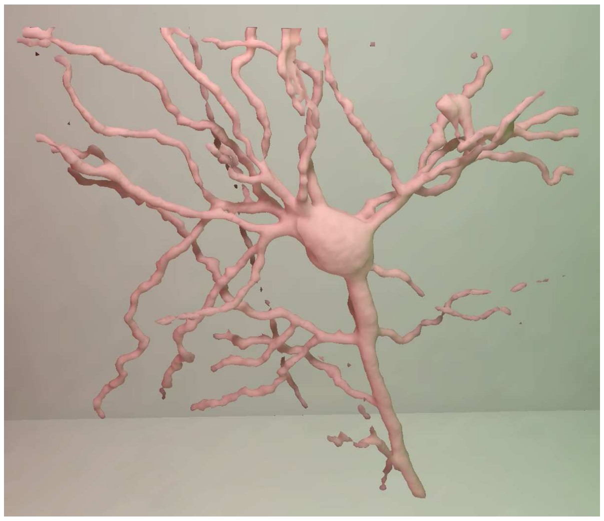
(b) Global illum., textured

Figure 5.8: (a) Level set of the neuron dataset for $h = 150$ rendered with local illumination, requiring 0.870 seconds to extract and display. (b) Same level set rendered with global illumination via heightfield rendering, requiring 0.880 seconds to extract and display. Heightfield rendering required 4587 seconds to precompute the illumination into a texture.

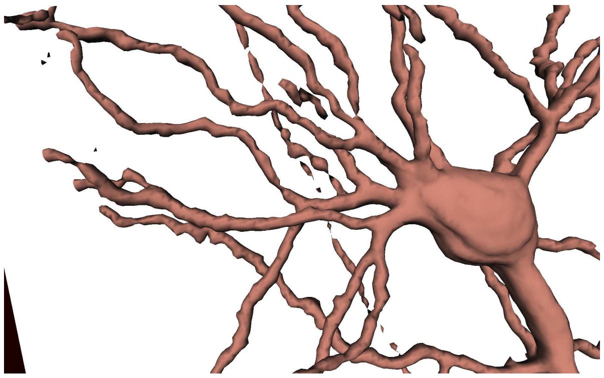
(a) Local illum.

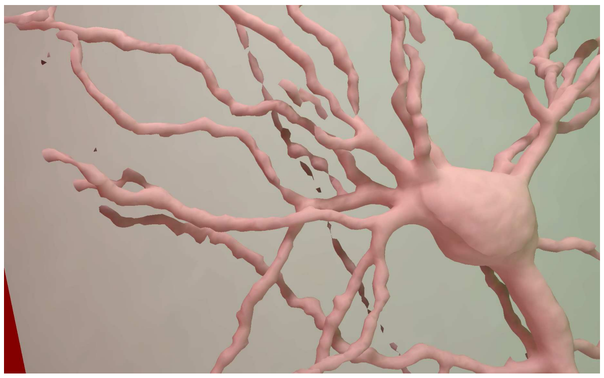
(b) Global illum., textured

Figure 5.9: Front view of level set of neuron dataset for $h = 85$. (a) Rendered with local illumination. (b) Rendered with global illumination via heightfield rendering.

lifting it.

Figures 5.8-5.10 shows a dataset from a confocal microscope scan of a living mouse neuron. This dataset is from Debra Fadool in the Department of Neuroscience at FSU, and Wilfredo Blanco

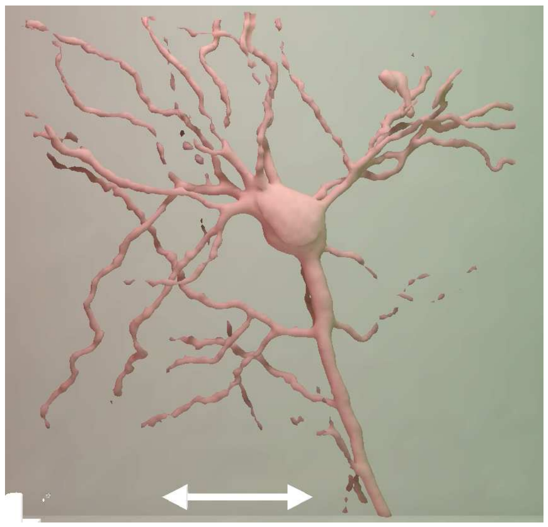

(a) $h = 107$

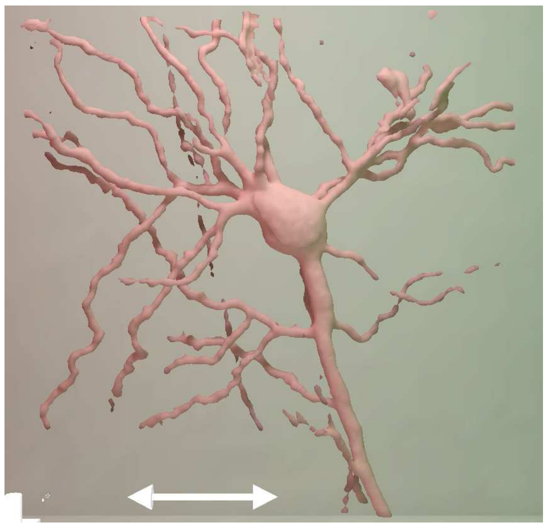

(b) $h = 88$

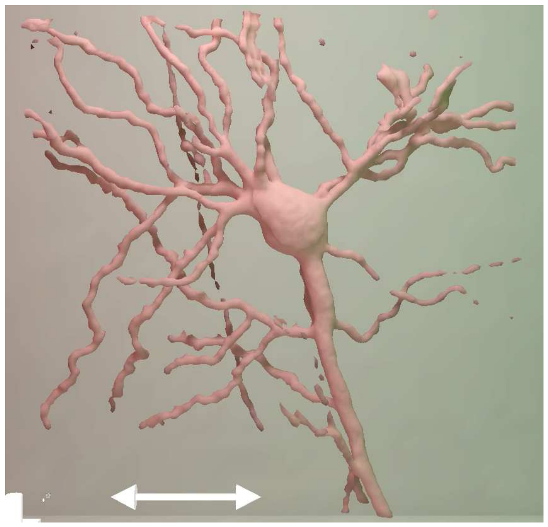

(c) $h = 78$

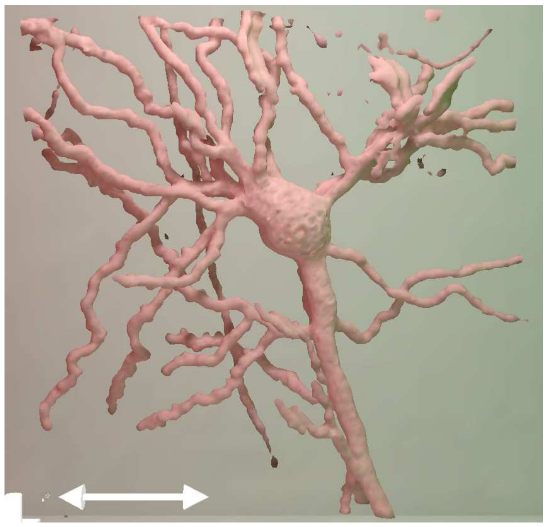

(d) $h = 49$

Figure 5.10: Four level sets of the neuron dataset for isovalues $h = 107$, $h = 88$, $h = 78$, and $h = 49$. Images were rendered with global illumination via heightfield rendering, taking 0.838 seconds per level set (average) for extraction and displaying.

in SCS at FSU.

Figures 5.11-5.13 shows a Magnetic Resonance Imaging (MRI) scan of a human brain, scanned at the McConnell Brain Imaging Center at McGill University.

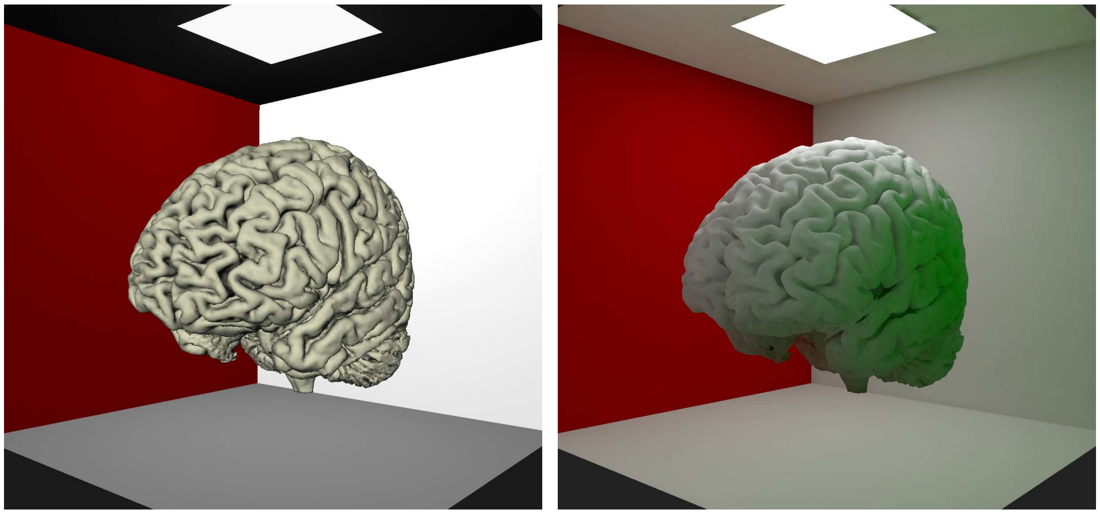

(a) Local illum. (b) Global illum.

Figure 5.11: Level set of the brain dataset for $h = 77$. (a) Rendered with local illumination, requiring 4.450 seconds to extract and display. (b) Same level set rendered with global illumination via heightfield rendering, requiring 4.680 seconds to extract and display. Heightfield rendering required 5452 seconds to precompute the illumination into a texture.

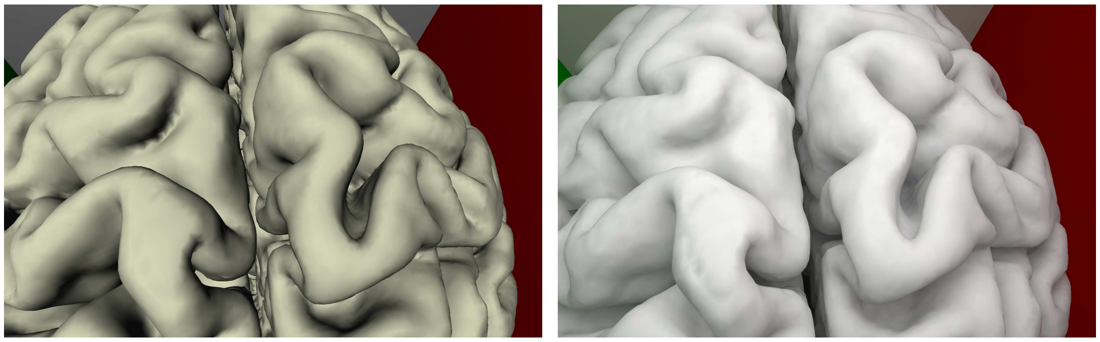

(a) Local illum. (b) Global illum., textured

Figure 5.12: Top view of level set of brain dataset for $h = 77$. (a) Rendered with local illumination. (b) Rendered with global illumination via heightfield rendering.

5.2 Timings

Table 5.14 summarizes these results and provides resolution, rendering settings, accuracy, and timings information for all four datasets. All 3D textures were computed on a dual processor Intel

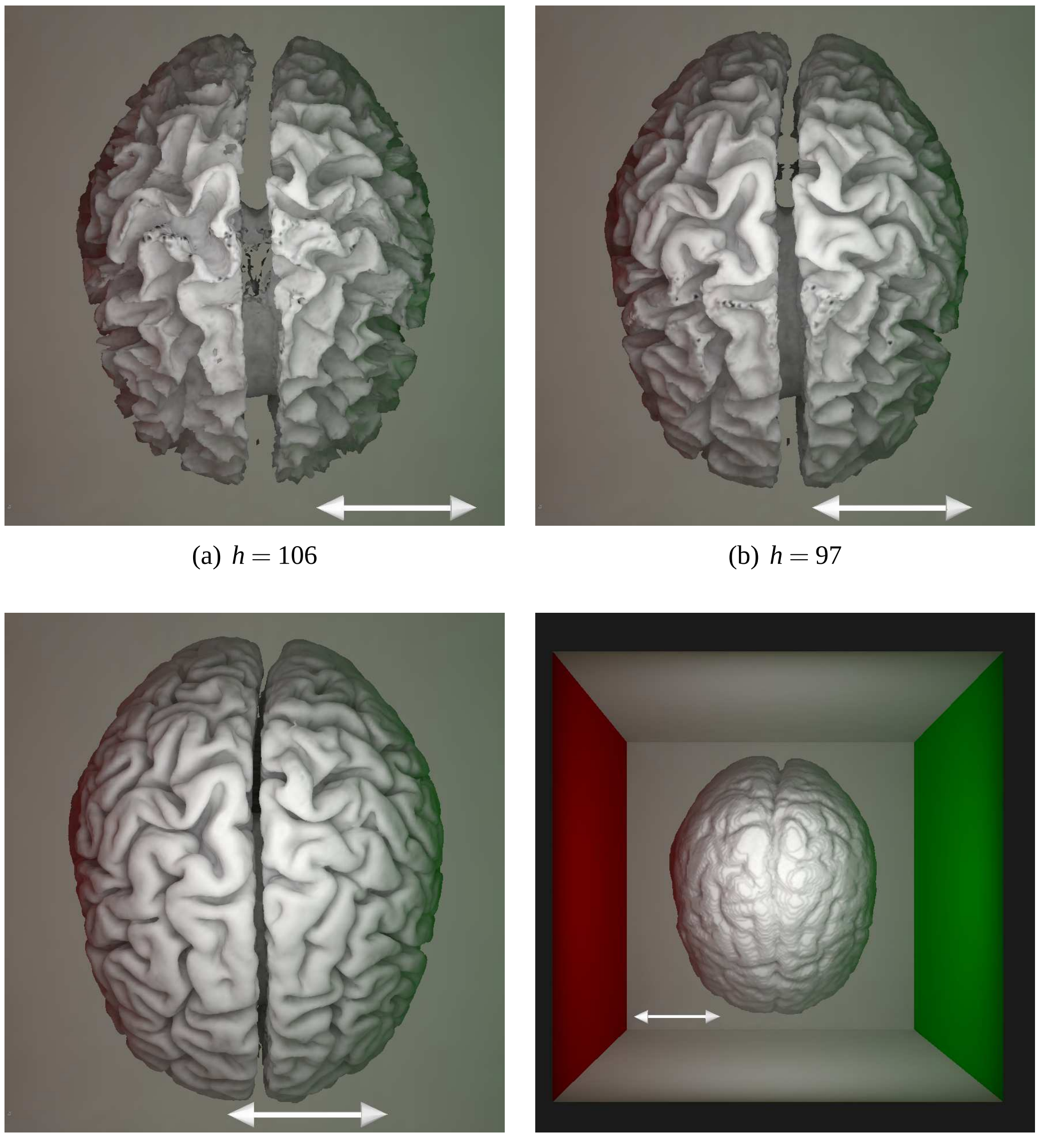

(a) $h = 106$ (b) $h = 97$

(c) $h = 82$ (d) $h = 19$

Figure 5.13: Four level sets of the brain dataset for isovalues $h = 106$, $h = 97$, $h = 82$, and $h = 19$. Images were rendered using global illumination via heightfield rendering, requiring 3.473 seconds per level set (average) for extraction and displaying.

Pentium 4 Xeon 3.0 GHz workstation with 4 GB of RAM running Redhat Linux 9.0, using the GNU g++ compiler.

			Texture			Single Isosurface		
Dataset	Qty. (#)	Reso-lution	Texture Samples	Phots. (10^6)	Precomp. Time (s)	Texturing Time (s)	Render Time (s)	Avg. RMS Error (%)
Nucleon	2	101^3	8,000,000	11.0	9,685	0.050	2,155	5.61%
LAPR	2	120^3	3,755,979	15.2	5,565	0.036	522	8.06%
Neuron	1	150^3	2,075,806	11.7	4,587	0.014	1,229	5.70%
Brain	1	217^3	17,390,102	7.6	5,452	0.098	1,819	6.53%

Figure 5.14: Timings and errors for heightfield rendering of four scientific datasets. Errors are for a single (arbitrary) texture-mapped isosurface versus a reference directly-rendered isosurface, and were computed using Equation 4.11.

5.3 Incorporating into a commercial software

To demonstrate globally illuminated isosurfaces, I used a custom Marching Cubes application to extract the isosurface and texture map it with a precomputed 3D texture. It is also possible to display globally illuminated isosurfaces by using the 3D texture in an commercial visualization package called “amira”, from Template Graphics Systems. amira supports isosurface visualization via Marching Cubes, additionally it supports 3D textures. Therefore it is possible to use amira to perform the last stage of heightfield rendering and display globally illuminated level sets. Doing so is a simple process and represents a novel contribution of this thesis. Figure 5.15 shows an isosurface of the brain dataset rendered with and without global illumination using amira. Figure 5.15 also shows the network used to configure amira to apply the texture map and achieve this result. To perform this operation, the 3D texture must be saved in a file with four bytes per voxel: one each for red, green, blue, and alpha (RGBA), respectively. The red, green, and blue bytes are specified by color of the texture voxel and the alpha byte should be set to 255. The texture is then loaded into amira as “Raw Data”, with a data type of four bytes per voxel (RGBA) and resolution equal to that of the texture. To apply the texture, first the dataset is loaded into amira and right-clicked to “Display” an “isosurface”. The texture is then applied by right-clicking the isosurface module’s connector box, selecting “ColorField”, and selecting the texture module. Any isosurfaces created will then have the 3D texture map applied, and will be displayed with the global illumination stored in the 3D texture. There is one caveat: amira’s headlight will cast additional diffuse shading on the isosurface. However, this may be considered useful for directional shading effects.

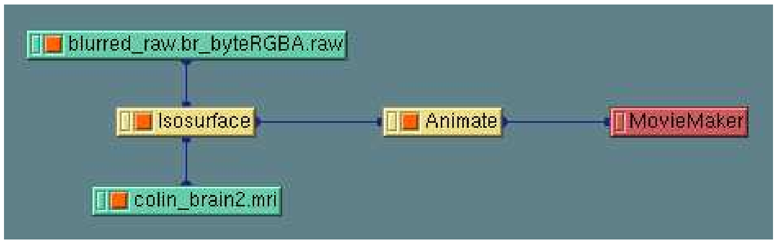

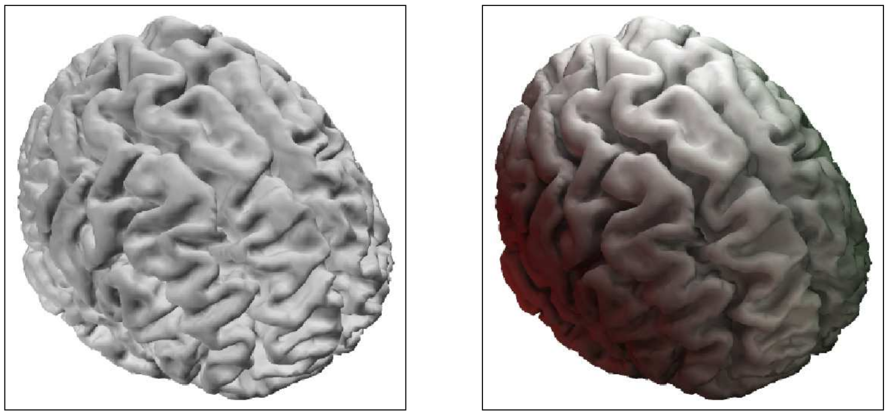

Figure 5.15: Incorporating pre-computed global illumination into the commercial visualization tool “amira.” Top: Data flow network of amira modules. Bottom: (left) Level set displayed with amira’s native lighting model; (right) displayed with 3D global illumination texture.

5.4 Summary

With heightfield rendering, a scientist examining the dataset is free to explore the level sets, including zooming, rotating, moving, and changing the isovalue, while taking advantage of the natural spatial relationship cues that global illumination offers, with no noticeable extra delay.

5.5 Conclusion

By providing a scientist or engineer wishing to examine their 3D scalar heightfield function $h : \mathbb{R}^3 \to \mathbb{R}$ the ability to interact and explore level sets of that data with global illumination, they are better able to interpret the data, especially the spatial relationships between different parts of the level set, thanks to the natural cues to the human visual system imparted by shadows and indirect illumination. Heightfield rendering provides these users with global illumination while still enabling them to explore the data interactively. It achieves this by (1) solving a modified version of the light transport equation and precomputing all global illumination solutions of the heightfield, (2) storing the solution in a 3D texture, and (3) extracting polygonal approximations of level sets and texture-mapping them with the precomputed texture. The result is interactive global illumination of level sets. The benefits have been illustrated with figures and timings, thus proving the thesis, namely, that globally illuminated isosurfaces of a scalar function $h : \mathbb{R}^3 \to \mathbb{R}$ can be generated and displayed at interactive rates on an ordinary desktop computer equipped with a graphics card.

APPENDIX A

Ray Isosurface Intersection for A Trilinear Cell

This appendix describes how to find the intersection of a ray with a cell, and it's normal, from a volumetric scalar heightfield. It is reproduced almost exactly from Parker *et al.* [9] with very minor corrections (sign reversals) in Equations A.1, A.2 A.3, A.4, and Figure A.2. These corrections, forming a correct algorithm, are a novel contribution of this thesis.

Let $h : \mathbb{R}^3 \rightarrow \mathbb{R}$ be a scalar field defined over a volume, at regular points in a 3D grid. For any given cell within the grid (Figure A.1), the function value within the cell can be found using

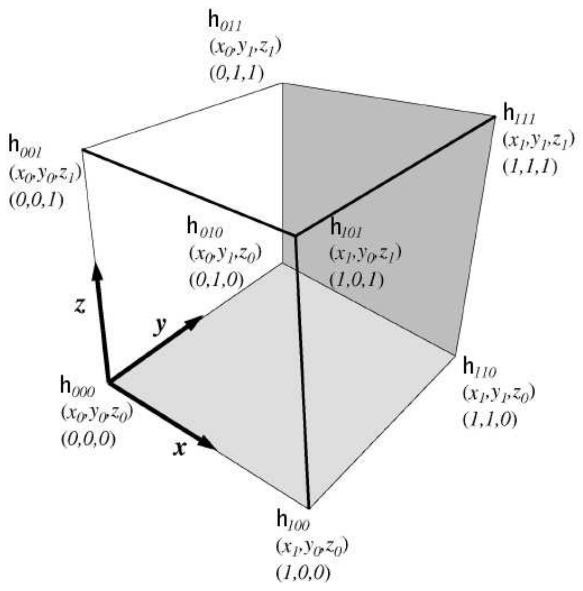

h_{011} (x_0,y_1,z_1) (0,1,1)
h_{111} (x_1,y_1,z_1) (1,1,1)
h_{001} (x_0,y_0,z_1) (0,0,1)
h_{010} (x_0,y_1,z_0) (0,1,0)
h_{101} (x_1,y_0,z_1) (1,0,1)
z
y
h_{110} (x_1,y_1,z_0) (1,1,0)
h_{000} (x_0,y_0,z_0) (0,0,0)
x
h_{100} (x_1,y_0,z_0) (1,0,0)

Figure A.1: Labelling of a cell. The cell's corner are eight neighboring voxels in a rectilinear grid, a small piece of a volume heightfield $h : \mathbb{R}^3 \rightarrow \mathbb{R}$. Figure reproduced from [9] Fig. 15

trilinear interpolation:

$$\begin{aligned}h(u,v,w) = (1-u)(1-v)(1-w)h_{000}+\\ (1-u)(1-v)(w)h_{001}+\\ (1-u)(v)(1-w)h_{010}+\\ (u)(1-v)(1-w)h_{100}+\\ (u)(1-v)(w)h_{101}+\\ (1-u)(v)(w)h_{011}+\\ (u)(v)(1-w)h_{110}+\\ (u)(v)(w)h_{111},\end{aligned}$$

where

$$u = \frac{x-x_0}{x_1-x_0} \qquad v = \frac{y-y_0}{y_1-y_0} \qquad w = \frac{z-z_0}{z_1-z_0},$$

and similarly,

$$1-u = \frac{x_1-x}{x_1-x_0} \qquad 1-v = \frac{y_1-y}{y_1-y_0} \qquad 1-w = \frac{z_1-z}{z_1-z_0}.$$

By defining

$$\begin{aligned} u_0 &= 1-u & u_1 &= u \\ v_0 &= 1-v & v_1 &= v \\ w_0 &= 1-w & w_1 &= w \end{aligned}$$

the following simple equation can be used to find the value of h:

$$h = \sum_{i,j,k=0,1} u_i v_j w_k h_{ijk}.$$

The surface normal inside the cell is given by the gradient:

$$\vec{N} = \vec{\nabla} h = \left(\frac{\partial h}{\partial x}, \frac{\partial h}{\partial y}, \frac{\partial h}{\partial z} \right).$$

Using finite differencing to approximate the differentials, the following summations compute the

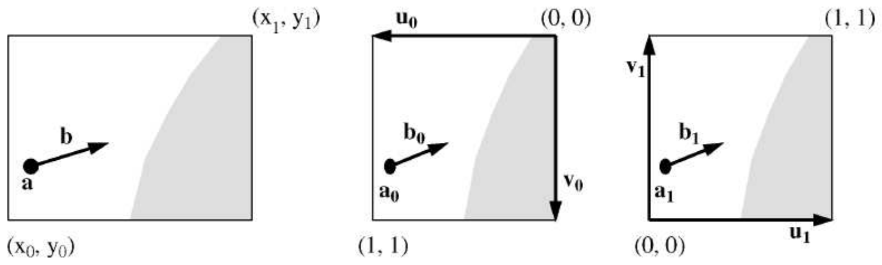

Figure A.2: Coordinate systems use for interpolation and intersection. Figure modified (corrected) version from [9] Fig. 16

normal:

$$N_x = \sum_{i,j,k=0,1} \frac{(-1)^{i+1} v_j w_k}{x_1 - x_0} h_{ijk}$$
$$N_y = \sum_{i,j,k=0,1} \frac{(-1)^{j+1} u_i w_k}{y_1 - y_0} h_{ijk}$$
$$N_z = \sum_{i,j,k=0,1} \frac{(-1)^{k+1} u_i v_j}{z_1 - z_0} h_{ijk}.$$

Given a ray with position $\vec{r} = \vec{a} + t\vec{b}$, the intersection point of the ray with the isosurface having isovalue *const* inside the cell is found where $h(\vec{r}) = const$. To find this point, first the ray is re-expressed in terms of (u_0, v_0, w_0) and (u_1, v_1, w_1) using the coordinate systems shown in Figure A.2. In terms of (u_0, v_0, w_0) the ray becomes $\vec{r}_0 = \vec{a}_0 + t\vec{b}_0$, where

$$\vec{a}_0 = (u_0^a, v_0^a, w_0^a) = \left(\frac{x_1 - x_a}{x_1 - x_0}, \frac{y_1 - y_a}{y_1 - y_0}, \frac{z_1 - z_a}{z_1 - z_0} \right), \tag{A.1}$$

and

$$\vec{b}_0 = (u_0^b, v_0^b, w_0^b) = \left(\frac{-x_b}{x_1 - x_0}, \frac{-y_b}{y_1 - y_0}, \frac{-z_b}{z_1 - z_0} \right). \tag{A.2}$$

In terms of (u_1, v_1, w_1) the ray becomes $\vec{r}_1 = \vec{a}_1 + t\vec{b}_1$, where

$$\vec{a}_1 = (u_1^a, v_1^a, w_1^a) = \left(\frac{x_a - x_0}{x_1 - x_0}, \frac{y_a - y_0}{y_1 - y_0}, \frac{z_a - z_0}{z_1 - z_0} \right), \tag{A.3}$$

and

$$\vec{b}_1 = (u_1^b, v_1^b, w_1^b) = \left(\frac{x_b}{x_1 - x_0}, \frac{y_b}{y_1 - y_0}, \frac{z_b}{z_1 - z_0} \right). \tag{A.4}$$

(Note that these equations have had their sign changed from the original equations given in Parker *et al.* [9].) This yields the following function for the value of h along the ray:

$$h(\vec{r}) = \sum_{i,j,k=0,1} (u_i^a + tu_i^b)(v_j^a + tv_j^b)(w_k^a + tw_k^b)h_{ijk}.$$

Setting this equation equal to the isovalue of interest, $h(\vec{r}) = const$, yields a cubic polynomial equation that determines t:

$$At^3 + Bt^2 + Ct + D = 0,$$

where

$$\begin{aligned}
A &= \sum_{i,j,k=0,1} u_i^b v_j^b w_k^b h_{ijk} \\
B &= \sum_{i,j,k=0,1} (u_i^a v_j^b w_k^b + u_i^b v_j^a w_k^b + u_k^b v_j^b w_k^a)h_{ijk} \\
C &= \sum_{i,j,k=0,1} (u_i^b v_j^a w_k^a + u_i^a v_j^b w_k^a + u_k^a v_j^a w_k^b)h_{ijk} \\
D &= -const + \sum_{i,j,k=0,1} u_i^a v_j^a w_k^a h_{ijk} \ .
\end{aligned}$$

Plugging these values into a cubic solver yields t, which can be substituted into the ray equation $\vec{r} = \vec{a} + t\vec{b}$ to find the intersection point $\vec{r}$. The source code for such a cubic solver by Schwarze [42] is available online at numerous *Graphics Gem* archives. However, as explained in Parker *et al.* [9], two modifications to the code must be made. First, the constant EQN_EPS should be changed to 1.0e-30 for maximum stability. Additionally, special cases for when the cubic equation is really a quadratic or linear equation must be added. This happens when the leading coefficients are sufficiently close to zero.

REFERENCES

[1] Caltech computer graphics image gallery, 1999. http://www.gg.caltech.edu/image_gallery.html.

[2] Jacob de Bree. A 3-D anatomy based treatment planning system for interstitial hyperthermia, 2002. http://www.radiotherapie.nl/dissert/debree/summary.html.

[3] Ambar Mukherjee. Data visualization, 2002. http://vizproto.prism.asu.edu/classes/sp02/members/mukherjee_a/viz/.

[4] Some images. http://www.csit.fsu.edu/~erlebach/Website/images/mantle_images.html1.

[5] Tom Goddard. Tracing 1BVP backbone in 8A simulated density map, 2001. http://www.cgl.ucsf.edu/Research/helixhunter/trace/.

[6] Henrik Wann Jensen. *Realistic image synthesis using photon mapping*. A. K. Peters, Ltd., 2001.

[7] Paul S. Heckbert. Radiosity in flatland. *Computer Graphics Forum (EUROGRAPHICS '92 Proceedings)*, 11(3):181–192, 1992.

[8] Diane Lingrand. The marching cubes. http://www.essi.fr/~lingrand/MarchingCubes/algo.html.

[9] Steven Parker, Michael Parker, Yarden Livnat, Peter-Pike Sloan, Charles Hansen, and Peter Shirley. Interactive ray tracing for volume visualization. *IEEE Transactions on Visualization and Computer Graphics*, 5(3):238–250, 1999.

[10] Mike Cammarano and Henrik Wann Jensen. Time dependent photon mapping. In *Proceedings of the 13th Eurographics workshop on Rendering*, pages 135–144. Eurographics Association, 2002.

[11] Richard Wesley Hamming, 2004.

[12] CJ Holmes, R Hoge, L Collins, R Woods, AW Toga, and AC Evans. Enhancement of MR images using registration for signal averaging. *Journal of Computer Assisted Tomography*, 22(2):324–333, 1998 Mar-Apr.

[13] A. James Stewart. Vicinity shading for enhanced perception of volumetric data. In *Proceedings of the 2003 IEEE symposium on Visualization*, page 47. Institute of Electrical and Electronics Engineers, Inc., 2003.

[14] Philip Dutré, Philippe Bekaert, and Kavita Bala. *Advanced Global Illumination*. A. K. Peters, Ltd., 2003.

[15] Bui Tuong Phong. Illumination for computer generated pictures. *Commun. ACM*, 18(6):311–317, 1975.

[16] James F. Blinn. Models of light reflection for computer synthesized pictures. In *Proceedings of the 4th annual conference on Computer graphics and interactive techniques*, pages 192–198. ACM Press, 1977.

[17] C. Madison, W. Thompson, D. Kersten, P. Shirley, and B. Smits. Use of interreflection and shadow for surface contact. *Perception and Psychophysics*, 63:187–194, 2001.

[18] James T. Kajiya. The rendering equation. In *Proceedings of the 13th annual conference on Computer graphics and interactive techniques*, pages 143–150. ACM Press, 1986.

[19] F. E. Nicodemus, J. C. Richmond, J. J. Hsia, I. W. Ginsberg, and T. Limperis. *Geometric Considerations and Nomenclature for Reflectance*. Monograph 161. National Bureau of Standards (US), October 1977.

[20] Peter Shirley. *Realistic ray tracing*. A. K. Peters, Ltd., 2000.

[21] Turner Whitted. An improved illumination model for shaded display. *Commun. ACM*, 23(6):343–349, 1980.

[22] Henry Fuchs, Zvi M. Kedem, and Bruce F. Naylor. On visible surface generation by a priori tree structures. In *Proceedings of the 7th annual conference on Computer graphics and interactive techniques*, pages 124–133. ACM Press, 1980.

[23] Peter Shirley and Keith Morley. *Realistic ray tracing*. A. K. Peters, Ltd., second edition, 2003.

[24] Andrew S. Glassner. Space subdivision for fast ray tracing. *IEEE Computer Graphics and Applications*, 4(10):15–22, 1984.

[25] Henrik Wann Jensen. Global Illumination Using Photon Maps. In *Rendering Techniques '96 (Proceedings of the Seventh Eurographics Workshop on Rendering)*, pages 21–30, New York, NY, 1996. Springer-Verlag/Wien.

[26] Changyaw Wang. Physically correct direct lighting for distribution ray tracing. In David Kirk, editor, *Graphics Gems III*, pages 307–313. Academic Press, Boston, 1994.

[27] The stanford volume data archive, 2001. http://graphics.stanford.edu/data/voldata/.

[28] CT scanning of the head. http://www.radiologyinfo.org/content/ct_of_the_head.htm.

[29] William E. Lorensen and Harvey E. Cline. Marching cubes: A high resolution 3D surface construction algorithm. *Computer Graphics (Proceedings of ACM SIGGRAPH '87)*, 21(3):163–169, 1987.

[30] Jules Bloomenthal. Polygonization of implicit surfaces. *Computer Aided Geometric Design*, 5:341–355, 1988.

[31] Interactive ray tracing, 2005. http://www.cs.utah.edu/classes/cs6620/lecture-2005-03-09-6up.pdf.

[32] Pentium 4. http://www.answers.com/topic/pentium-4.

[33] Kevin Beason, Josh Grant, David C. Banks, Brad Futch, and M. Yousuff Hussaini. Precomputed illumination for isosurfaces. unpublished technical report.

[34] Donald Shepard. A two-dimensional interpolation function for irregularly-spaced data. In *Proceedings of the 1968 23rd ACM national conference*, pages 517–524, New York, NY, USA, 1968. ACM Press.

[35] Wikipedia. Optical fiber - wikipedia, the free encyclopedia, 2005. [Online; accessed 7-July-2005].

[36] David C. Banks. *Interacting With Surfaces in 4-dimensional Space Using Computer Graphics*. PhD thesis, Department of Computer Science (PhD Thesis), UNC-Chapel Hill, 1993.

[37] David C. Banks. Illumination in diverse codimensions. In *SIGGRAPH '94: Proceedings of the 21st annual conference on Computer graphics and interactive techniques*, pages 327–334, New York, NY, USA, 1994. ACM Press.

[38] Steven Richard Hollasch. Four-space visualization of 4d objects. Master's thesis, Arizona State University, 1991.

[39] Andrew J. Hanson, Tamara Munzner, and George Francis. Interactive methods for visualizable geometry. *Computer*, 27(7):73–83, 1994.

[40] Wikipedia. Brane cosmology - wikipedia, the free encyclopedia, 2005. [Online; accessed 7-July-2005].

[41] Tomas Moller and Ben Trumbore. Fast, minimum storage ray-triangle intersection. *Journal of Graphic Tools*, 2(1):21–28, 1997.

[42] Jochen Schwarze. Cubic and quartic roots. In *Graphics gems*, pages 404–407. Academic Press Professional, Inc., San Diego, CA, USA, 1990.

[43] William H. Press, Saul A. Teukolsky, William T. Vetterling, and Brian P. Flannery. *Numerical Recipes in C: The Art of Scientific Computing*. Cambridge University Press, New York, NY, USA, 1992.

[44] Jane Wilhelms and A. van Gelder. Octrees for faster isosurface generation. *ACM Transactions on Graphics*, 11(3):201–227, 1992.

[45] J. Revelles, C. Urena, and M. Lastra. An efficient parametric algorithm for octree traversal.

[46] Gregory J. Ward, Francis M. Rubinstein, and Robert D. Clear. A ray tracing solution for diffuse interreflection. In *Proceedings of the 15th annual conference on Computer graphics and interactive techniques*, pages 85–92. ACM Press, 1988.

[47] Matt Pharr and Greg Humphreys. *Physically Based Rendering : From Theory to Implementation*. Morgan Kaufmann, August 2004.

BIOGRAPHICAL SKETCH

Kevin Beason was born in Tallahassee, Florida in 1977. As a young boy he went on a cross country camping trip. Rather than enjoying the fascinating plains of Texas, he dreamed of the new video game system awaiting his return. Years later, lying on a boat rocking in the sunny Gulf of Mexico off the Florida Keys, he dreamed of simulating the beautiful clouds overhead.

He graduated from Leon High School in 1995, and entered Florida State University, where he acquired a B.S. in Computer Science in 2000, with a focus on mathematics and physics. These studies paid off when he entered the Master's program to study computer graphics and visualization. In graduate school he learned how to simulate light transport, an important step towards making one of his early dreams come true. He plans to find a job continuing his studies in simulating natural phenomena.